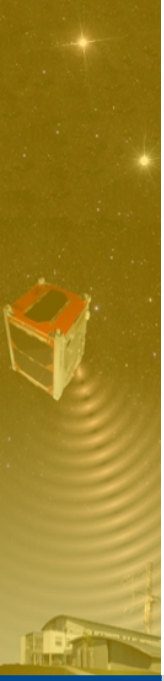

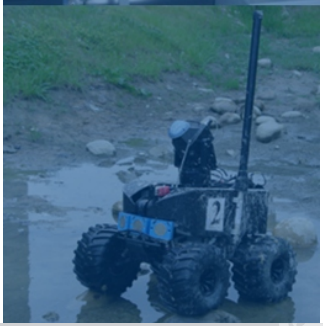

Institut für Informatik
Lehrstuhl für Robotik und Telematik
Prof. Dr. K. Schilling
Prof. Dr. A. Nüchter

Würzburger Forschungsberichte
in Robotik und Telematik

Uni Wuerzburg Research Notes
in Robotics and Telematics

Julius-Maximilians-
UNIVERSITÄT
WÜRZBURG

Band 21

Angelo Pio Rossi, Francesco Maurelli,
Vikram Unnithan, Hendrik Dreger,
Kedus Mathewos, Nayan Pradhan,
Dan-Andrei Corbeanu, Riccardo Pozzobon,
Matteo Massironi, Sabrina Ferrari,
Claudio Pernechele, Lorenzo Paoletti,
Emanuele Simioni, Maurizio Pajola,
Tommaso Santagata, Dorit Borrmann,
Andreas Nüchter, Anton Bredenbeck,
Jasper Zevering, Fabian Arzberger,
Camilo Andrés Reyes Mantilla

DAEDALUS

Descent And Exploration in Deep Autonomy of Lava Underground Structures

DAEDALUS – Descent And Exploration in Deep Autonomy of Lava Underground Structures

Open Space Innovation Platform (OSIP) Lunar Caves-System Study

Angelo Pio Rossi, Francesco Maurelli, Vikram Unnithan,
Hendrik Dreger, Kedus Mathewos, Nayan Pradhan, Dan-Andrei Corbeanu,
Riccardo Pozzobon, Matteo Massironi, Sabrina Ferrari,
Claudio Pernechele, Lorenzo Paoletti, Emanuele Simioni, Maurizio Pajola,
Tommaso Santagata,
Dorit Borrmann, Andreas Nüchter,
Anton Bredenbeck, Jasper Zevering, Fabian Arzberger, Camilo Andrés Reyes Mantilla

February 28, 2021

Study Team

No.	Name	Affiliation	Email Address
1	Prof. Dr. Andreas Nüchter	University of Würzburg, Germany	andreas.nuechter@uni-wuerzburg.de
	Dr. Dorit Borrmann	University of Würzburg, Germany	dorit.borrmann@uni-wuerzburg.de
	Jasper Zevering	University of Würzburg, Germany	jasper.zevering@stud-mail.uni-wuerzburg.de
	Anton Bredenbeck	University of Würzburg, Germany	anton.bredenbeck@stud-mail.uni-wuerzburg.de
	Fabian Arzberger	University of Würzburg, Germany	fabian.arzberger@stud-mail.uni-wuerzburg.de
	Camilo Andrés Reyes Mantilla	University of Würzburg, Germany	camilo.reyes@stud-mail.uni-wuerzburg.de
2	Prof. Dr. Angelo Pio Rossi	Jacobs University Bremen, Germany	an.rossi@jacobs-university.de
	Prof. Dr. Francesco Maurelli	Jacobs University Bremen, Germany	f.maurelli@jacobs-university.de
	Prof. Vikram Unnithan	Jacobs University Bremen, Germany	v.unnithan@jacobs-university.de
	Hendrik Dreger	Jacobs University Bremen, Germany	h.dreger@jacobs-university.de
	Kedus Mathewos	Jacobs University Bremen, Germany	k.mathewos@jacobs-university.de
	Nayan Pradhan	Jacobs University Bremen, Germany	n.pradhan@jacobs-university.de
	Dan-Andrei Corbeanu	Jacobs University Bremen, Germany	d.corbeanu@jacobs-university.de
3	Prof. Dr. Matteo Massironi	University of Padova, Italy	matteo.massironi@unipd.it
	Dr. Riccardo Pozzobon	University of Padova, Italy	riccardo.pozzobon@unipd.it
	Dr. Sabrina Ferrari	University of Padova, Italy	sab.ferrari@gmail.com
4	Dr. Claudio Pernechele	INAF Padova, Italy	claudio.pernechele@inaf.it
	Lorenzo Paoletti	INAF Padova, Italy	lorenzo.paoletti@inaf.it
	Dr. Emanuele Simioni	INAF Padova, Italy	emanuele.simioni@inaf.it
	Dr. Maurizio Pajola	INAF Padova, Italy	maurizio.pajola@inaf.it
5	Tommaso Santagata	VIGEA – Virtual Geographic Agency, Italy	tommy.san84@gmail.com

Abstract

The DAEDALUS mission concept aims at exploring and characterising the entrance and initial part of Lunar lava tubes within a compact, tightly integrated spherical robotic device, with a complementary payload set and autonomous capabilities. The mission concept addresses specifically the identification and characterisation of potential resources for future ESA exploration, the local environment of the subsurface and its geologic and compositional structure.

A sphere is ideally suited to protect sensors and scientific equipment in rough, uneven environments. It will house laser scanners, cameras and ancillary payloads. The sphere will be lowered into the skylight and will explore the entrance shaft, associated caverns and conduits. Lidar (light detection and ranging) systems produce 3D models with high spatial accuracy independent of lighting conditions and visible features. Hence this will be the primary exploration toolset within the sphere.

The additional payload that can be accommodated in the robotic sphere consists of camera systems with panoramic lenses and scanners such as multi-wavelength or single-photon scanners. A moving mass will trigger movements.

The tether for lowering the sphere will be used for data communication and powering the equipment during the descending phase. Furthermore, the connector tether-sphere will host a WIFI access point, such that data of the conduit can be transferred to the surface relay station. During the exploration phase, the robot will be disconnected from the cable, and will use wireless communication. Emergency autonomy software will ensure that in case of loss of communication, the robot will continue the nominal mission.

Contents

SysNova Lunar Caves System Study

Chapter 1

Introduction

Lunar exploration is on the verge of a new golden age starting with the foreseen Gateway station in cislunar orbit serving as an outpost for human exploration and precursor missions such as the foreseen ESA European Large Logistic Lander (also known as EL3), whose development will tie in with the NASA Artemis programme. With this in mind, it is envisioned to have temporary, semi-permanent or permanent outposts on the surface of the Moon and to bring astronauts to these outposts. Such setup implies new challenges in terms of mission concepts for future long-lasting permanence on the Moon requiring new approaches to achieve exploration goals in caverns and lava tubes (Figure 1.1, 1.2).

Two of the main topics to be addressed are identification of in-situ resources such as H_2O, for fuel and oxygen production in situ [88], construction materials for habitats, REE etc. (see [5, 12]) and natural shelters for settlements [22, 133]. Cosmic radiation, extreme temperature excursions between night and day such as 360K to 220K at the Apollo 11 landing site (according to the Apollo 11 technical memorandum, [72]), to extremely low temperatures such as at the lunar south polar regions [29] and not exceeding 100K such in the shaded areas of the Shackelton Crater [74], micrometeorites impacts and sharp, fine-grained regolith represent significant challenges for robotic system design and performance as well as life-support systems.

1.1 The importance of lava tubes exploration

The discovery in 2009 of the Marius Hills skylight with SELENE-Kaguya Terrain Camera [67] opened new questions on the existence [79], formation processes [33, 83, 133], size and stability [22, 133, 149] of underground voids related to drained lava tubes. The existence and entity of such voids has been inferred to be up to hundreds of meters in height by radar sounder measurements at several locations, including Marius Hills [79], gravity mass deficits with GRAIL [36] and comparative planetology with morphometric analysis of Earth analogues [133]. Their stability has been addressed by structural stability models [22, 149] suggesting that, theoretically,

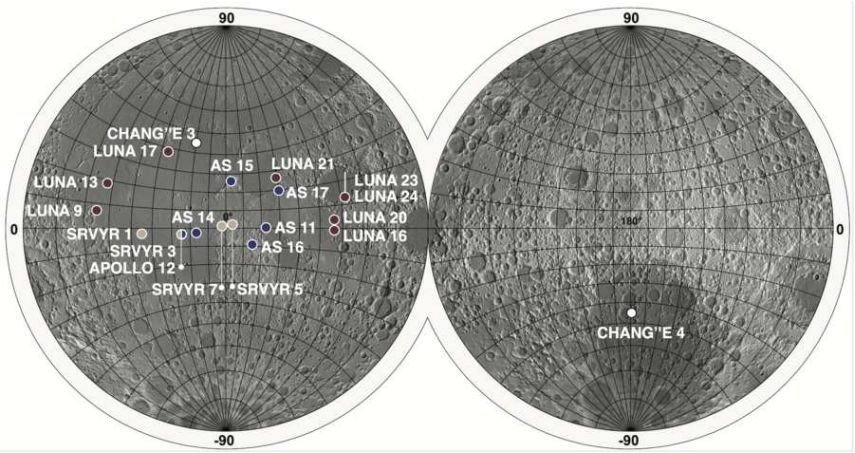

Figure 1.1: Robotic and human-robotic landing sites so far (modified from [128])

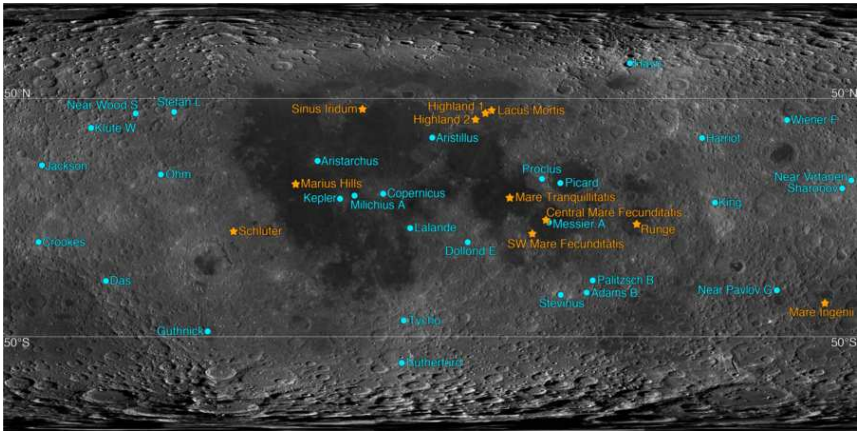

Figure 1.2: Location of pits mentioned in the text, from [153].

under lunar gravity conditions voids up to 1 km across can be stable under only few meters-thick roofs. Such roof geometry has been imaged at different phase and incidence angles by NASA LROC NAC showing that these lava-tube roofs are often overhanging and formed by several

meter-thick layers of lava flows [125]. Therefore the accessibility of these lava-carved caves could potentially provide, as in Earth analogues, stable temperatures with little to no variation across day and night cycles, micrometeorites impacts and shelter from radiation. The only known access to these voids are vertical shafts with overhanging roof (Wagner and Robinson 2014), whose thickness is variable and the estimate of the environmental characteristics of these voids as well as their stability remains largely theoretical or inferred from comparative planetology (e.g. [44]) , including aspects to their hazards to humans (e.g. [8]).

The ability to access such voids (Figure 3) could both provide answers to all the above questions related to environmental conditions as well as give the possibility for science of opportunity also during the descent of the vertical shaft (e.g. [68]). In fact, along the walls, the possibility to analyse at close-range the stratigraphy of the stacked lava flows (which is present and well-visible as in [125]) constituting the roof of the conduit, will provide more insights both in terms of morphological characteristics of the lava layers, presence of paleoregolith, fracturing and compositional diversity. Overall, the knowledge of the uppermost crust of the Moon and its thermal evolution, the styles of its volcanism and the volatile migration history will be advanced through observations of lava layers, in particular through their:

- Composition
- Derived flow rheology
- Overall morphology of the tunnel
- Possible presence of volatiles and cold traps

1.2 Exploration challenges

The exploration of the surface of the Moon, both with crewed and uncrewed missions, has been essentially concentrated in the Apollo era. Later on, the CNSA with the Chang'e 3 mission in 2013 [156] and the Chang'e 4 in 2019 [155] were the newest attempts to navigate on the surface of the Moon since decades.

Several environmental, geomorphological and trafficability challenges and hazards have to be taken into account and mitigated when planning a mission on the surface, adding new levels of complexity in the attempt to deploy a device in the subsurface. These challenges are even more increased in semi-autonomous navigation and mapping in a previously unexplored area, with limited communication increases the level of complexity and hazard as well.

Overall, the first challenge is of course environmental. Radiation and temperatures need to be cped with proper materials and dissipation/heating of the internal robotic devices and analytic instruments. We have a well-known record on how the radiation and temperature profiles to expect on the Moon since the early '70s thanks to the Apollo missions at low-mid

latitudes [72] and further refined and expanded towards the poles (e.g. [29]) and the knowledge of the amount of radiation was refined as well [8]. We could expect that the subsurface will retain lower radiation levels as it is shielded by meters of hard rock.

The second challenge is selecting the landing area. It should be essentially obstacle-free, sufficiently flat and with a ground material able to support the lander/rover devoted to pit approach and Daedalus deployment.

Therefore, the selection of the landing site is tied with terrain characterization and trafficability towards the experiment site. In our case, boulders and small craters can be an obstacle to approach and maneuver towards the pit. This problem has been under characterization and assessment since the late '90s on the Mars surface [57] in order to assess safety for the lander and rovers trafficability/operations [58]. Such hazard analysis was further refined with both manual [115] and automatic detection [58]. Since 2006, these operations were performed on Mars by means of the high-resolution capabilities of HiRISE camera [100] with a ground resolution of 0.25 m/pixel. On the moon the same detections can be performed on the LROC NAC images with a ground resolution of 0.5 m/pixel [127].

Overall, all these challenges and relative hazards will be analyzed and characterized in detail. Indeed, the techniques are well-established by the scientific/engineering community thanks to case-studies associated with past, present and future Mars landing sites (see e.g. [60, 116] and references therein). However, for the lunar case the major challenge never attempted before is the deployment of a device within an almost totally confined environment (i.e. the vertical pit and the underground tunnel) which will require ad hoc communication and data transfer to the surface, as well as ad-hoc analytical solutions to carry out analyses in a completely dark environment, and essentially made up of dark basaltic rocks.

The eventual trafficability of the tunnel and the untethered communication with the Daedalus sphere will also provide a major challenge in the entire mission scenario. Semi or complete autonomous navigation is required, and, as happens in terrestrial analogues (see [82, 134] and references therein) the type of environment to expect is essentially regolith with piles of boulders of various sizes (from centimeters to tens of meters) due to the roof collapse. Therefore, navigation must be expected to be extremely challenging or impossible.

Finally, if navigation turns out to be possible due to a relatively obstacle free underground environment, the sharpness of the rocks and the lunar regolith must be seriously taken into account. Indeed, it is well-known since the Apollo missions that regolith can be extremely sharp and abrasive, and being also of very fine granulometry (50% by volume $<$50 micron), hence it can interfere with and degrade mechanical joints. The adhesive properties of regolith must also be taken into account and mitigated.

Chapter 2

Executive Summary

2.1 Study Flow

The DAEDALUS study was an ESA Open Space Innovation Platform (OSIP) lunar caves-system study, requested by ESTEC. The study was carried out by an interdisciplinary team of specialists from University of Würzburg, Jacobs University Bremen, University of Padova, INAF Padova, and VIGEA, starting with a Kick-Off on April 7, 2020 and finishing with an final Presentation on December 17, 2020. Intermediate progress meetings were held on September 17, 2020 and November 9, 2020.

2.2 Study Objectives

The Daedalus mission concept addresses specifically the following ESA Moon exploration objectives:

- Identification and characterisation of potential resources for future exploration.
- Characterisation of the dynamic dust, charge and plasma environment.
- Characterisation of biological sensitivity to the lunar environment.

Those objectives will be addressed with geologic and compositional vertical surveying and three-dimensional assessment in the landing / caving site, continuous monitoring throughout the descent of temperature, radiation and dust environment, as well as with the overall environmental and lithological characterisation of the shaft and explored cave portions.

Moreover, DAEDALUS indirectly contributes to the following objectives:

- Deployment of geophysical instruments and the build up a global geophysical network.
- Analysis of new and diverse samples from the Moon.

These indirectly addressed objectives will be tackled with the one-station role of DAEDALUS at the bottom of the selected shaft, whose measurements will be correlated with eventual additional lander or rover locations active at the time of the mission. Moreover, the access to pristine samples protected from the surface radiation environment (space weathering) and micrometeorite impacts could provide, for follow up robotic and human exploration missions, access to samples for additional deeper in-situ and sample return analyses.

2.3 Requirements and Design Drivers

Lunar exploration is on the verge of a new golden age starting with the foreseen Gateway station in cislunar orbit serving as an outpost for human exploration and precursor missions such as HERACLES [97]. With this in mind, it is envisioned to have temporary, semi-permanent or permanent outposts on the surface of the Moon and to bring astronauts to these outposts, such as in the future Artemis programme. Such setup implies new challenges in terms of mission concepts for future long-lasting permanence on the Moon requiring new approaches to achieve exploration goals in caverns and lava tubes.

Two of the main topics to be addressed are the identification of in-situ resources (H_2O, for fuel and oxygen production in situ, construction materials for habitats, Rare Earth Elements etc.) and natural shelters for settlements. Cosmic radiation, extreme temperature excursions between night and day such as 360 K to 220 K at the Apollo 11 landing site (according to the Apollo 11 technical memorandum [76]), to extremely low temperatures not exceeding 100K in the Shackleton Crater [73], micrometeorites impacts and sharp, fine-grained regolith represent significant challenges for robotic system design and performance as well as life-support systems.

The discovery in 2009 of the Marius Hills skylight with SELENE-Kaguya cameras opened new questions on the existence, formation processes, size and stability of underground voids related to drained lava tubes [65]. The existence and entity of such voids has been inferred to be up to hundreds of meters in height by radar sounder measurements at several locations, including Marius Hills [80]) as well as gravity mass deficits with GRAIL [37]. Their stability has been addressed by structural stability models [23] suggesting that, theoretically, under lunar gravity conditions voids up to 1 km across can be stable under only few meters-thick roofs. Such roof geometry has been imaged at different phase and incidence angles by NASA LROC NAC showing that these lava-tube roofs are often overhanging and formed by several meter-thick layers of lava flows [126]. Therefore, the accessibility of these lava-carved caves could potentially provide, as in Earth analogues, stable temperatures with little to no variation across day and night cycles, micrometeorites impacts and shelter from radiation. The only known access to these voids are vertical shafts with overhanging roof, whose thickness is variable and the estimate of the environmental characteristics of these voids as well as their stability remains largely theoretical or inferred from comparative planetology (e.g., [45]), including aspects to

their hazards to humans (e.g., [7]).

The ability to access such voids could both provide answers to all the above questions related to environmental conditions as well as give the possibility for science of opportunity also during the descent of the vertical shaft (e.g., [66]). In fact, along the walls, the possibility to analyse at close-range the stratigraphy of the stacked lava flows (which is present and well-visible as in [126]) constituting the roof of the conduit, will provide more insights both in terms of morphological characteristics of the lava layers, presence of paleoregolith, fracturing and compositional diversity. Overall, the knowledge of the uppermost crust of the Moon and its thermal evolution, the styles of its volcanism and the volatile migration history will be advanced through observations of lava layers, in particular through their composition, derived flow rheology, overall tunnel morphology and possible presence of volatiles or cold traps.

Requirements		
Req. ID	Category	Requirement formulation
Req-M01	Mission	The Mission shall be designed for a launch in 2030
Req-S01	Science	The Sphere shall map lunar caves and shafts with a LIDAR scanner and 95 % coverage.
Req-S02	Science	The Sphere shall record the cave with optical sensors to 95 % in stereo coverage.
Req-T01	Technical	The sphere shall gather the data on the ground of the cave.
Req-T02	Technical	The sphere shall gather the data while desending the shaft to the cave.
Req-T03	Technical	The sphere uses new hemispherical lenses with a field of view of 270 degree.
Req-T04	Technical	The robot needs to have a working temperature range of 100K to 360K.
Req-T05	Technical	The robot shall be designed as a sphere with only minimum deviations.
Req-T06	Technical	While descending the sphere shall cover the wall of the shaft with 4cm per optical pixel.

2.4 Study Approach

The study is structured as follows: First, we analyze the sphere for descending lunar craters. This includes an analysis of the locomotion principle, where we review also alternative approaches, such as using the concept of impulse by conservation of angular momentum (IBCOAM). These considerations lead finally to the proposed locomtion system. As the LiDAR subsystem plays an important role in our concept, we take an in-depth look at it, when discussing the sphere for descending lunar craters. The same applies to the camera subsystem. Second, we take a look at the geology and the spectral requirements. This includes the landing site analysis and spectral requirements. Third, we discuss optical imagary and how it can be used to compute 3D models for this exploration task.

Based on all discussed points, we come up with the final design proposal for the DAEDALUS sphere. The overall study flow is presented in Figure 2.1.

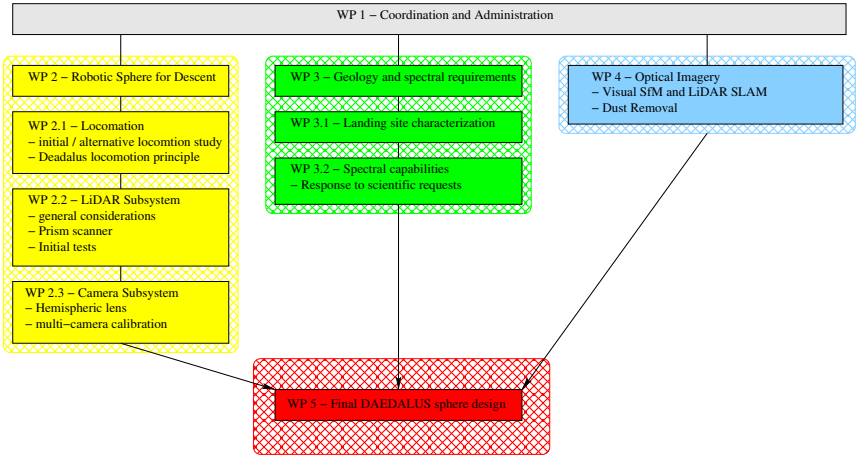

Figure 2.1: Study flow as PERT-like diagram.

2.5 Landing Site Characterization

2.5.1 Introduction

The trafficability of maria-like terrains has been widely explored during Apollo human explorations with crewed vehicles. In this case the exploration of the Marius Hills lava tube is tied to the possibility to land, rove and approach safely to the skylight. Without that, no exploration mission would be possible, and therefore it is mandatory to characterize in high detail the terrains surrounding the skylight both in terms of hazard and safety. Ideally, the pit should be surrounded by obstacle-free terrains and presenting a relatively low boulder presence, while the regolith would be able to sustain inertial platforms with a relevant weight (up to the 300 kg foreseen for the HERACLES deprecated robotic sample return mission as detailed in [97]). In addition, the location should guarantee an easy approach to the pit up to a location where the Daedalus sphere will be deployed. Therefore in order to characterize the feasibility of landing, approach and deployment of the Daedalus sphere several aspects of the terrains surrounding the pit must be investigated taking into account several morphometric parameters:

- flat surface over steep overhanging pit margins, with a slope safety margin of 15 deg
- hazard-free or low-hazard trafficability from landing ellipse to the pit
- hazard free landing area (low crater density, low slopes, boulder-free)
- closest point to the shaft

2.5.2 Geologic context

Marius Hills region is among the largest volcanic complexes on the Moon and is located in the Oceanus Procellarum. Aside from the presence of multiple monogenic cones set on a ∼300 km shield, it is also characterized by widespread mare basalt and very large rilles at its flanks, namely rille A and B [18, 141].

The selected skylight is a nearly circular hole of ∼65 m in diameter, located at 303.3°E, 14.2°N in the Marius Hills region, roughly in the middle section of the so-called "rille A" in correspondence of a ∼90 deg change of direction (Figure 4). The first detection was achieved via SELENE-Kaguya Terrain Camera images by [65], whose fist depth estimate was of 80m. Later, [126] performed photoclinometric measurements on the shadow on the pit floor with slanted observation (Figure 5) at 5 m/pixel resolution with LROC NAC images, reduced the height estimation at 40m.

2.5.3 Datasets and software tools used

The datasets used are listed in table 2.2

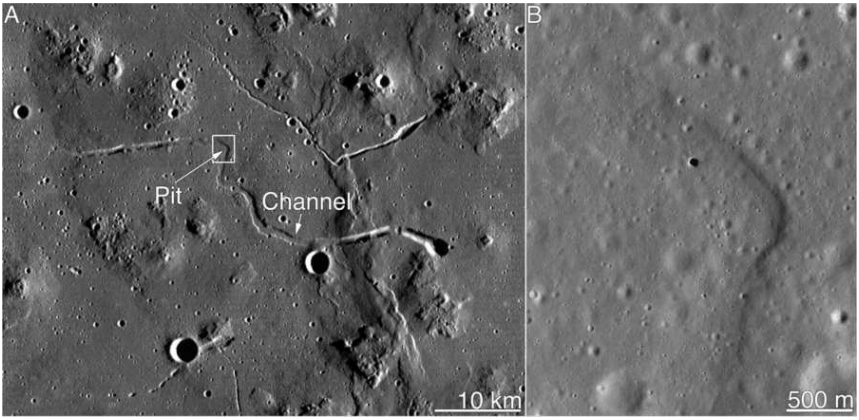

Figure 2.2: In A) location of the Marius hills rille "A" and in B) location of the pit, from [153]

LOLA (Lunar Orbiter Laser Altimeter) data merged with the SELENE-Kaguya stereo DEM result in a global DEM of ∼59 m horizontal resolution and 4m of vertical resolution. The LROC NAC stereo DEM produced by the instrument team was used as an absolute reference for the heights of our custom made DEM for the landing area.

To achieve this product we used ISIS (Integrated Software for Imagers and Spectrometers) by USGS to process the LROC NAC raw files and the ASP (Ames Stereo Pipeline) software to generate the stereo DEM and align it with the absolute reference.

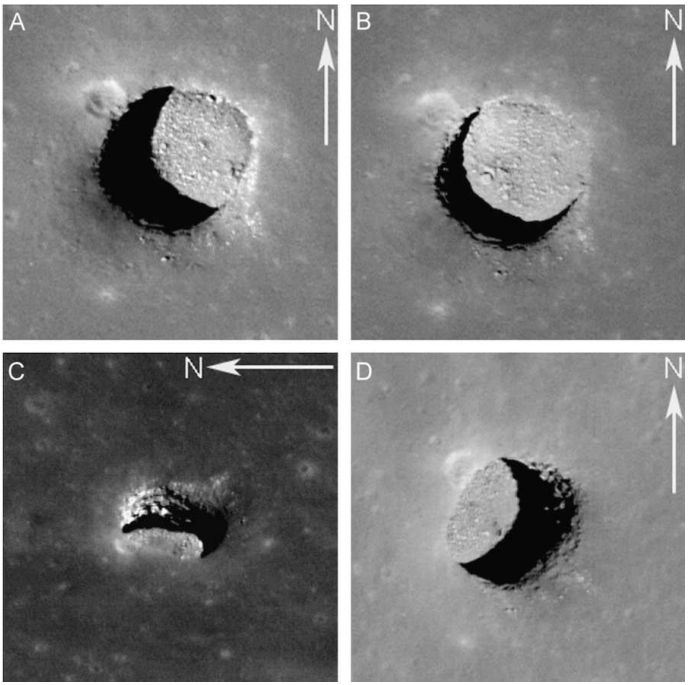

Figure 2.3: Slanted observations with LROC NAC camera of the marius hills pit. In C the different lava layers along the pit walls are visible [126].

Table 2.2: Used datasets for the landing site characterization

Dataset	Product ID	Source of raw / derived data	Resolution
LOLA+Kaguya merged DEM	Lunar_LRO_LOLAKaguya_DEMmerge_60N60S_512ppd.lbl	USGS Astrogeology	59 m grid spacingx
LROC NAC images	M1219322049LE M1219329084LE	PDS Geosciences Node	0.95 m/pixel
LROC NAC DEM	from the LROC NAC image stereo pair above	Daedalus custom data product	5 m/pixel

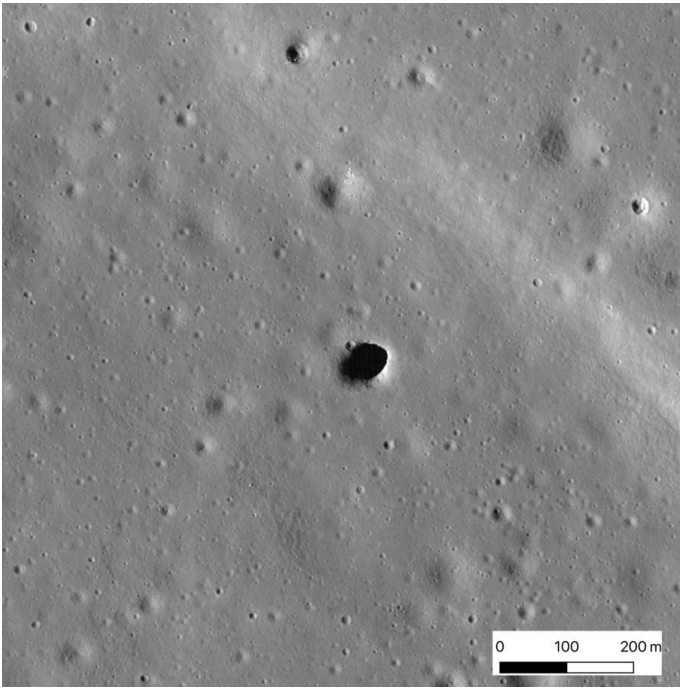

Figure 2.4: LROC NAC Orthoimage of the Marius Hill pit entrance (1 m/pixel resolution).

2.5.4 Data processing and analysis

Raw LROC NAC stereo images from the PDS geosciences node were processed in order to perform radiometric calibration to remove vignetting and possible sensor-related artifacts. The pointing and navigation kernels of the satellite were then attached to the image header in order to obtain a precise location on the surface of the Moon. Furthermore, the two images were bundle-adjusted in order to refine the pointing of the two images and obtain a product validated for scientific measurements. Processing steps used both USGS ISIS3 [6] and NASA ASP [19] respectively higher level data processing and stereogrammetry systems.

Such images were then cropped in order to obtain a buffer area around the skylight of 1×1 km. This has a double advantage: speed up the processing time for stereo DEM generation and avoid possible problems generated by areas outside our region of interest.

The stereo matching algorithm takes care of identifying tie points in both of the images and reconstructs a 3D point cloud by means of an iterative closest point algorithm, and finally was further aligned to the LROC NAC DEM used as absolute reference. At this point the point cloud is interpolated in a grid whose horizontal resolution is typically three times larger than the original stereo imagery resolution, in order to avoid noise and artifacts. However, we interpolated our point cloud at 1 m resolution in order to be able to further refine the DEM with shape from shading technique.

This technique is frequently used to enhance the fine details of the DEMs where the stereo matching algorithm is not able to do that with the use of tie points. It is based on using the illumination conditions of one (or multiple) images of the same area in order to derive the convexities and concavities of the surface defined by the shading in the images themselves. Shape from shading is typically highly computationally expensive and does not always provide a best solution, but is largely dependent on illumination conditions, and in particular to the presence of hard shadows or oversaturated image portions.

We decided to use it in order to cope with the poor performances of the stereo matching algorithm in the particular setting of the Marius Hills region. In fact, the best results in stereo reconstruction are obtained when the illumination conditions of the original stereo images are quite similar one to each other, when there is no occlusion of terrain portions by steep slopes or overall terrain morphology that needs to be variegated and not completely flat and completely shaded areas need to be avoided as they bear no information. However, the Marius Hills skylight surroundings display all of these far from ideal features: a flat terrain with no or little stereo information usable for reconstruction, a very steep and completely shaded region (the pit itself). This hard shadow is furthermore not ideal even for shape from shading as it can severely affect the result in the whole region. With this respect, the ASP stereo_gui function was used to calculate the shadow-threshold value, in order to be avoided by the shape from shading algorithm while performing DEM refinement.

In order to parallelize the computation we used the gnu-parallel utility, divided the image into 200×200 pixel tiles (with 1 pixel=1 meter in this case) and 50 pixels of overlap between adjacent tiles to avoid stitching artifacts. We assigned a low smoothing value in order to preserve as much information as possible and we limited the shape from shading iterations at 3. More iterations will result in artifacts as streaks in the illumination direction and deteriorate the final DEM quality. We chose a lunar Lambertian reflectance type material [19] to be used and used the bundle adjustment information of the 2 images used also to perform shape from shading. We thus obtained a perfectly comparable DEM with all the heights matching with the previous validated one but with much higher detail, mandatory to quantify slopes, depths and terrain hazards in detail (Figure 8).

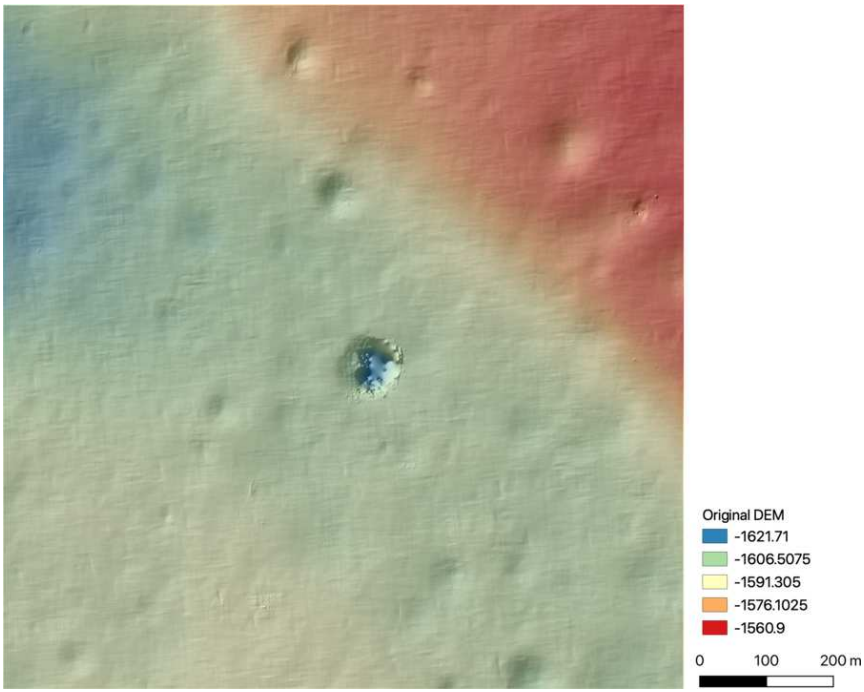

Figure 2.5: Original DEM obtained from stereogrammetry, using LRO LROC NAC data. DEM ground resolution is 3 m/pixel

2.5.5 Hazard characterization

The stereo DEM refined was analyzed with several algorithms for morphometric characterization. In general terms, we were able to perform an automated quantitative crater detection using the refined DEM and the multi-scale TPI (Topographic Position Index) in SAGA GIS (See Pozzobon et al, 2018, and ref. therein). TPI is a dimensionless index based on the difference of elevation between a DEM pixel cell and the average elevation of its neighborhood. By selecting a proper neighborhood we could derive all the depressed areas with respect to the surrounding plateau. Since TPI output is depending on the scale of the neighborhood it is possible to use a multi-scale TPI tha analyzes neighborhoods at different scale-size at the same time. We set these thresholds to be 4, 10 and 100 meters in order toso that we could detect small craters (less than 4 meters, the minimum viable threshold to define a circular object), medium craters and the larger ones

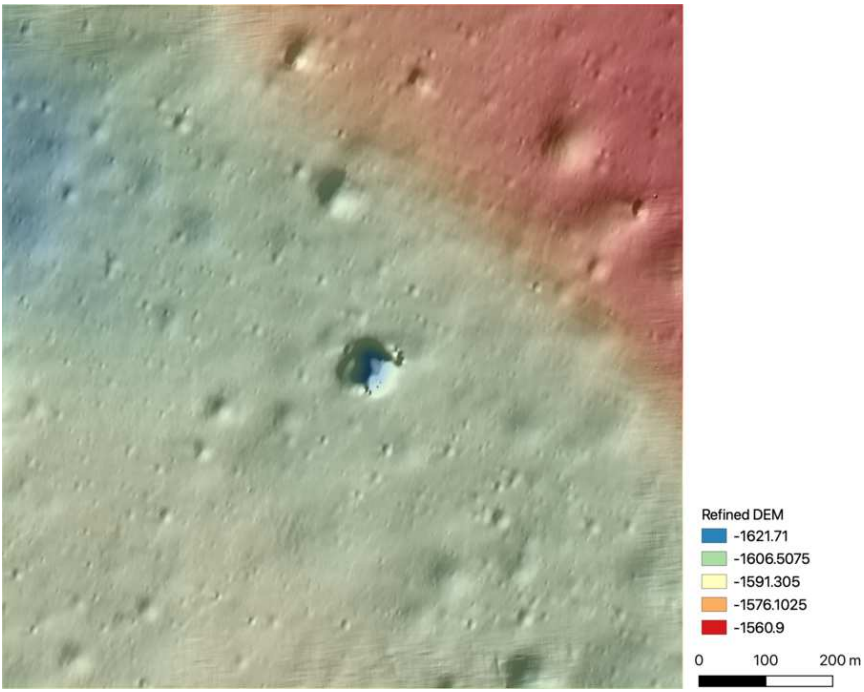

Figure 2.6: Refined DEM with SfS applied. Note the limited striation/artifact, vs. a large increase in detail, with craters of just a few meters appearing and with measurable depths.

(as also the pit, ofis 80×90 meters of size, it is also classified as a depression).

We were therefore able to characterize the following hazards:

- Crater density: Crater density is a first order of trafficability hazard [114]. Of all craters we identified, some of them are not hazardous as they may be very shallow (few decimeters per meter in diameter, slopes being negligible);
- Slopes: slopes thresholds were extracted following the Burrough and McDonnell technique, and they represent the major trafficability constraint on the area [28]. Based on both HERACLES [97] and MSL Curiosity/Perseverance constraints [60] we selected a maximum slope safety threshold to be < 15 deg. We also characterized the terrain in order to have a safer slope threshold set at < 10 deg which should be acceptable by any rover-lander;

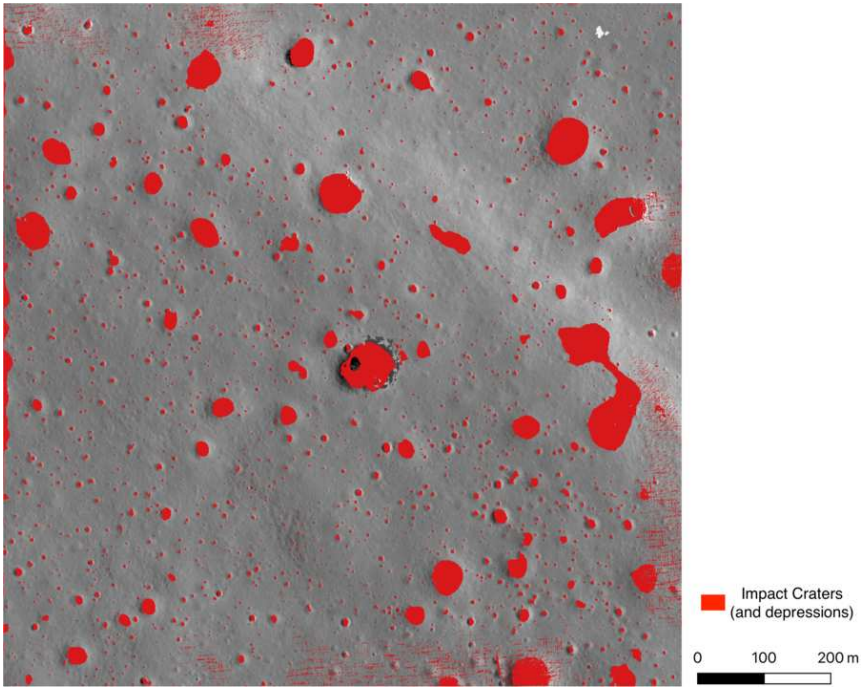

Figure 2.7: LROC NAC orthorectified image at 1 m/pixel resolution. Red areas mark the impact craters and depressions extracted from the high-resolution SfS-refined topography.

- Craters' depths: Crater depths' have been characterised through the derived DTM. All craters shallower than 1 m and with inner slopes <15 deg have been considered safe;
- Boulder abundance: it was detected by means of the LROC NAC orthorectified 0.5 m/pixel image, as boulders are usually smoothed by the interpolation algorithm while creating the DEM. Less than 50 boulders are present in the area and none of those are affecting the overall hazard of the analyzed region

2.5.6 NO-GO areas definition and proposed landing ellipse

The no-go areas have been finally defined by merging together all the hazard information detected, and marked in red in fig. 12. We also provided a map of the areas where trafficability is

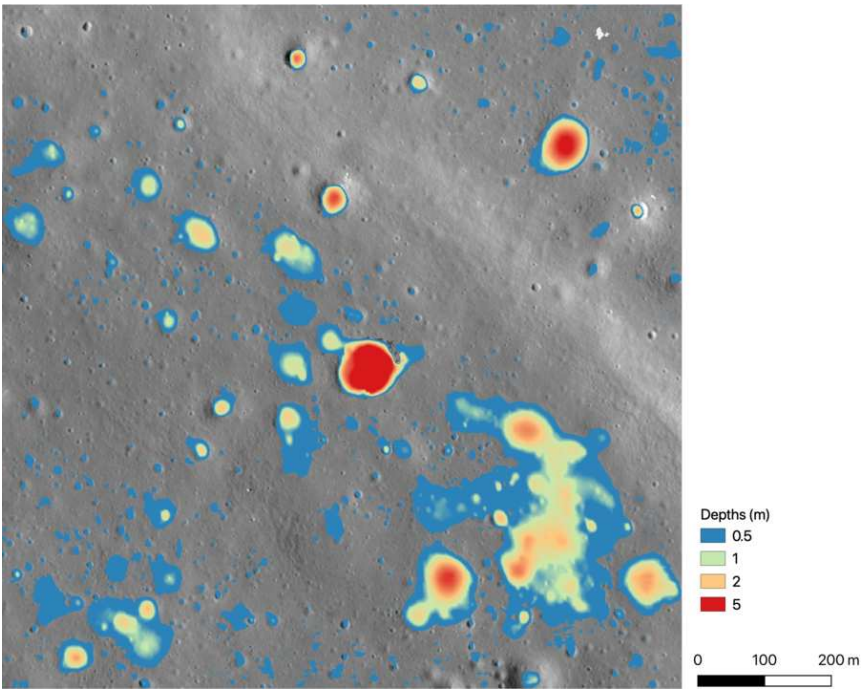

Figure 2.8: Impact craters' and depressions' depths, as inputs for the hazard assessment.

possible but with more caution, as potential hazards can be present but not clearly detectable with the available data resolution. A tentative landing ellipse of 300×200 meters was placed in the safest area of the 1×1 km buffer around the pit, where minor landing and trafficability hazards are present and the travel distance towards the pit is less than 1 km.

2.5.7 Skylight and cave entrance characterization

In order to identify the sizes of the boulders located on the floor of the sinkhole (remnants of the collapsed ceiling) we made use of an LRO/LROC-NAC image (M155607349RE) with a spatial scale of 0.42 m and with a solar incidence angle of ∼12 deg. Through the ArcGIS software we assumed the boulders to be circular in shape (the resolution of the image did not allow to characterise such features as polygons) and then extracted their maximum dimension. This is a common technique that was already applied several times to the Moon (e.g. Bart and

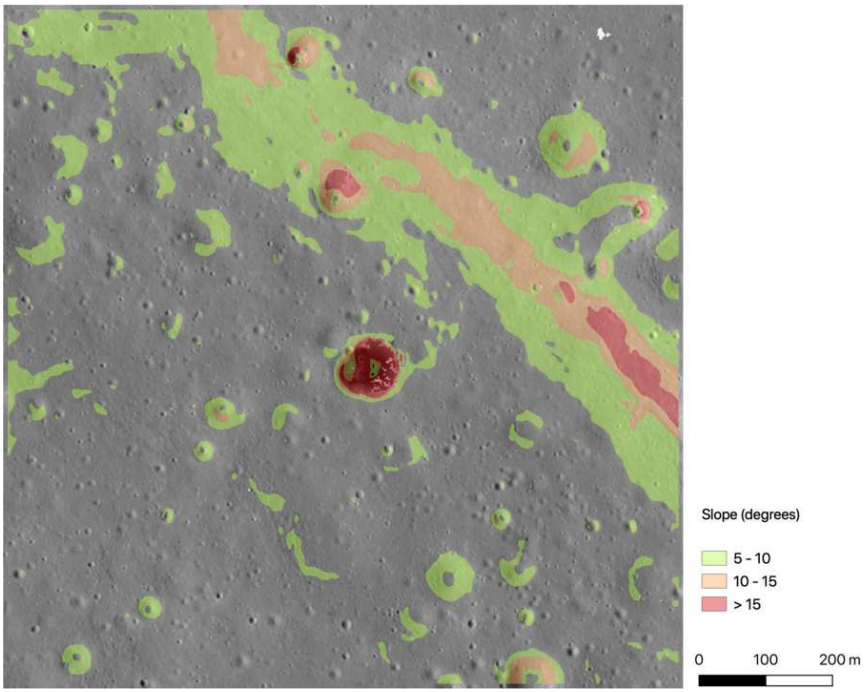

Figure 2.9: Slope classification of topography, overlaid on LROC NAC orthoimagery, used as input for hazard assessment.

Melosh, 2010; Pajola et al., 2019) and to other bodies, such as planets [115], comets [117] or asteroids [47]. Afterwards, in a log-log plot, we fitted the data by using a linear regression as shown in Figure 2.12, hence obtaining the power-law index of the distribution. The error bar for each value is the root of the unbinned cumulative number of counted boulders [104]. We used the common three pixels sampling rule to estimate the minimum size of the statistically meaningful dataset [111], hence all counts with dimensions smaller than $\sim$1.2 m are not considered by the fit. The resulting power-law index is -2.6 $+0.3/-0.4$. Such slope can be used to assess the possible cumulative number of boulders/pebbles towards the smallest sizes and is pivotal for engineering safety evaluation. The maps in Figure 2.11 show how the boulders are distributed and which is their abundance in the bottom of the pit. A relatively boulder free area with high frequency of small-sized ones is located in the north-western part, making it a promising target

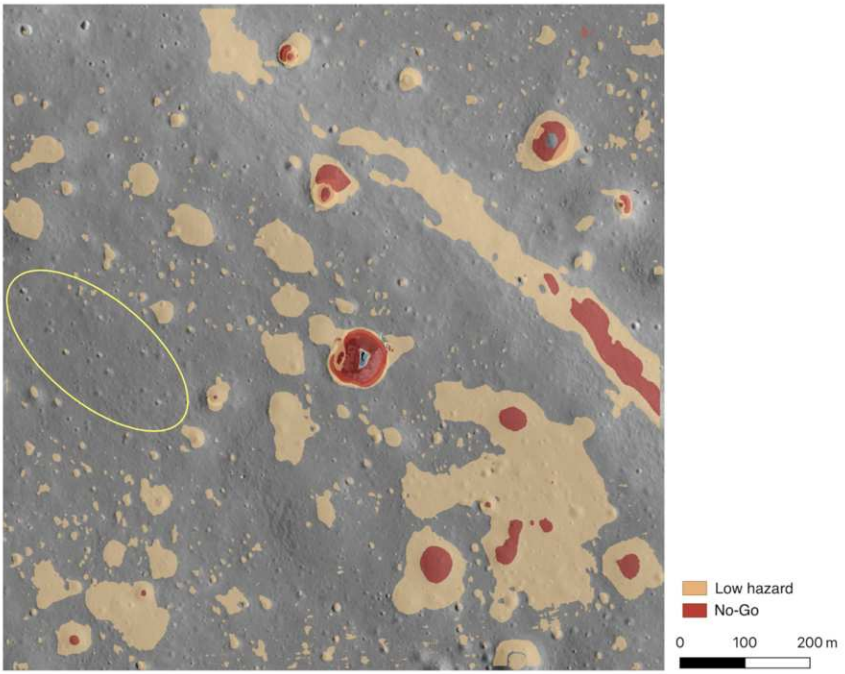

Figure 2.10: Hazard detection quantitative map resulting from the integration of Figure 9-11). The "no-go" areas are marked in red whereas the orange areas present low (but still present) hazard corresponding to the maximum tolerance of slopes/roughness/relative depths of the terrain. All remaining regions are virtually safe.

for DAEDALUS deployment.

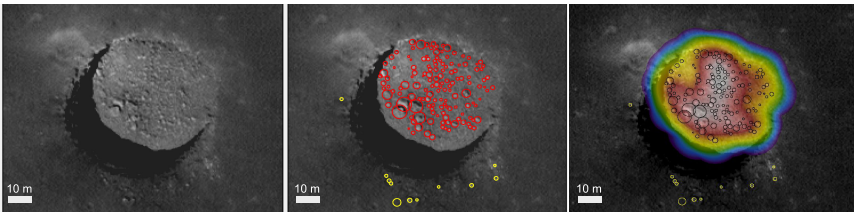

Figure 2.11: Boulder mapping in the pit. In the left panel close up of the LROC NAC M155607349RE image with ∼12 deg of solar incidence angle. In this case the bottom of the pit is well-lit and trafficability evaluations can be quantitatively assessed. In the central panel are visible in red boulders mapped on the bottom of the Marius Hills Skylight. In yellow boulders mapped on the surface close to the edge of the pit. In the right panel is displayed the boulders map (black circles) and colour-coded map of boulder abundance weighted on their size. The red-white bears the largest number of boulders with the largest diameters, the yellow-green portions present boulders of sub-metric size with high trafficability potential. Indeed, the north-western portion of the pit is a promising target for DAEDALUS deployment.

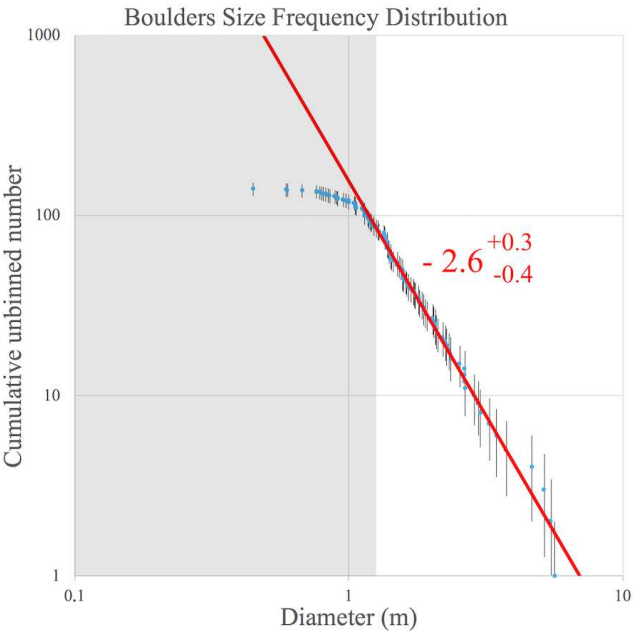

Figure 2.12: The boulders size frequency distribution evaluated on the Marius hills pits' floor. The grey area covers the sizes that are not considered by the fitting curve (<1.2 m)

Chapter 3

Robotic Sphere for Descent

The advantage of using spherical robots is the practicality it represents in the face of different types of terrain and environments in which they can perform a variety of tasks, all sensors, internal control unit (ICU) and framework setup are shielded from the outside by the shell, meaning that they are unaffected by harsh environments such as sand, mud, water, and even snow. Likewise, the spherical shape allows them to perform actions that cannot be achieved with other types of robotic configurations: they can be more task-adjustable than any other conventional robot, depending on the objectives they can even semi-deform their shape so that they can achieve more complex tasks, they can also be networked and allow signal transfer in places where communications from surface to subsurface are not possible due to electromagnetic absorption by rock and/or debris [51], they can also be useful tools in the monitoring and tend of crops all over the world [34]; everything lies in the type of tasks to be carried out and in the work environment, and even in the imagination of its creators. As Ocampo-Jimenez et al. [112] state in their work on spherical robots based on the sea-urchin characteristics, a source of inspiration is nature itself, where locomotion and reconfiguration mechanisms can be used as metaphors to inspire or improve the design of mobile robots and autonomous vehicles, to be used and implemented in the most diverse ways. Thus, they are ideally suited for the exploration of unknown harsh environments such as lunar lava tubes. Apart from the crucial design also the materials are highly important, since the durability of the robot and the extent of the tasks it performs depends on this. In this chapter the general design for the Daedalus sphere is analysed, including experiments regarding the locomotion mechanism and the sensor setup. Additionally, algorithms for state estimation as well as autonomous navigation are discussed.

3.1 Locomotion

The spherical design allows to create a holonomic system, which is a system where the controllable degrees of freedom are equal to the total degrees of freedom, making them omnidirectional

irrespective of their desired direction of movement, enhancing the mobility on spherical-shaped robots. This section decribes different locomotion concepts that have been studied for the design of the Daedalus sphere.

3.1.1 Differential Drive – Comparable Study

A differential drive system for locomotion is the first comparative platform which was developed and studied, due to vast use of these motors and configuration for various robotics systems. For the sake of stability and payload space, the original spherical design was extended into a cylindrical shape. This guarantees an easier maneuverability and more space for the scientific equipment.

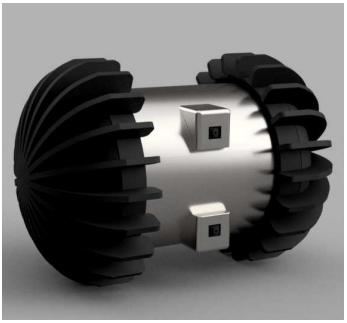

Figure 3.1: Design of the differential driven robot with spherically shaped wheels.

The robot is divided into three parts: the two semi-hemispheres that act as wheels and an internal corpus which houses the scientific equipment and is connected to the semi-hemispheres with two motors. The robot moves by controlling each of the semi-hemispheres individually, which enables it to turn into any direction with a zero-turn radius.

The body is further divided into three sections, each section dedicated for a different purpose as shown in Figure 3.2. The top section is intended to house equipment for visual odometry. The middle layer contains the control and communication module, as well as the two electrically driven motors to propel the wheels. Lastly, the bottom section is selected for the battery system.

Laboratory Setup

The contact area of the ground of this design's wheels is relatively small. Since traction is very important to consider when designing a lunar robot an alternative design has been developed that has a contact surface which is twice as large (bottom images of Figure 3.3). The larger area

Figure 3.2: The top left image demonstrates the bottom segment of the robot. The top right image shows the top segment of the robot and the bottom image shows the middle segment of the robot.

is assumed to have a better grip into the soil, noting however that this type of wheel design is exposed to a larger amount of rolling drag than the spherical shaped wheels.

In order to simulate the difference in gravity on the moon compared to earth, a mechanism was built to resemble the lunar gravity. The robot is connected to a rope that goes through a pulley and has a counterweight on the other side to decrease the weight of the robot to $\frac{1}{6}$. Figure 3.4 shows an image of the constructed site. The robot drives along a straight line underneath the pulley system. For the counter weight, a bucket with sand is used to approximate the weight of the robot under lunar gravity.

Results and Shortcomings

A fundamental problem arises with this design. Since the internal body has no point of contact to the ground, the torque produced by the motors can cause a rotation of the body itself instead of the wheels. This case can occur when the weight of the body is too light compared to the wheels. To ensure that the motor torque results in a rotation of the wheels instead of the body, the center of mass has to be as far away as possible from the wheel axis. To distribute the weight accordingly, the heaviest component, the battery system, is mounted in the bottom of

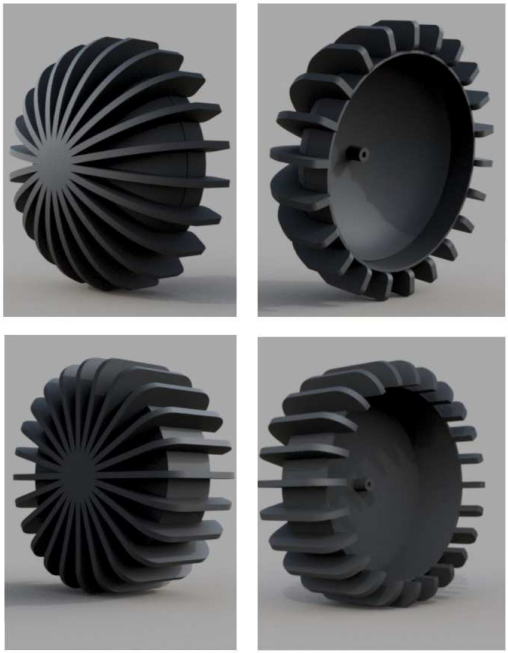

Figure 3.3: The top images show the spherically shaped wheels. The bottom images show the alternative design with a rectangular shape.

the robot. The robot might still be susceptible to tilting during the acceleration phase which needs to be considered when evaluating the data of the visual sensors.

A mechanical solution for this problem is to attach a rod perpendicular to the horizontal axis and the center of mass at the bottom of the robot to prohibit the internal body from rotating. However, this reduces the mobility of the robot greatly as it continuously creates drag and reduces the turn radius of the robot. It is also a new potential failure point considering the harsh environment the robot is to be deployed in. The connection to the wheels can also represent another weakness in high dust environments while the self contained spherical robots do not share this weakness.

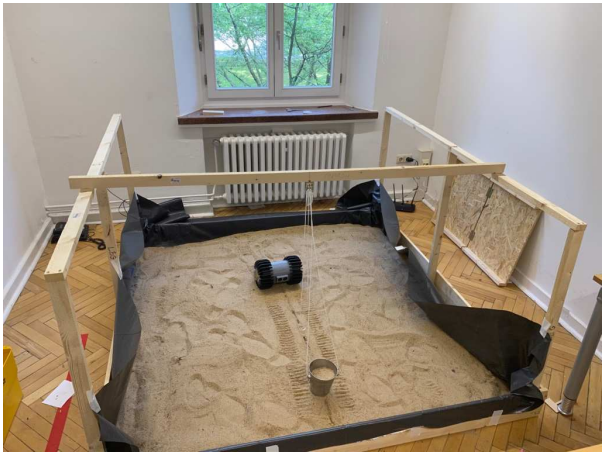

Figure 3.4: Testing site for the rectangular wheels

3.1.2 Impulse by Conservation of Angular Momentum Drive

Concept

We investigated another approach to move the spherical robot using the impulse generated by the conservation of angular momentum (IBCOAM). The basic idea behind the IBCOAM drive is that a torque generated by flywheels mounted inside the sphere will cause an opposing torque onto the sphere itself. The spinning motors provide a force, and according to Newtons' third, a force is applied back, resulting in the opposite change of momentum of the sphere. However, it is important to note that the rotation of the sphere is not a direct consequence of the angular momentum of the flywheels, but rather of the impulse needed to spin them.

Laboratory Setup

We built a prototype called L.U.N.A (abbr. "lasermapping unidirectional navigation actuator") using the concept described above to test if the IBCOAM drive reliably moves a spherical robot in one direction. Figure 3.5 shows a CAD blueprint of the overall interior layout of the mechanical structure of the L.U.N.A sphere, ignoring the outside shell, flywheels and wiring. The images in 3.6 show the prototype with and without the outer shell. In both images, flywheels are attached to the motor. A low cost LMS-100-10000 laser scanner as well as an IMU system is mounted in the inside to the supporting structural components which are made of acrylic glass.

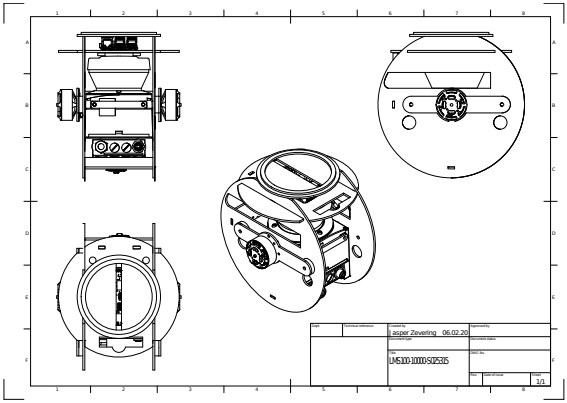

Figure 3.5: Blueprint showing the mechanical structure of the L.U.N.A prototype

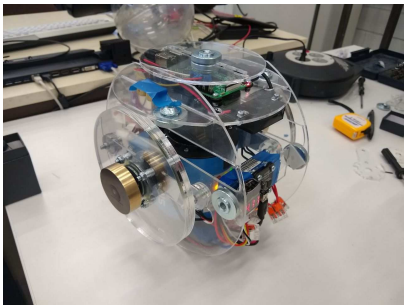

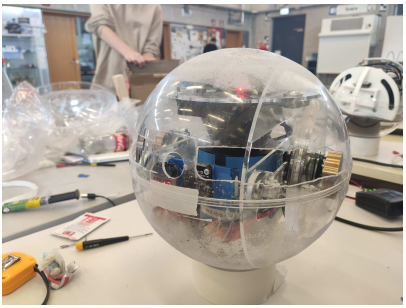

Figure 3.6: Images showing the L.U.N.A prototype without outer shell (left) and with outer shell (right)

Test Results

The conversation of angular momentum drive accelerates the L.U.N.A. sphere reliably. Figure 3.7 shows the angular velocities of the whole sphere measured by the IMU system in one test run. Furthermore, it shows that the velocities along the rotational axis of the flywheels rises while the velocities along the other axes remain lower, albeit are noisy. The vibrations and tilt of the robot contribute to the velocities along the non-rotating axes. However, the vibrations are results of inexact drilling of the flywheels such that there is an unbalance.

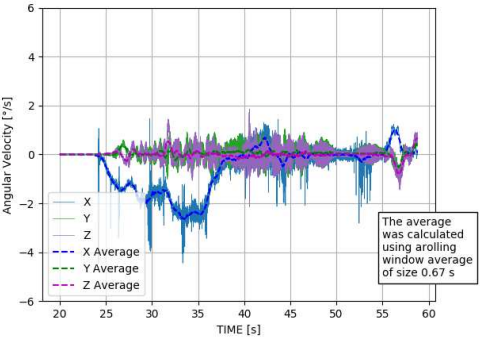

Figure 3.7: Angular velocities of the sphere in 3 axes. Motors start rotating at t = 23s

Shortcommings

Although the results mentioned above are a great proof of concept, the IBCOAM drive is not the choice we propose for the final design due to the following issues.

First, the power consumption is too high since the torque generated to impell the sphere has to be within the order of magnitude of the spheres overall weight. This is an inefficient way to drive the sphere because with the IBCOAM concept there is no way of maintaining the achieved movement. Instead, the flywheels velocities need to be desaturated in order to generate a large torque in the same direction over and over again. Furthermore, the impulse (i.e. the acceleration of the flywheels) has to be as instantanious as possible to maximize the torque on the sphere, which increases power consumption even more.

Second, the drive is too unprecise since with the presented setup there is no reliable way to drive curves or correct the orientation once the sphere falls to one side. However, even with a curve driving mechanism built in the mobility of the sphere still is unflexible because it is unable to change its direction on one spot, which exacerbates object avoidance.

3.1.3 Locomotion by Mass Distribution

Concept

This approach is based on the idea of shifting the center of mass of the sphere to cause rotation. When the center of mass of a sphere is not directly above the point of contact between the sphere and the ground, the sphere will roll until its center of mass and the point of contact are realigned. Shifting the center of mass of our sphere is achieved by two motors which attach the

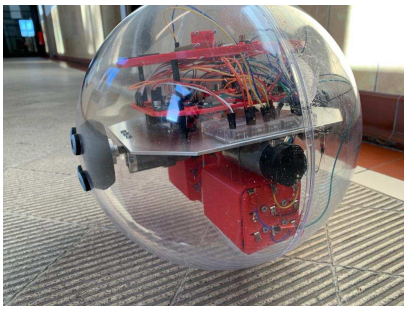

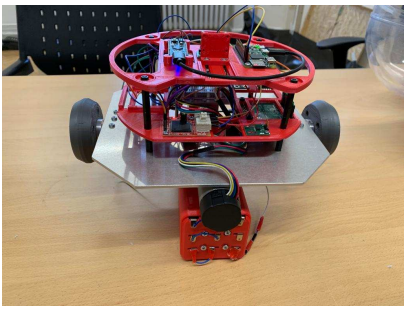

Figure 3.8: Images showing our prototype based on a shifting center of mass

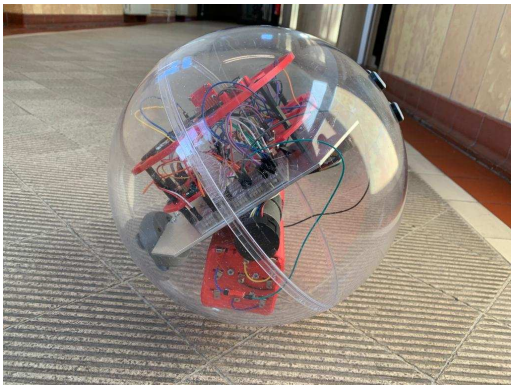

Figure 3.9: Our prototype with off-center pendulums and prepared to move in an arc

outer sphere to the inner structure. When these motors rotate, the internal structure rotates as well and causes the the center of mass to shift. Steering is achieved by two additional motors which move parts of the internal structure perpendicular to the line of motion and causes the center of mass to shift left and right.

Laboratory Setup

Figure 3.8 shows our prototype which demonstrates an implementation of this concept. We used two motors to attach the inner structures to the outer sphere. In addition to mounts for the different boards, the inner structure also consists of two pendulums which are responsible

for steering. These pendulums are attached to the rest of the inner structure by motors which rotate on an axis parallel to the direction of motion. The batteries are housed within these pendulums to increase their weight and their contribution to the position of the sphere's center of mass.

Our prototype executes forward and backward motions in small steps. Each step consists of rotating the motors connecting the outer sphere to the inner structure for a fraction of a second and then stopping the rotation for the same duration. At the end of each step the sphere rolls forward as a consequence of its center of mass having shifted over its point of contact with the ground. Smooth continuous motion is achieved by reducing the duration of each step and concatenating a large number of steps.

Steering is controlled by the position of the pendulums. When the pendulums are positioned off-center, the sphere tilts in their direction until its point of contact with the ground is directly below its center of mass. Fig 3.9 shows our prototype in such a position. Any forward or backward movement at this point is arced in the direction of the sphere's downward tilt.

Results and Shortcomings

This setup reliably drives the sphere in a motion whose speed/direction is controllable but is restricted to straight lines and arcs. While the sphere executes straight line and arced motion satisfactorily, it ends motions with some wobble that causes it to turn away from the direction of motion. This cannot be simply compensated for after the movement since our design does not allow for rotation on the spot. We have observed that the wobble increases as the length of motion increases. By limiting the distance traveled by the sphere in one motion we have managed to limit how far the sphere turns away from its direction of motion.

3.2 Sensing

3.2.1 LiDAR Subsytem

Concept

LiDAR is a method for measuring distances (ranging) by illuminating the target with laser light and measuring the reflection with a sensor. Differences in triangulation angles or in laser return times of laser pulses or observed phase-shifts and wavelengths can then be used to make digital 3-D representations of the target. It has terrestrial, airborne, and mobile applications. A key issue is the software analyzing the raw sensor data to produce meaningful results.

We propose a LiDAR system as part of the spherical robot in order to measur distances in the environment. LiDARS that use triangulation as the basic work according to the principle are only usable for small distances and cannot be used in the target environment. Time-of-Flight LiDARs that analyze the phase-shift have the potential to measure at very high-data

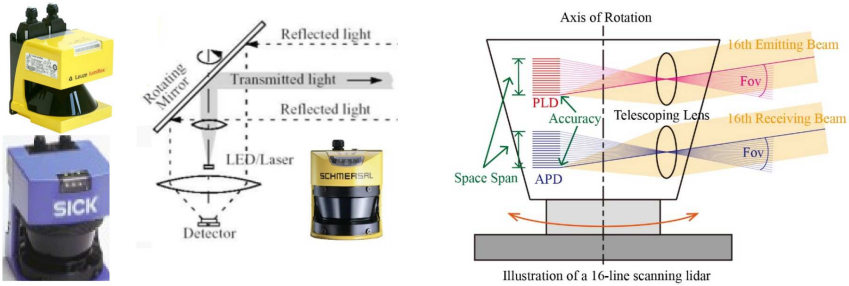

Figure 3.10: Left: LiDAR by rotating a mirror and some well-established examples from industrial automation. Right: Principle of conventional 16-line lidar [91]

rates and obtain high-precise results. While phase-shift-based scanners are well established in surveying, they are not usalble in the target environment due to the inherent unambiguousness range. Thus, DEADALUS will employ a time-of-flight device using a pulsed laser ranger.

3D laser scanning always involves mechenical parts that steer the laser to target locations as well as the actual sensors, cf. Figure 3.10. Typically, a mirror or the sensor head rotates. Mirror-based systems have a large field-of-view up to 360 deg, where a plane is scanned. Smaller FoVs are not possible. Sensor heads with several pulsed laser diode and avalanche photodetectors are difficult to manufacture and to calibrate. To this end, we explore in this study the usage of a prism scanner.

Line Scanner

Figure 3.10 (left) shows a line scanner. We tested such a scanner, i.e., a SICK LMS141 industrial scanner, in a sphere, on a floating desk, rolling on tracks, and free rolling. This is shown in Figure 3.11. The row above shows the sphere rotating. This means, that the translation does not need to be considered. The images below show the resultung 3D point cloud. Applying SLAM algorithms in such a condition is rather challenging, as the overlap between the scan lines is too little, cf. section 5.2 and a different scanning pattern should be considered.

Prism Scanner

While traditional laser scanners have a wide FoV, the point density is fixed for a certain distance. Additional gimbals or other mechanical mechanisms for steering the scanner require more driving energy while non-carried-axis galvanometers have limited aperture sizes [87]. To overcome these issues, we study a so-called Risley prism scanner. Such a cosists besides a sender and receiver for the laser light *two* motorized, rotating prisms for controlling the beam deflectance [150], see

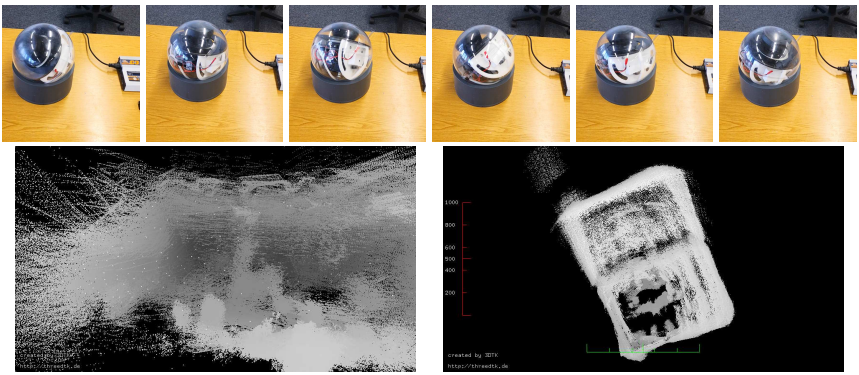

Figure 3.11: Top: Sphere rotating on a floating table. Bottom: Scan matching results. Left: 3D view of the lab. Right: Top view.

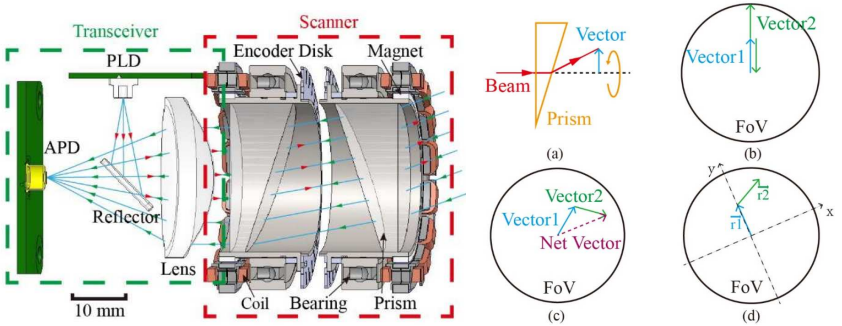

Figure 3.12: Left: Two rotating prisms for controlling the beam deflectance. Right: Scanning principle of prism-based lidar by summing up the deflection vectors. Both images taken from [91].

Figure 3.12. Rotating a pair of Risley prisms with their locations fixed relative to each other traces out a circle with a maximum cone angle of deflection defined by the prism material and wedge angle [87]. The prisms can be made of a single material for single-wavelength operation.

A typical resulting scan pattern is given in Figure 3.13. It displays the pattern integrated at different points in time and as one sees it becomes more dense. The shape of the pattern is adjustable by the rotation speed of the prisms [150].

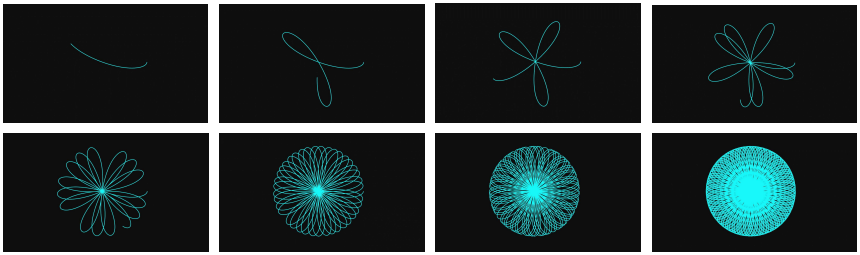

Figure 3.13: The scan pattern becomes denser over time.

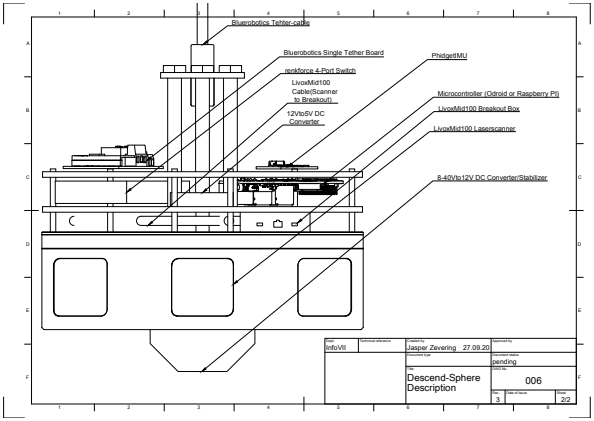

Figure 3.14: Blueprint showing the hardware setup used for testing the LiDAR subsystem.

Laboratory setup

In order to test the performance and reliability of the LiDAR subsystem we used one Livox Mid-100 laser scanner (basically consisting of three individual laser scanners put together to increase FOV) which has the technical features described in table 3.1. The blueprint in 3.14 describes how we implemented the hardware setup.

We connected the laser scanner to an outsourced processing machine via a 50m tear-resistant tether cable (Fathom ROV Tether by BlueRobotics) which we rolled around a coil in order to perform the descending and ascending movement of the sphere, as shown in figure 3.15. A spin encoder measures the rotation of the coil which directly corresponds to the height of the sphere according to the helix arc length formula. That way we estimate the position (only in

Table 3.1: Features of the Livox Mid-100 LiDAR.

Laser Wavelength	905 nm
Detection Range	90 m @ 10% reflectivity 130 m @ 20% reflectivity 260 m @ 80% reflectivity
Horizontal FOV	98.4° (3 × 38.4°)
Vertical FOV	38.4°
Angular precission	0.05°
Detection range	260 m
Range precission	0.02 m
Point rate	100.000 pts/s
Temperature range	−20°–60° C
Input voltage	10–16 V
Operating power	> 60 W

one direction) of the laser scanner. We use a Phidgets 3/3/3 Spatial IMU to gain information about the orientation of the sphere. A voltage stabelizer keeps the input voltage for the laser scanner constant at 14V.

Test run and results

We used the LiDAR setup described in 3.2.1 to conduct a test run in a firestation building, which allowed us to test the reliability of the descending mechanism as well as the quality of the 3D point cloud. The descent of the sphere covered a distance of 22 m (see figure 3.15) and was performed in a duration of 402 s. The cable introduced some non-linear rotations in both directions to the sphere, as chapter 6.2.2 describes this in more detail. During descent, the sphere recorded the scan data of the laserscanner as well as pose information of the IMU. Post processing of this data results in a 3D point cloud of the building. For comparison a reference point cloud was recorded with a terrestrial 3D laser scanner. A second test run, performing the ascent while covering the same distance in a duration of 258 s, yielded faster rotations, making the resulting point cloud very noisy and barely usable.

Figure 3.16 shows a view of the two 3D point clouds as well as a top view of the entire scene. The general geometry of the scene is well captured with the test sphere. Towards the left wall in the top view an increase in the noise level becomes visible. Figure 3.17 gives a quantitative analysis of the results by displaying the distance of the points to the closest point in the reference scan. The majority of the points has a distance of less than 20 cm to the reference scan. A lot of

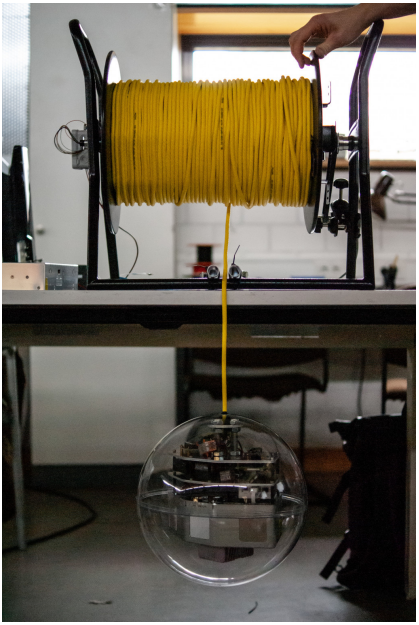

Figure 3.15: (Left) Laboratory setup showing the connection of the laser scanner with the tether cable that is rolled around a cable reel. (Right) Image showing the test sphere as it gets descended 7 floors of a firestation building.

the points with a larger distance are in areas that were occluded for the terrestrial scanner. A slight decrease in accuracy is visible in the far corner. A further source of error is the different behavior of the two laser scanners on the windows. Figure 3.16 shows that the test sphere captures significantly more points on the windows than the terrestrial laser scanner.

The comparison in Figure 3.17 shows that improving the 3D point cloud quality should definitely still be an objective for future studies. To improve 3D point cloud quality, the following roadmap is given:

- Improving pose estimation
- Establishing a robust time synchronisation between scan and pose
- Developing a post-processign algorithm to remove noise, outliers and corrupted scans

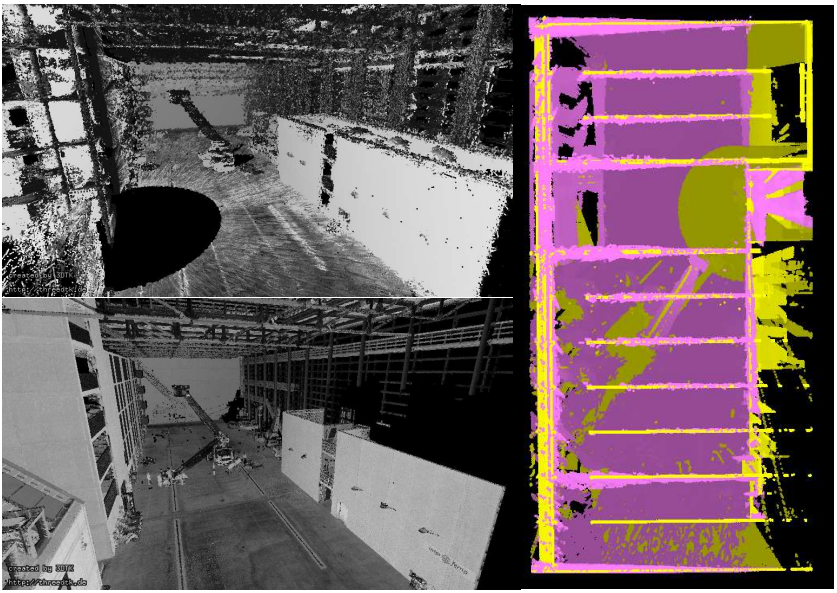

Figure 3.16: 3D point clouds of the fire station building. (Left Above) A view of the 3D point cloud acquired by the test sphere during descent and processed with 3DTK. (Left below) Reference 3D point cloud recorded by stationary RIEGL 3D terrestial laser scanner and post processed with 3DTK. (Right) Top view of both points clouds. For a better view of the scene the ceiling and reflections from the windows have been cropped. The data captured with the test sphere (magenta) represents the geometry of the environment well. Towards the left wall the noise level increases.

- Designing a rotation resistant cable to minimize the chaotic nature of load rotation (as described in chapter 6.2.2)
- Identifying other sources that lead to noise and outliers

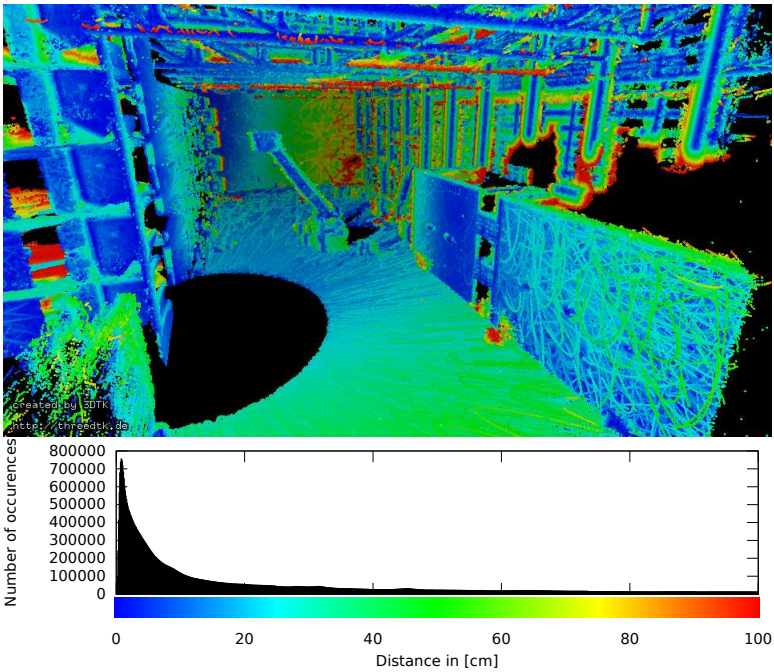

Figure 3.17: (Above) The 3D point cloud acquired by the test sphere compared to the test scan of the fire station building. (Below) A histogram showing the number of points with a given distance to the reference and the color scale used to color the point cloud.

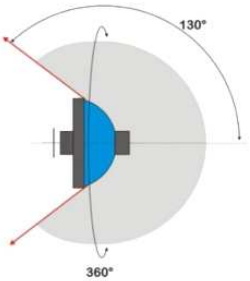

Figure 3.18: Hyperhemispheric lens FoV diagram.

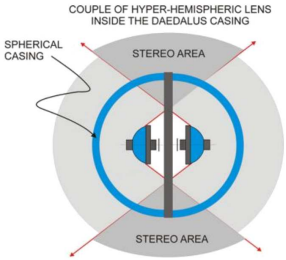

Figure 3.19: Hyperhemispheric lens FoV diagram

3.2.2 The Camera Subsytem

Aim of the Study

We propose to use two hyper hemispheric lenses mounted inside the spherical robot in order to map the whole environment and have stereoscopic capabilities in the lenses equatorial region.

Basic Concept

An hyperhemispheric lens (see [118] for details) has a field of view (FOV) of 360 deg $\times$260 deg, as depicted in Figure 3.18.

Putting a couple of lenses inside the robot permits to have some stereoscopic capabilities in the equatorial plane of the lens, as shown in Figure 3.19.

During the cave descending phase, the lenses could be mounted in the setup shown in Figure 3.20 (TBD).

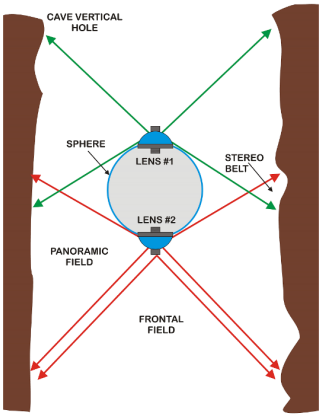

Figure 3.20: Descending phase scheme showing the frontal filed (in front of the below camera) the panoramic field (all around) and the stereo belt (overlapping region of the two FoVs).

Laboratory Setup and Image Acquisition

In order to test the stereoscopic capabilities of a such couple of lenses, we realized a laboratory set-up (see [118] for details), with the two lenses mounted of a steady mechanical frame with a vertical baseline of 80 cm, as shown in Figure 3.21. The image sensor has a 2/3" format, with 2k×2k resolution with a pixel size of 3.5 μm and a color RGB Bayer pattern based matrix.

Actually two hyper hemispheric lenses are available (we have just one) and the we have tested only the panoramic field ($+60\,\text{deg} / -40\,\text{deg}$ degree around the lens horizon). However, this is the most critical field and the one dedicated to stereo propose; in any case the results are meaningful for the whole field.

For calculate the stereoscopic parameters we realized a chess board to frame at different field position. This method (normally call Zhang calibration, see also [138], [139]) is well known in indoor ambient and the same approach was also applied in planetological field for the stereo validation of the STC/SIMBIO-SYSstereo camera calibration (see [118] for details). An example of the images acquired is shown in Figure 3.22. The left image shows the panoramic field for the upper lens, while the right panel shows that for the lower lens. We acquire 63 couple of images (126 total) and analyze the results. Once operating the image dewarping (software correction of distortion and anamorphism) a typical linearized filed is shown in Figure 3.23. The common field between the upper and lower lens (40 deg) is also shown by the central band of the Figure. Here stereoscopic information may be retrieved.

Figure 3.21: Laboratory set-up simulating the stereo block with panoramic cameras. In red the two optical heads.

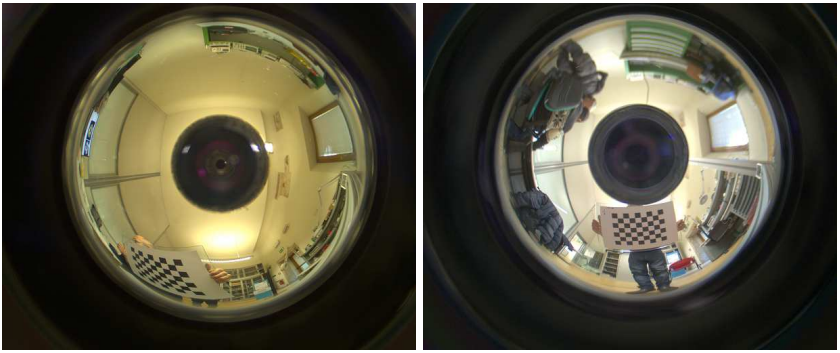

Figure 3.22: Example of two images acquired in our laboratory during the stereo block test by below camera (on the left) and upper camera (on the right)

Image Analysis

The angular resolution of the panoramic field is within a range of 1-3 mrad/px (the lenses considered, due to its extremely large FoV, is anamorphic). Images shown in Figure 3.22 are

Figure 3.23: Example of two images acquired in our laboratory during the stereo block test by below camera (on the left) and upper camera (on the right).

processed for the detection of the corners of the chessboard. The dimensional knowledge of this 3D points allows:

- to model the camera
- to measure the relative position of one optical head respect the other.

Thanks to these measurement it is possible after photogrammetric process to triangulate the images features and perform a 3D reconstruction. An example of target corners detection for one image is shown in the Figure 3.24. Corners are detected with a satisfying detection rate of 95%.

Test Results

The performances of the target and extrinsic calibrations can bewell understood by analyzing the residual of the projection of the3D corner coordinates through the model defined by intrinsicparameters. The standard deviation of the residuals islimited to 0.47 px which corresponds to the resolution of the detection. This means that the camera model and the relative positions between the cameras are correctly measured hallowing in future the best triangulation during the stereo reconstruction.

After intrinsic and extrinsic calibration (as described also in [118]) we summarize the results as in Figure 3.25.

The top panel of the figure shows the VA (vertical accuracy) of the camera with respect to the distance of target from the robot (up to 5 m), parametrized for different baseline (0.25 m,

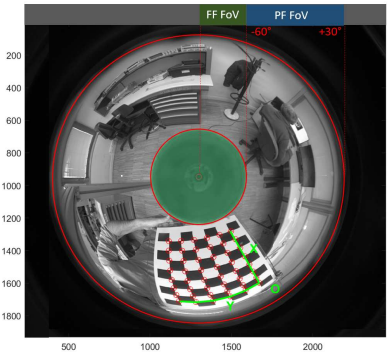

Figure 3.24: Example of the results of the detection of the targetcorners for an UP image. Labels show the limits of the Frontal Field (here not acquired) and the Panoramic Field.

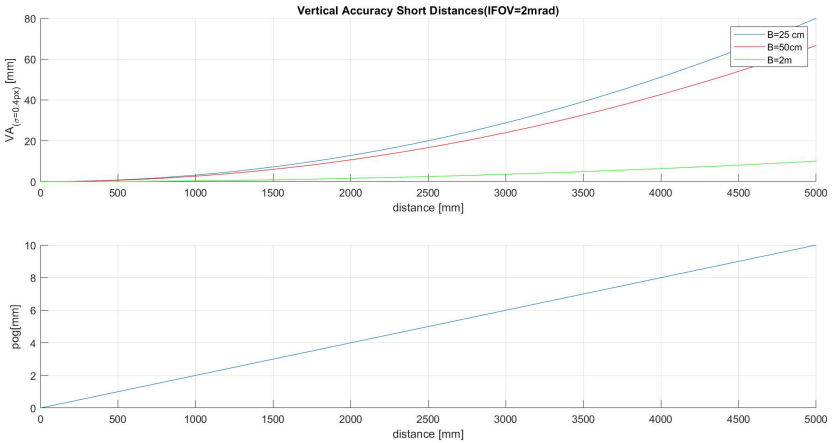

Figure 3.25: Upper plot show the VA (considering a nominal matching error of 0.4 px for three cases considered: in green a baseline of 2 m, in red the 50 cm and in blue the 25 cm. Lowe plot shows at the same distance from the camera the pixel resolution (not depending by the baseline).

0.5 m and 2 m). The baseline (distance between the optical heads) is obviously depending by the dimension of the payload The bottom panel shows the pixel-on-ground resolution with the

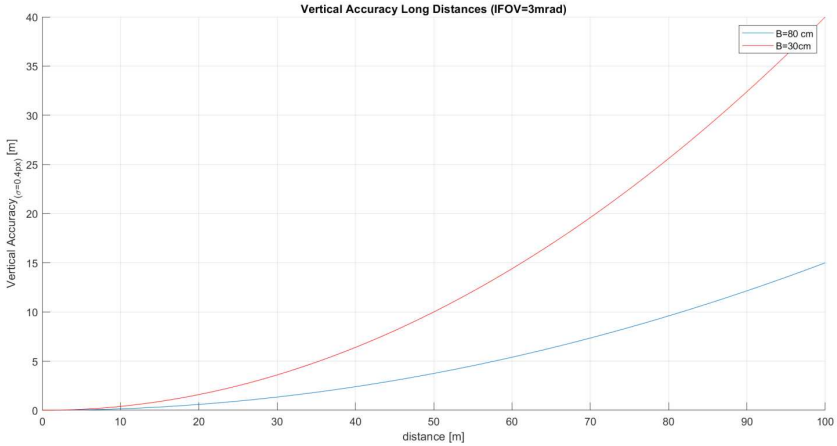

Figure 3.26: Same diagram reported in Figure 3.25 but extended to high distances (more common in a outdoor ambient)

present detector (2k×2k with a pixel size of 3.5 μm) and a baseline of 25 cm. As we can see a resolution of 1 cm is reached for a robot-target distance of five meters. An extrapolation of the VA up to 100 m distance is shown in Figure 3.26.

3.3 State Estimation

The overall pose will be combined out of knowledge of the pose of the SLAM and IMUs. For the pose out of IMU-evaluation, three separate IMUs keep track of the pose of the sphere. Each IMU is placed so that the IMUs Z-axis corresponds to one possible rotation axis of the sphere. Therefore, each IMU is perpendicular to the other two. Combining the axes measurements leads to a "virtual" IMU, which emulates being an IMU positioned at the sphere's center. Hence, isolating the measurements of the resulting virtual IMU to only the rotation in the given axis. Previous prototypes have shown that transforming the data of only one non-centered IMU leads to lower quality measurements. However, combining three IMUs, where each measures only the static rotation around one of their rotational axes (which also represents a sphere's rotation axis), leads to less noise. Each IMU has its own pose estimation for a plausibility check. In case of failure of one IMU, the filtered pose of both working IMUs will provide the pose. This leads to a good estimation and high redundancy of the IMUs. The poses of the IMUs and SLAM will be combined in a suitable filter-structure like the extended Kalman filter. During descending

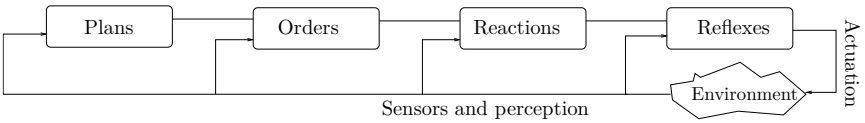

Figure 3.27: Elements for robot control. The connections without arrows point at mutual influence.

the IMUs of the cable can be taken for even more inputs to the filter.

3.4 Autonomous Navigation, Obstacle Avoidance and Exploration

A further issue of our spherical robotic system is navigation, including exploration. In general every goal-oriented action is based on some form of planning: Where do I want to go? How do I get there? If for an robotic system the main task is to go from A to B, then the path must be planned. If there exists no such B then it has to be computed before. And last but not least, the vehicle is supposed to avoid unexpected obstacles while driving the computed path. All of these tasks are subsumed in mobile robotics under the term *navigation*.

How are plans for robots created and how is their execution monitored? One has to be aware, that all information for a robot is incomplete and imprecise. Thus, the plan based robot control must regard this. Having a path from A to B successfully computed does not mean that the robot is supposed to know everything down that was unknow at the time of planning the path. Using a planning module in the robot control does not mean that the robot insists on the plan – there must be further modules which modify the plan according the the current situation. Modifying does not mean to abandon the plan once an unexpected event occurs: For example, if there is a (large) rock on the path of the sphere, it can be pushed away or circumnavigated.

It is difficult and a currently not completely solved problem to fuse the information from a plan, e.g., a planed path, with the requirements of a robot control architecture, to to react on unexpected events and to deviate from the plan without loosing the goal from the plan. Most commonly, the control loop in Figure 3.27 is used. The figure does not specify, how components influence each other precisely, but the influence is mutual: Information about a planned path yields the driving order, but the information from a driving order, especially if an order fails due to a closed door, is fed back into the path planner.

In the depicted elements of a robot control, there are differences concerning the abstraction and time scales and different levels can be identified: Plans, orders, reactions, and reflexes. Figure 3.28 presents the orders of magnitude. Plans are long term task and have to be monitored occasionally. By using reactions and reflexes, the robot control is supposed to act quickly on

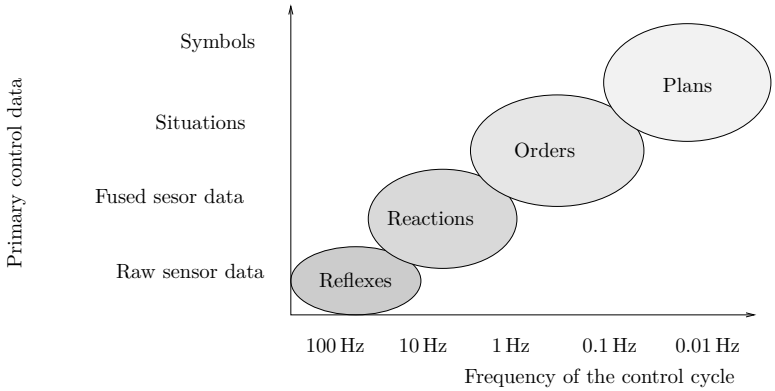

Figure 3.28: Orders of magnitude of control cycles.

requirements from the environment. Reflexes change most rapidly sensor input to control signals. Often they are implemented in hardware, for example emergency stops, contact sensors or safety laser scanners. Here the vehicle stops immediately. Reflexes override other control signals. Reactions also use directy sensor values for control, but they might be pre-processed or fused. Reactions form the basis for the so-called behavior-based robotics. The name originates from the fact that single behaviours are implemented in a separate software module, which are called behaviors. All software modules are fed with the sensor data and wait until they are activated to produce control signals. These output signals are then fused and an overall behaviour is created.

Some tasks can be solved by pure behaviour-based robotic without having orders or planning components, especially the basic tasks of a robot like obstacle avoidance or precise navigation to a goal pose. Other taks like path planning are difficult to solve in a behaviour-based fashion: A modul for path planning uses a map and computed a path from the current vehicle pose to the goal pose. This path is divided into smaller parts or driving jobs are generated. These orders are excuted one by one, where reactive modules ensure that no order is missed. Such a scheme is given in Figure 3.27. This way a telematic control, i.e., taks-level supervisory contral can be established ensuring safe operation of the robot with a ground station on earth.

Path planning methods for robotic systems can directly be used for exploration planning. For exploration goal or target positions are computed given the current map. Crucial for computing these goal positions are the borders between explored and unexplored areas, which are called frontiers. Based on the frontiers, the possible information gain of candidate goal position can be evaluated [26, 50, 110, 145].

For path planning in mobile robotics one choses often the following representation: One reduced the vehicle to a holonomic point without orientation and enlarges objects in the metric map by halve of the robot radius. Thus, areas where the vehicle cannot drive become inaccessable. For such a representation there exists three classes of path planning methods: road maps, grid maps and potential fields. All these methods are well-established [71].

3.4.1 Sensor Placement Planning

Sensor placement planning is needed for the goal directed acquisition of 3D data. The task of a sensor placement planning algorithm is to find a set of sensor configurations needed for obtaining a detailed environment model. Since a typical 3D laser scan takes 3 to 5 minutes for one position, depending on the resolution, it is desirable to minimize the number of scanning positions. This leads to an optimization problem similar to the Art Gallery Problem (AGP) (where to place guards such that the entire gallery is guarded) [113]. The AGP problem is NP hard and is usually solved by heuristics that perform well in practice [59]. These methods are categorized as model-based sensor placement planning (*a priori* model of the environment is known) and non-model-based methods. The latter are applied for exploration tasks in which the robotic system has to navigate autonomously in an unknown environment and build its own model. The planner must determine the next-best-view (NBV) based on the information collected from previous scans. Most exploration strategies push the robot onto the border between explored and unexplored regions [52, 151]. The majority of exploration algorithms is not reliable when applied under real conditions due to the sensitivity to uncertainty of measurements, localization, and map building. A small divergence in localization at the pre-computed NBV point can lead to many unnecessary movements. Moorehead et al. include the uncertainty of the robot pose into the exploration strategies [107]. Recently, numerous sensor placement planning algorithms have been developed for the reconstruction of 3D environment models. Most methods take 3D scans based on a 2D exploration strategy [145]. For creating a full 3D thermal model of a building it is essential to consider the 3D geometry of the environment to ensure that all parts of the building are mapped. Blaer and Allen propose a 3D NBV method which plans additional viewing locations based on a voxel-based occupancy procedure for detecting holes in the model [21]. Low and Lastra present a full non-model-based 3D NBV method based on an exhaustive hierarchical 3D view metric evaluation [95]. However, the computational complexity is still the major challenge in designing practical autonomous 3D NBV solutions.

A sensor placement planning module will enable the full autonomous exploration in order to acquire a dense 3D model of the environment. An algorithm based on the 2D horizontal plane in the point cloud at a specific height can be used efficiently for a rough approximation. However, this will not be sufficient for creating a complete 3D model. Consequently, if the aim is to have a complete 3D model, a method that searches for unexplored areas in 3D is needed.

Implementing and applying a complete 3D sensor placement planning algorithm in a large

cave environment needs significant memory space for storing the occupancy information of the whole environment. One would also need to store the exploration status of each part of the environment. All together this stretches the memory demands a lot. Additionally, the computational effort needed to process all the stored information will be high and increases the exploration time.

Assuming that at least one intial 3D scan of the environment has been taken. From the available scans the initial 3D model is built and the exploration continues by using the 3D model based NBV planning algorithm. The main idea of the autonomous 3D NBV planning algorithm is described in [26].

To obtain NBV positions the 3D model needs to hold information of the explored and unexplored area inside the cave. We propose a voxel based 3D model where each voxel has one of the following labels: *occupied* if the volume within the voxel is occupied, *unseen* if the occupied status of the voxel is unknown or *empty* if the voxel is empty with no obstacles inside. The dimensions of the cave define the number of voxels that should be used to cover the whole area of the cave, i.e., memory allocation for the detected environment. The shape of the enclosed space is arbitrary. A cuboid 3D voxel model that encloses the entire detected space is chosen. The voxel model has to be large enough to enclose the largest area expected in the environment.

The voxel based 3D map is initialized with all voxels set to *unseen*, since we do not have any information on the environment. The update for every 3D scan is performed by using the ray tracing algorithm which traces a ray from the position where the scan was taken to each data point in the scan. Each voxel that is crossed by the ray is marked as *empty* and the voxel containing the data point is marked as *occupied*. The potential NBV position candidates are all voxels at the height of the laser scanner with the status *empty*. Position candidates that are not reachable for the robot are then removed from the list. The aim of this strategy is to choose the candidate scanning position from where the most *unseen* voxels could be seen. For each candidate scanning position we count the number of *unseen* voxels. A ray is traced from the candidate scanning position to each *unseen* voxel and, if all crossed voxels are *empty*, the counter is incremented. Since considering every *unseen* voxel is unnecessarily time consuming only *unseen* voxels with at least one *empty* neighbor are taken into account [21]. In that way the number of voxels that need to be tested is decreased and voxels outside the room boundaries are not considered. The approach is similar to the jump edges in 2D in the way that *unseen* voxels that are taken into account actually corresponds to jump planes which divide explored and unexplored regions. Constraints in the field of view and range properties that are limits introduced by the sensors are considered by checking the range and the angle between the candidate scanning position and the *unseen* voxels.

If the constraints are not satisfied, the *unseen* voxel is not counted. After finding a location that maximizes the number of unseen voxels, i.e., the NBV position, the robot drives to it, takes the 3D scan, and the whole procedure is repeated. The algorithm stops when the number

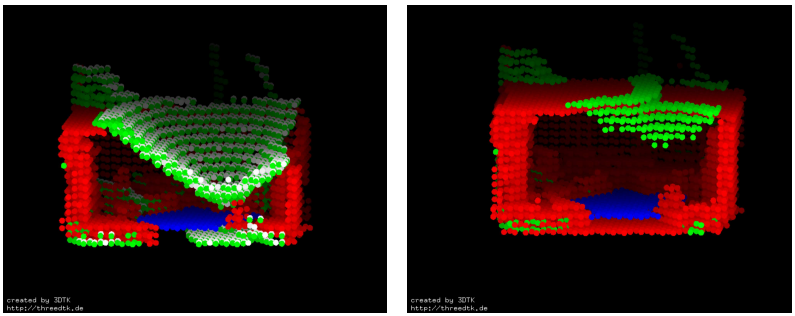

Figure 3.29: 3D voxel based models of 3D scans. *occupied* voxels are colored red, potential position voxels (*PP*) are colored blue, *unseen* voxels are colored green. White voxels are unseen voxels that can be seen from at least one *PP* position in the workspace. Left: Initial model of a room after one scan. Right: Final model of a room after three 3D scans. Images taken from [26].

of *unseen* voxels that can be seen from the best candidate position is below some predefined threshold V_{min} and the room is considered explored.

Chapter 4

Geology and Spectral Requirements

4.1 Science Objectives

Being Dedalus mission devoted to pit and lava tube exploration the main science objectives can be listed as follows

1. Exploration of the evolution of volcanism through windows within the lava flow successions on lunar maria.
2. Identification and characterization of potential paleo-regolith layers and pyroclastic deposits.
3. Detection of fresher rocks and outcrops from deeper locations less affected by space weathering.
4. Generatation of a 3D map based on LiDAR and SfM data of pit walls and lunar caves
5. Verification of the volatiles' presence within the cave.
6. Research of locally sourced resources that can be integrated in crewed missions architecture.
7. Definition of subsurface environmental conditions.

Most of these points (1,2,3,4) being focussed on the analysis of lavas emplacement mechanisms, and volcanic layering and composition specifically address the ESA Moon exploration objectives related to the understanding of the lunar surface and subsurface geology and mineralogy. In addition point 5 is specifically dedicated to volatiles and point 6 to the Identification and characterisation of potential resources for future exploration. Although the volatiles quest is at the moment mainly focussed to the cold traps in the polar regions of the Moon, lava tubes could

be an interesting additional site of permanent shadows able to trap volatiles for future exploration and use. Finally point 7 aims at defining the environmental conditions of subsurface cave contributing to provide useful data for the characterisation of the biological and physiological sensitivity to the lunar environment. The correspondence between the mission objectives and the goals of the ESA exploration program are in table 4.1. Those objectives will be addressed with geologic and compositional vertical surveying and three-dimensional assessment in the landing / caving site, continuous monitoring throughout the descent of temperature, radiation and dust environment, as well as with the overall environmental and lithological characterisation of the shaft and explored cave portions. On top of this, Daedalus can indirectly contribute to the objective of deployment of geophysical instruments functioning as a station at the bottom of the selected shaft carrying out measurements that can be correlated with eventual additional lander or rover locations active at the time of the mission. Moreover, Daedalus will perform a preliminary survey of the access to pristine samples (protected from space weathering) for eventual follow up robotic and human exploration missions aiming at additional deeper in-situ and sample return analyses.

4.2 Science requirements

In order to achieve DAEDALUS science objectives, panchromatic and color images at a proper resolution must be acquired during the descent and with a dedicated illuminator even within the caves for detailing the subsurface geology and detecting fresher rocks, diverse volcanic emplacements, paleoregolith layers and pyroclastic deposits. A 3D reconstruction at high resolution should be guaranteed by both photogrammetry and LIDAR surveys in order to reconstruct the subsurface stratigraphy and to obtain reliable measurements within the underground caves; LIDAR should be also acquired at different wavelengths so that the related measurements, coupled with the information brovided by the cameras, will consistently enhance the chances of rock discrimination and ice detection. A thermometer, a dosimeter and dust detectors should be part of the payload to constrain the cave environment; finally the mode of motion through Daedalus pods should be used for soil strength measurements. In summary the specific needed requirements can be listed as follows:

- Panoramic images of the pit during descent at a resolution better than 0.1 degree per pixel
- Color images obtained with at least 3 filters in the 0.4–0.9 μm wavelength range
- 3D photogrammetric reconstruction with accuracy of less than 10 cm at 5 m distance
- SLAM (Simultaneous Localisation And Mapping) of the pit during descent with 1k per m^2

Table 4.1: science objectives of Daedalus within the overarching ESA Lunar Exploration objectives

DAEDALUS objectives	ESA exploration programme
Explore the evolution of volcanism through windows within the lava flow successions on Lunar maria	ESA Strategy for Science at the Moon: Near surface geology, geophysics, mineralogy and geochemistry
Generate 3D map based on LiDAR and SfM data	ESA Strategy for Science at the Moon: Near surface geology, geophysics, mineralogy and geochemistry
Analysing fresher samples from deeper locations less affected by space weathering	ESA Strategy for Science at the Moon: Near surface geology, geophysics, mineralogy and geochemistry
Detect the presence of volatiles within the cave	ESA Strategy for Science at the Moon: Characterisation of cold trapped volatiles (not at the polar regions)
Research on locally sourced resources that can be integrated in crewed missions architecture (ISRU)	ESA Space Resources Strategy
Identification and characterization of at least one paleoregolith and pyroclastic deposits	ESA Strategy for Science at the Moon: Near surface geology, geophysics, mineralogy and geochemistry ESA Space Resources Strategy
Subsurface environmental conditions	Fundamental for constraining the mentioned Biological and Physiological effect of the Lunar environment

- Long-range LIDAR survey of the cave from tether and/or tripod position (at least 150–200 m)
- At least 2 LIDAR wavelengths (one on the visible range and the other at around 1500 nm)
- Illuminator for optical cameras in shadowed areas in the pit/tunnel
- Accelerometers for soil strength analysis
- Thermometer for environmental conditions evaluation
- Dosimeter for radiation levels
- Dust detectors
- Expected spectral behavior of the basalt layers

Of particular interest are the spectral requirements for both the camera filters and LIDAR that must be constrained on the basis of the material expected to be encountered during both

the descending and navigation phases of the mission. This specific study is developed in the following section.

4.3 Spectral capabilities Definition/ Response to Scientific Requirements

4.3.1 Expected spectral behavior of the basalt layers

NASA Lunar Reconnaissance Orbiter Camera (LROC) Narrow Angle Camera (NAC) revealed eight layers along the Marius Hills pit wall, ranging in thickness from 4 to 12 ± 1 m, with an average thickness of 6 m [125]. Though the pit formed in a mare deposits, and layering is likely due to a sequence of basalt flow effusions, the exact nature of each single layer is still unknown. It is plausible that, during the descent, DAEDALUS will be able to confirm the meter- to decameter-scale of the layering and provide fundamental characters such as texture or relative composition of the identified subunits. Such investigation would provide scientific clues on the effusion mechanisms, the cooling history, possible regolith development between flows (paleo-regolith) and on the eventual access to life resources like trapped volatiles.

It has been demonstrated that, using multispectral remote sensing data, a certain number of basalt units can be discriminated within the Marius Hills terrain (e.g. [17]) reproducing the overall stratigraphy of the complex. In particular, the UV/VIS slope, the strength of the 1-μm absorption – which is indicative of the content of femic minerals - and the TiO_2 content can be used as compositional parameters. The estimation of the relative proportion between femic and sialic minerals, for example, provides hints on the viscosity of the lava flows, or the travel efficiency. On the other hand, the absolute average reflectance can provide hints on the grain size and the porosity of possible unconsolidated layers embedded between uncorrelated lava flows. Due to the hosting of ancient samples of solar wind, the discovery of paleo-regolith layers would in future prompt dedicated scientific missions to the Marius Hills pit. Those parameters and properties need to be investigated in the laboratory, rescaling the analytical outputs to the DAEDALUS constraints.

4.3.2 State of the art: unweathered Lunar basalt spectral response

We are investigating the possibility to distinguish basalt layers of different compositions using multispectral data. Such data could come up from multispectral LiDAR as well as coupling narrowband filters to the cameras. The choice of reference wavelengths partly depends on the rising of reflectance absorptions expected for the volcanic material that potentially build-up the pit walls. The peculiarity of lunar mineralogy required a very preliminary study of lunar samples as ground truth, rather than synthetic or terrestrial analogues. Concerning detectable spectral properties via cameras, we considered a simulated distance of 1-10 m from the target and an

output spatial resolution of several hundreds of microns per pixel. At such conditions, most of the output pixels would be essentially constituted by mixed information, and the microcrystalline basaltic matrix would most likely dominate this mixed information.

As a first reference, VNIR spectra of pristine mare basalt samples and mineral separates collected by the Lunar Rock and Mineral Characterization Consortium (LRMCC, [75]) have been used. The suite includes four pristine and unweathered samples of mare basalts [75], which are thought to fit the expected lower maturity of the pit outcrops. Specifically, two slabs of low-Ti Apollo15 basalts (15058 and 15555) and two high-Ti Apollo17 basalts (70017 and 70035) were reduced, obtaining four particulate bulk samples, a portion of which were used for mineral separates. See [75] for preparation details. VNIR-SWIR spectra of bulk particulates and their constituents (i.e., the endmembers) were acquired at the NASA Reflectance Experiment Laboratory (RELAB, Brown University) as bidirectional reflectance (BDR) at 30 degree incidence and 0 degree emergence with a spectral resolution of $4\,cm^{-1}$, from 280 nm to 2600 nm.

We focus on spectra of coarse particulates, i.e. $<125\,\mu$m, which are largely dominated by coarse particles. Fine-grained sample spectra generally display increased albedos and decreased band strengths. Endmember spectra are used to highlight the specific contribution of each mineral in shaping the bulk spectrum. Modal abundances determined from analyses of paired thin sections [75] are reported in Table 4.2 as a rough reference for bulk compositions: pyroxenes and plagioclases are the most abundant constituents of these lunar samples.

Visible and near-infrared spectra of coarse particle samples are shown in Figure 4.1, along with Ilmenite spectra of the two high-Ti lunar samples.

1. Ilmenite, which we consider the first discriminant for basalt layers, act on bulk spectra suppressing the average reflectance, upturning reflectance beyond $1.7\,\mu$m (i.e., mimic the shifting of the typical 2-μm pyroxene absorption center toward shorter wavelength) and decreasing the 1-μm pyroxene absorption depth. In addition, ilmenite spectral rising along UV-VIS wavelength contributes to decrease the spectral slope of the bulk sample in this specific range. Isaacson et al. [75] pointed out that effects of ilmenite on reflectance spectra are similar to some of the optical effects of space weathering.

2. The position of the 1- and 2-μ pyroxene absorptions, which dominates the bulk spectra, depends on the Ca-content, with higher-Ca pyroxenes displaying the absorption center at longer wavelengths.

3. Olivine, which is significantly present in 15555 sample, act on bulk spectrum broadening the 1-μ absorption toward larger wavelengths (i.e., shifting the large-wavelength shoulder position toward larger wavelengths). These discriminants can be retrieved reducing (resampling) spectral information at the following seven wavelength positions: 280 nm, 750 nm, 1000 nm, 1500 nm, 2200 nm, 2600 nm (Figure 4.2).

Table 4.2: Modal abundances of samples considered in this study, determined from analyses of paired thin sections [75]

Mineral Phase	15058	15555	70017	70035
Olivine	0.1	11.8	1.5	1.2
Orthopyroxene	3.7	0.3	-	-
Pigeonite	25.6	32.4	17.7	20.2
Augite	16.7	18.6	34.2	27.7
Fe-pyroxene	17.1	5.4	0.6	1.1
Plagioclase	30.1	27.3	25.7	30.1
Tridymite	3.5	0.8	1.6	0.9
Ilmenite	1.4	1.2	17.3	17.4
Chromite	<0.1	0.4	-	-
Ulvospinel	0.9	1	0.3	0.3
ARmalcolite	-	-	0.1	0.1
Rutile	-	-	0.1	0.1
Troilite/Metal	-	-	¡0.1	-
K-rich glass	0.5	0.4	0.3	0.4
Phosphates	0.1	0.1	0.1	¡0.1
Total	99.9	100	100	100

Specifically, the following standard spectral parameters can be retrieved: the steepness of UV/VIS spectral slope using a 280/750 nm value (alternatively, the 400/750 nm value), which could suggest a difference in layer maturity and/or a relative ilmenite content; the albedo using 750 nm value, which is meaningful of the TiO_2 and FeO (e.g. ilmenite) abundance (e.g. [69]); the strength of the 1 μm absorption, which depends on the femic mineral abundance, using 750, 1000 and 1500 values (e.g. [18]); the steepness of 1500/1000 nm spectral slope, which could suggest the presence of olivine; the depth and asymmetry of the 2-μm absorption, using 1500, 2200 and 2600 nm values, which are indicative of the ilmenite content rather than of the pyroxene content and chemistry. All these parameters need to be further investigated in the laboratory. In this way, we expect to acquire the knowledge to definitively identify proper wavelengths.

4.3.3 Potential OH^- – H_2O spectral response

The spectral behaviour of H_2O in the UV-VIS-MIR range depends on several factors. Basically, H_2O ice exhibits strong absorption in the ultraviolet and strong reflection in the visible, with a

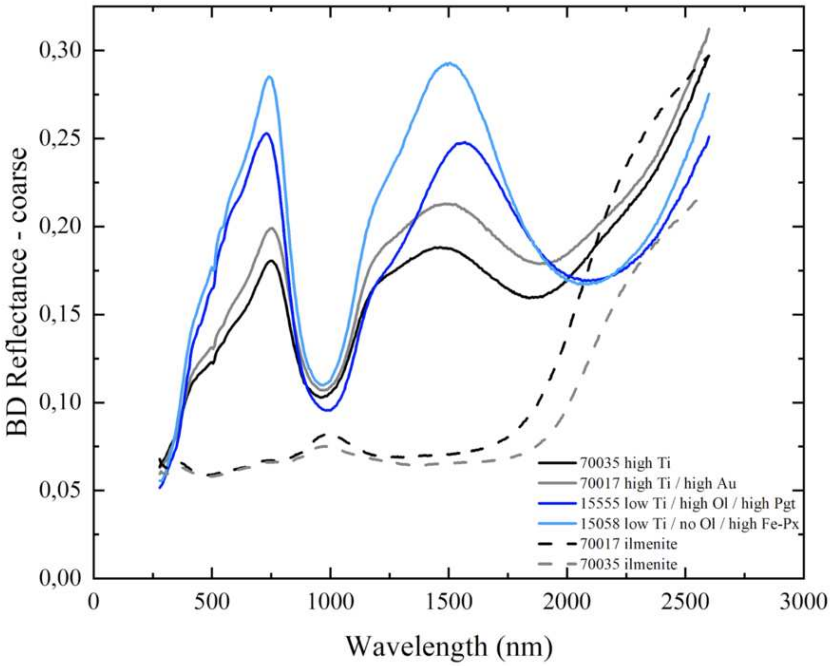

Figure 4.1: BD reflectance of coarse particulates described in 4.2 in terms of modal abundances.

reflection maximum near 400 nm; the absorption is moderate in the 1–3-μm range, with specific bands at 1.5 μm and 2.0 μm, where diagnostic vibrational overtones and combinations of the 3-μm fundamental water molecule vibration lie. Nonetheless, in the 1–3-μm range the OH^- hydroxyl exhibits overtone absorptions indicative of mineralogical hydrated phases [42]. Where 1–3 μm water-indicative absorptions have been detected, the presence of solid water with respect to OH^- bearing phases could be inferred through a 1.5/2.0 μm band ratio: a higher ratio should be indicative that only OH^- is present, whereas a lower ratio should be indicative that water ice is present (Figure 4.3). In general, a low reflectance value for the 1.5 μm wavelength should be indicative of OH^-, therefore we suggest to focus instrument capabilities to this specific wavelength to reveal possible H_2O presence. The 1.5 μm absorption has been already used to evaluate the wet content of clay minerals using a 1535 nm laser [55]. Similar methods have been applied on wet and dry mineralogical aggregates using alternative wavelengths in the 750–1000 nm range

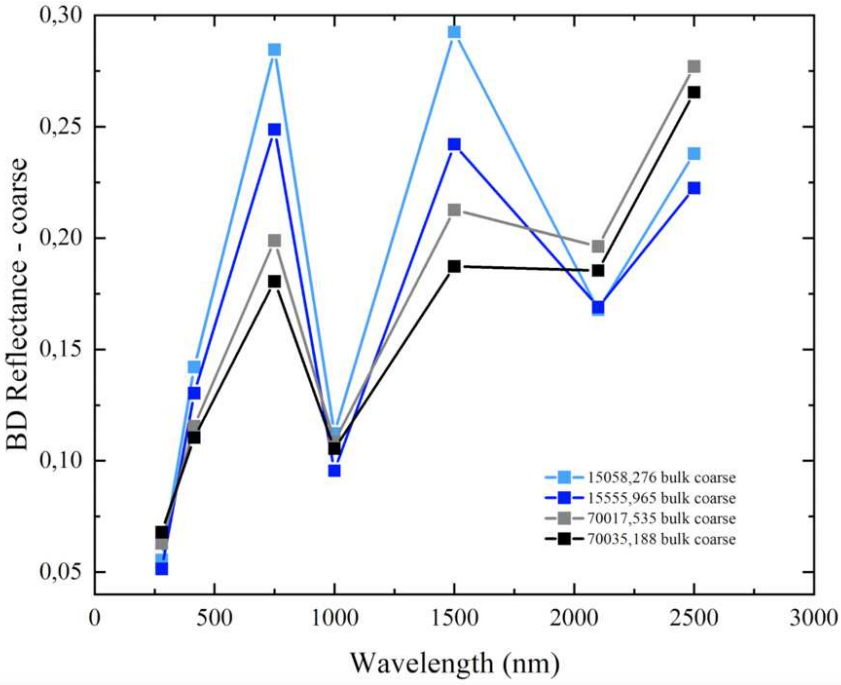

Figure 4.2: BD resampled reflectance of coarse particulates described in Table 4.2

(e.g., [78]).

4.3.4 Optical spectral requirements

Quantum efficiency of the CCD image sensor suggests the range within which signal is valued. The sensitivity (relative quantum efficiency) of the designated CCD is maximised at 500 nm, halved at 400 and 750 nm and less than 10% beyond 950 nm, suggesting to select filters within the 400–900 nm range. In order to retrieve the highest number of spectral parameters, we suggest applying at least four filters centered at 480 nm, 600 nm, 700 nm and 830 nm (see Figure 4.4). Bandpass should be adequately narrow.

The UV/VIS spectral slope (480/700 nm) could be indicative of layer maturity, grain size, ilmenite content: to constrain each contribution, it becomes of paramount importance to test this spectral parameter in a suited set of analogue samples. Reflectance at 700 nm will be

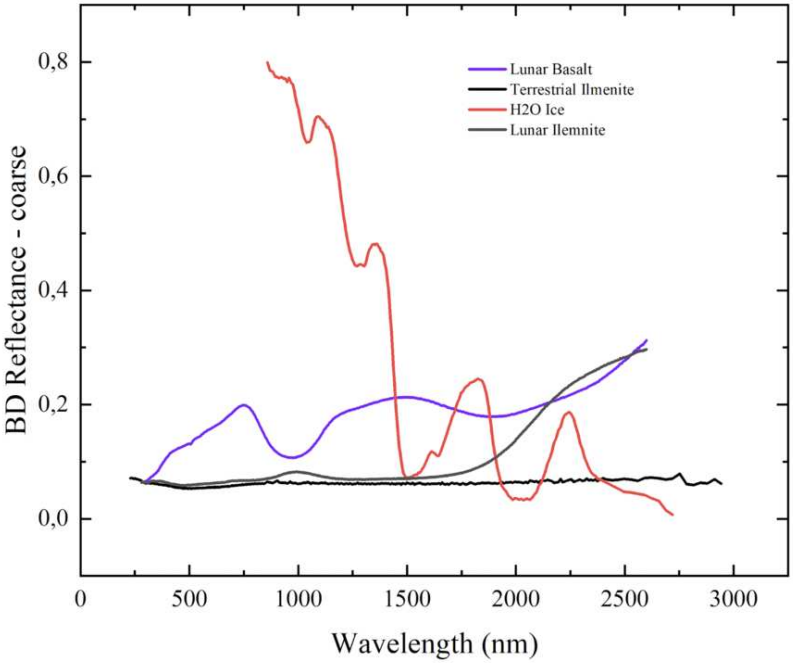

Figure 4.3: BD reflectance of coarse particulates described in Table 4.2 (Lunar Basalt sample 70017,532 and relative Lunar Ilmenite), and BD reflectances of a Terrestrial Ilmenite and H_2O ice from the USGS Spectral Library Version 7 [85]. Any spectral comparison should be qualitative.

negatively correlated with TiO2 and FeO (e.g., ilmenite) abundance. Relatively high reflectance values joined by attenuated 600/700- nm spectral slopes could be associated with a yellow-orange volcanic glass content, suggesting the presence of pyroclastic material. The 830-nm reflectance value coupled with the 750/830- nm slope, which points to the 1 μm absorption strength, is indicative of the mafic minerals abundance. All the spectral parameters must be correctly cross-correlated to achieve compositional information.

4.3.5 LiDAR spectral requirements

LiDAR return signal will be employed for water detection. Ice water reflectance, which is greatest up to green wavelengths, tends to dramatically decrease toward near-infrared wavelengths (4.3),

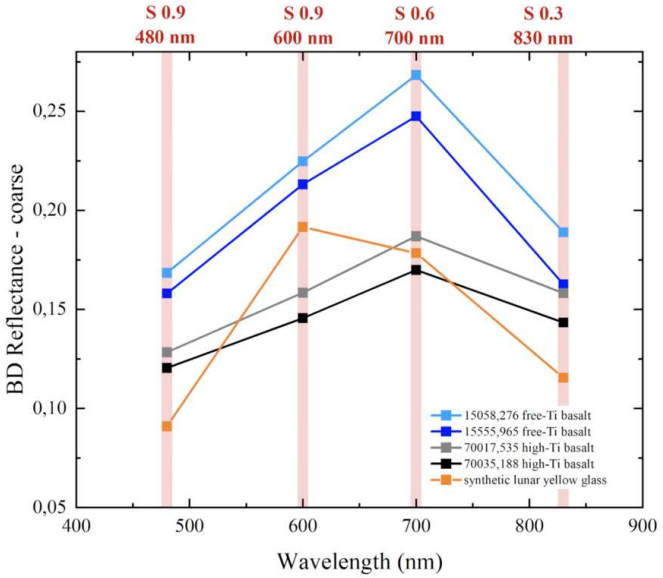

Figure 4.4: BD resampled reflectance of coarse particulates described in Table 4.2, and BD reflectance of a synthetic Lunar-like yellow glass acquired by Ralph Milliken with the NASA RELAB facility at Brown University. Red stripes indicate constrained band centers, sensitivity (S) is reported on the top of each band wavelength.

where water ice competes with ilmenite in reducing the bulk signal. In order to discern water ice contribution by ilmenite contribution, we suggest to use a red/NIR ratio, which is positively correlated with ice content. Specifically, we suggest to use an orange/red laser wavelength (e.g. 657 nm) and a 1535 nm laser, centered where the main water ice absorption arises (Figure 4.5). Concerning basaltic aggregates, it is possible that ilmenite could be qualitatively inferred in cases where the red/1535 nm ratio appears close to one and both intensity values are comparatively low.

4.3.6 Advancements

All the identified spectral properties and parameters need to be investigated in the laboratory, with proper sample suites and dedicated environments, rescaling the analytical outputs to the DAEDALUS constraints.

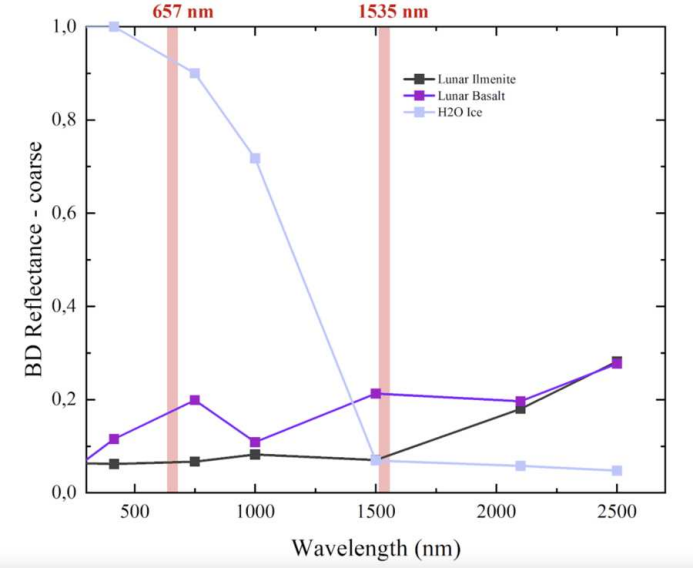

Figure 4.5: BD resampled reflectance of coarse particulates described in table 4.1 (Lunar Basalt sample 70017,532 and relative Lunar Ilmenite), and BD reflectances of H_2O ice from the USGS Spectral Library Version 7 [85]. Any spectral comparison should be qualitative. Red stripes indicate two common LiDAR wavelengths that fit water detection.

4.4 Mission phases and foreseen Science return

The Daedalus exploration will develop following mission phases with a progressive improvement of the science return. They can be summarized as follows.

Phase I): Skylight approach and descender deployment

During this phase Daedalus is thought to be lowered down within the pit using a crane system mounted on a dedicated rover. If a crane, as most likely, is not long enough to suspend the descender directly in the shaft a rolling sphere robot and the LOSYS pod subsystem can overcome the problem, since the marius hills skylight has a sloping portion before the void.

Phase II): skylight descent and mapping

During the descending phase the laser scanner and the panoramic cameras will be used. With the help of an encoder, which measures the tether length, laser data can be used to create an initial 3D point cloud. Redundancy is provided by the stereo section and robot SLAM

and SfM algorithms. Besides context 360 imagery, VIS dual hemispheric cameras will also provide stereo imaging of illuminated overlapping areas as well as close-range imaging, useful for textural characterization of shaft walls' lava layers. At the meantime, thermal-, radiation- and dust-sensors will provide information about the thermal gradient as well as the environment condition within the pit. Radiation and temperature vertical profiles will also be acquired during descent.

Phase III): enter the main void and mapping from the descender tether the main cave environment.

The phase begins at the base of the cave ceiling and ends at the cave floor. The Lidar system should acquire the first 3D point cloud within the cave and the cameras can acquire eventually using both natural and artificial illuminations . Thermal/radiation/dust sensors will work to define the radiation and temperature horizontal profiles At touchdown, the objective of close characterization of the ground with multi-band LIDAR and cameras will be achieved.

Phase IV): Initial navigation and tunnel mapping

During this phase Daedalus will navigate within the cave using tether as a wifi spot. Under ideal condition Daedalus may possibly enter within the lava tube up to at least 200 meters. This is, however, highly dependent on the morphology and geometry of the lava tube, that will be acquired in the descent phase before touchdown. Obstacles evaluation and terrain strength data are to be acquired by passive seismometry with embedded accelerometers (NAV) and extendable pods (LOSYS) acting as Schmidt hammer at touchdown. This mission phase is highly dependent on the contingency of the cave configuration which is highly variable and unpredictable. The deployment and distance of travel of rolling spheres using tether as a wifi hotspot is indeed dependent on 1) terrain roughness 2) obstacles such as boulders 3) radiation and rock magnetisation interfering with the wifi signal.

The cave exploration will be based ton the locomotion subsystem (LOSYS) which works via eccentric mass movements and autonomous pod movements (simplified sea urchin-like) to progress on the cave bottom. Power is guaranteed by the batteries, kept charged during descent via tether, so that all subsystems can work (e.g. HYLI, VIS, etc.). Communication is guaranteed via local Wi-Fi from the solo DAEDALUS sphere and the base of the tether or in its vicinity, e.g. at a certain height above the detachment mechanism. This phase of the exploration bears higher risks.

4.4.1 Science return levels

DAEDALUS mission is designed in order to accomplish progressive scientific return in every phase of implementation after deployment in the skylight. In particular we can subdivide the science return into three different stages:

- The Minimum viable science return is expected to be achieved at the edge of the pit during

the approach of PhaseI and the initial descent of PhaseII.

- The Nominal mission science return will be obtained during the tethered exploration of the entire pit up to the cave floor. This activity includes most of the Phase II during which the pit walls will be carefully explored and the entire Phase III when the cave will be explored in tethered mode.
- The Extended mission science return will be achieved during the tunnel mapping (Phase IV) including the powered solo mode.

  The science return expected at each stage is summarized as follows:

  - Minimum viable science return - Edge of pit - initial descent
    - Surface volcanic geomorphology
    - Characterization of surface regolith
    - First multispectral panoramic views of the volcanic environment at a pit entrance
    - First high-resolution 3D reconstruction of the sky-light entrance
    - First stratigraphic interpretation of a pit entrance
  - Nominal mission science return - Base of the pit, main void tethered exploration
    - First high resolution 3D reconstruction of pit walls and bottom floor
    - First multispectral and rock lithological characterization of pit walls and bottom floor
    - First Stratigraphy of lava flow sequences along the entire pit
    - First Rock mass fracture density estimates for cave stability analysis on the Moon
    - Detections of potential paleoregolith layers
    - Detections of potential pyroclastic deposits
    - Temperature and radiation profiles during descent
  - Extended mission science return - Untethering, tunnel navigation
    - First high resolution 3D reconstruction of a lunar cave
    - First 3D reconstruction for stability evaluation of the cave ceiling
    - Horizontal profiles of temperature and radiation along the tunnel
    - First evaluation of cave trafficability
    - Detection of potential cold traps
    - Cave floor mechanic properties
    - Evaluation of insolation variability within the cave
    - First multispectral images and rock lithological characterization within a lunar cave
    - First textural characterization of volcanic rocks and debris within lunar caves

Chapter 5

Optical Imagery

5.1 Visual SfM and Laser SLAM

To capture the 3D environment the Daedalus sphere relies on two different types of optical sensors, namely cameras and laser scanners. While cameras project their surroundings onto a 2D image plane and acquire data at high frequencies, laser scanners capture accurate depth information and are independent of external lighting conditions. Both of sensors have in common, that they only capture a small part of the environment within their field of view. This chapter describes the algorithms required to reconstruct the full scene based on camera or lidar data.

5.1.1 Structure from Motion

The ability to recover 3D information from 2D images is of high interest. This operation is unfortunately not possible by using a single image due to the fact that depth information cannot be extracted from it without additional information. But using different views of the same scene, this information can be reconstructed by means of triangulation. Structure from motion is a photogrammetric technique to compute simultaneously camera positions and projections from multiple views of a scene, to produce a 3D model of the scene using only correspondences between the different views. In a broad sense these correspondences are found when tracking common features between the views, which can be detected as edges with colour gradients on multiple directions. When matching multiple views, tracking the feature trajectories over time is used to compute their 3D position, as well as the camera motion. Two main alternatives exist for approaching this reconstruction step: incremental structure from motion, that solves the camera poses one by one and adds them into the reconstruction, and global structure from motion, that attempts to solve all of them at the same time. After the reconstruction a sparse 3D point cloud is obtained, which is refined by applying a bundle adjustment that optimizes the initial projection matrices of the views by the means of minimizing a cost function [124]. As a final step, with the 3D pose identified for the features in every view, the depth information can be

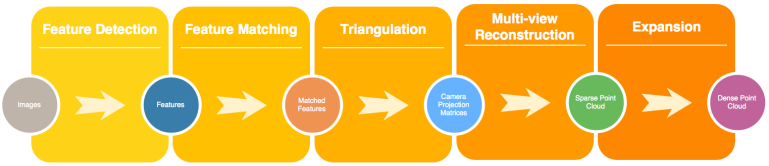

Figure 5.1: Overall process flow of an structure from motion algorithm.

computed for pixels in nearby regions of feature points. This data is used to produce a denser and colourized 3D point cloud as the output of the structure from motion algorithm. Figure 5.1 shows an overview of the data flow of the structure from motion technique.

The first step in a structure from motion reconstruction pipeline is detecting features in a view that are later matched across multiple images to infer the camera position and depth information of the views. For this purpose, a method is required to detect such features that is invariant to image scaling and rotation and also to changes in illumination and camera point of view; to maintain a consistent and stable feature tracking across multiple views. One of the most popular algorithms for this purpose utilized in multiple structure from motion packages is the scale-invariant feature transform (SIFT) [96].

Feature matching, that is, finding the corresponding points in different images of the same object, has proven to be a particularly complicated problem to solve automatically [77]. This is due to the fact that two images may exhibit substantial change of scale of the photographed object, different angles or perspectives or even degrees of occlusion. A possible approach for detecting correspondences in features between different images [13] is to assume that small local patches of surface in the object are subject to only affine transformations (i.e. translation, scale, rotation, skew). It is important to clarify once more that this is not the only solution to this problem, but the one used in this section to illustrate the process of feature correspondence.

The first step in this algorithm is to examine a region in the image centred in a keypoint and calculate a set of characterization values for that region. This involves calculating affine invariants for stretch, skew, photometric intensity changes and rotation effects, using shape-adapted texture descriptors [89]. The output of this algorithm is a feature vector containing 43 invariants describing an image patch for an RGB image.

For matching the patches across images, a Mahalanobis distance metric [98] is used since the features are sufficiently well characterised to use a simple matching scheme. Given two feature vectors $v^{(i)}$ and $w^{(j)}$ and a distance measure $d(v, w)$, the matching algorithm first calculates the distance matrix $m_{i,j} = d(v^{(i)}, w^{(j)})$ between the pairs of features across the two images. For identifying potential matches (i, j), a feature i in the first image is selected in such a way that is the closest one to feature j in the second image, and vice versa. These potential matches are scored using an ambiguity measure [49], that measures the relative distance between the two

matching features and the next closest distance between one of the matched pair and any other feature. Finally, unambiguous matches are chosen or the best n matches according to the score.

It is well-known, that a fundamental matrix that relates a pair of calibrated views can be estimated from at least eight correspondences between them, and how this matrix can then be decomposed to estimate the relative camera orientation and position between the views [93]. This matrix is derived by the means of epipolar geometry. With the relative camera position and orientation estimated, the projection matrices of the cameras can be computed by decomposing the fundamental matrix. Finally, the 3D points are triangulated by computing the intersection of the back-projected rays of the image points between at least two images.

Once that the fundamental matrices have been found between multiple pairs of images and the location of the 3D points in the relative frames of references from all cameras have been computed, the position of all the cameras in a common frame of reference are calculated.

There are two main approaches to this problem. One is solving the positions in a sequential manner, where cameras are added one by one to the common frame of reference using the geometry encoded in the fundamental matrices that describe the relative movement between the camera to be added and any camera already on the common frame. The other tries to solve all camera positions simultaneously. The final step for both approaches is applying a bundle adjustment, which is used iteratively to refine the structure and motion parameters by the minimisation of a cost function [124].

5.2 Laser-based SLAM

For all of our systems, we need a semi-rigid SLAM solution, which is explained in the next section. To understand the basic idea, we summarize its basis, 6D SLAM, which works on single 3D point clouds acquired in a stop-scan-go fashion.

6D SLAM works similarly to the the well-known iterative closest points (ICP) algorithm, which minimizes the following error function

$$E(\boldsymbol{R}, \boldsymbol{t}) = \frac{1}{N} \sum_{i=1}^{N} \| \boldsymbol{m}_i - (\boldsymbol{R}\boldsymbol{d}_i + \boldsymbol{t}) \|^2 \tag{5.1}$$

to solve iteratively for an optimal rotation $\boldsymbol{T} = (\boldsymbol{R}, \boldsymbol{t})$, where the tuples $(\boldsymbol{m}_i, \boldsymbol{d}_i)$ of corresponding model $\boldsymbol{M}$ and data points $\boldsymbol{D}$ are given by minimal distance, i.e., $\boldsymbol{m}_i$ is the closest point to $\boldsymbol{d}_i$ within a close limit [16]. Instead of the two-scan-Eq. (5.1), we look at the n-scan case:

$$E = \sum_{j \to k} \sum_{i} |\boldsymbol{R}_j \boldsymbol{m}_i + \boldsymbol{t}_j - (\boldsymbol{R}_k \boldsymbol{d}_i + \boldsymbol{t}_k)|^2 , \tag{5.2}$$

where j and k refer to scans of the SLAM graph, i.e., to the graph modelling the pose constraints in SLAM or bundle adjustment. If they overlap, i.e., closest points are available, then the point

pairs for the link are included in the minimization. We solve for all poses at the same time and iterate like in the original ICP. The derivation of a GraphSLAM method using a Mahalanobis distance that describes the global error of all the poses

$$W = \sum_{j \to k} (\bar{\boldsymbol{E}}_{j,k} - \boldsymbol{E}'_{j,k})^T \boldsymbol{C}_{(}^{-1} \bar{\boldsymbol{E}}'_{j,k} - \boldsymbol{E}'_{j,k}) \tag{5.3}$$

where $\boldsymbol{E}'_{j,k}$ is the linearized error metric and the Gaussian distribution is $(\bar{\boldsymbol{E}}_{j,k}, \boldsymbol{C}_{j,k})$ with computed covariances from scan matching as given in [25] does not lead to different results [109]. Please note, while there are four closed-form solutions for the original ICP Eq. (5.1), linearization of the rotation in Eq. (5.2) or (5.3) is always required.

5.2.1 Semi-rigid SLAM

In addition to the calibration algorithm, we also developed an algorithm that improves the entire trajectory of the system simultaneously. The algorithm is adopted from [53], where it was used in a different mobile mapping context, i.e., on wheeled platforms not on spherical robots. Unlike other state of the art algorithms, like [143] and [27], it is not restricted to purely local improvements. We make no rigidity assumptions, except for the computation of the point correspondences. We require no explicit motion model of a vehicle for instance. The semi-rigid SLAM for trajectory optimization works in 6 DoF. The algorithm requires no high-level feature computation, i.e., we require only the raw points themselves.

In case of a continuous motion, we do not have separate terrestrial 3D scans. In the current state of the art developed by [27] for improving overall map quality of mobile mappers in the robotics community the time is coarsely discretized. This results in a partition of the trajectory into sub-scans that are treated rigidly. Then rigid registration algorithms like the ICP and other solutions to the SLAM problem are employed. Obviously, trajectory errors within a sub-scan cannot be improved in this fashion. Applying rigid pose estimation to this non-rigid problem directly is also problematic since rigid transformations can only approximate the underlying ground truth. When a finer discretization is used, single 2D scan slices or single points result that do not constrain a 6 DoF pose sufficiently for rigid algorithms.

Mathematical details of our algorithm are given in [53]. Essentially, we first split the trajectory into sections, and match these sections using the automatic high-precise registration of terrestrial 3D scans, i.e., globally consistent scan matching [25]. Here the graph is estimated using a heuristics that measures the overlap of sections using the number of closest point pairs. After applying globally consistent scan matching on the sections the actual semi-rigid matching as described in [53] is applied, using the results of the rigid optimization as starting values to compute the numerical minimum of the underlying least square problem. To speed up the calculations, we make use of the sparse Cholesky decomposition by [46].

Table 5.1: Commercial available dust removal and hard coting technologies.

Technology	Power consumption	Space qualification	Reference
Dust removal			
Electrostatic	Active	No	[3, 148]
Ultrasound	Active	No	[2]
Nanocoating	Passive	No	[24]
Hard coating			
SiO_2 / Al_2O_3 coating	Passive	No	[101]

A key issue in semi-rigid SLAM as well as the ICP-like 6D SLAM is the search for closest point pairs. We use an octree and a multi-core implementation using OpenMP to solve this task efficiently. A time-threshold for the point pairs is used, i.e., we match only to points, if they were recorded at least t_d time steps away. In the experiments described in the previous sections, we have used a maximal allowed point-to-point-distance which has been set to 0.25 cm.

Semi-rigid SLAM transforms all points; points in a scanline via interpolation over the time-stamps. Finally, all scan slices are joined in a single point cloud to enable efficient viewing of the scene. The first frame, i.e., the first 3D scan slice from the Riegl scanner defines the arbitrary reference coordinate system.

5.3 Dust Removal

Table 5.1 shows possible solutions for dust removal and prvides a link to hard coatings of the company Merck. It should be noted, that these technologies are not space qualified yet.

Chapter 6

Final DAEDALUS Design Proposal

6.1 Nomenclature

This chapter provides parametric analysis for a possible final design of the DAEDALUS system. In general, for the tables displaying this analysis an accompanying table is presented containing the approximate margin of errors. Some values have different margin of errors towards higher values than lower values, therefore the nominal values do not have to be the center of the range interval.

6.2 Cable

6.2.1 Components

The sphere-end of the cable has the following tasks:

Mechanical coupling. The sphere is coupled and decoupled to the cable and therefore needs a reliable coupling mechanism. Also, the recoupling process (see section 6.4.4) brings the requirement of some shape for passive alignment, as it will be hard to get to an mm-exact position under the cable.

Wifi RX/TX. The cable end serves as WIFI Access Point at the bottom of the lunar cave.

Pose estimation. The cable has to estimate its pose to enable and improve recoupling.

Light source. The cable holds a light-source that lights 360 degrees while descending. Furthermore, it lights the near environment once at the bottom of the cave while the power comes from the surface (see 6.5.1). Also, the light can be used as a marker for optical tracking for navigation, in addition to the navigation by SLAM.

Voltage stabilization. Because there will be a voltage drop over the length of the cable, the voltage at the bottom of the cable needs to be stabilized. Tests with the third prototype (see section 3.2.1) showed that the difference between the voltage drop with idle and full power consumption is too high to be in the range of all components work. Therefore a stabilizer needs to transform a huge range of voltages to one main working voltage. In the prototype, the working voltage was 12 V, and the stabilizer had an input-range of 8 V to 40 V.

Heating. As the electronics in the cable have themselves an operating range of temperature, a heater is necessary, even if the sphere can heat the cable with its heater over the physical connection during descending. The heater of the cable can heat the sphere over that connection and relieve the heater of the sphere while charging and descending.

Cooling. The cable itself works as a radiator whit a big surface due to its length and, therefore, can redirect thermal energy from the sphere to the cable. The option exists to mount extra fins to the cable to strengthen the cooling effect. This would lead to a higher power consumption of the heater when heating up, as energy will be lost due to the stronger cooling effect at the same time.

6.2.2 Load Rotation

Rotation-Resistant Design

Twisted wire designs, as they are usually used for common electrical wires due to their anti-inductive properties, always keep the risk of inducing rotation on its load. This is because their internal twist establishes a non neglectable torque onto the load proportional to the tension applied to the cable. The effect gets emphasized further since twisting the strands (not only the electrical ones but also the ones exposed to the tensional forces) gives axial strenght whilst preserving bending flexibility, therefore being a reasonable design choice. However, the torques established by the twist of the strands get compensated when using multiple layers of opposite twist, establishing a counteracting torque. Torque also gets minimized when using ordinary lay constructions due to their contrary helical geometry. Balancing the left-handed with the right-handed torques is key to a rotation-resistant cable design.

One example to this is a 40xK7 type cable, depicted in 6.2. A similar approach could be applied, incorporating all components mentioned in 6.2.1.

Cable Storage

The cable will be rolled over a drum in order to perform descending and ascending of the sphere. Unfortunatley, this process may change rotational properties of the cable, i.e. lay length

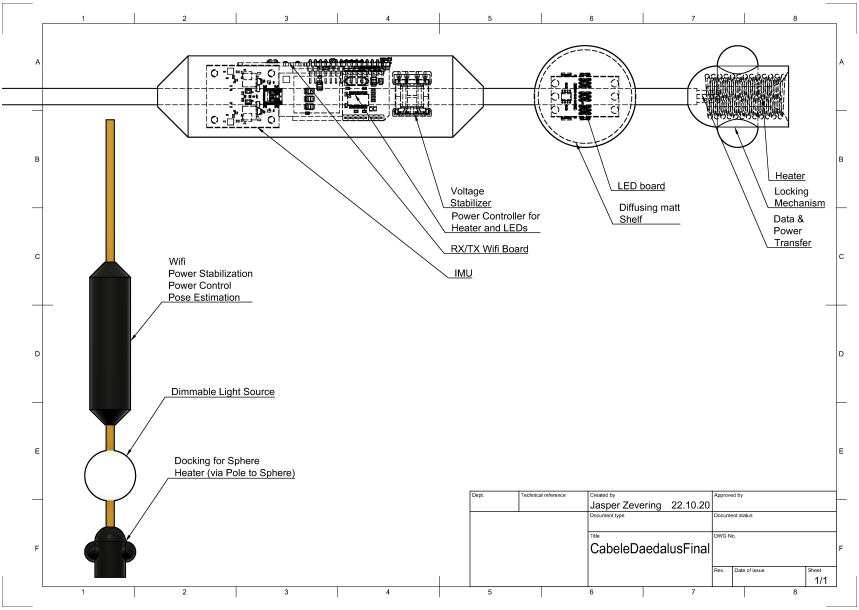

Figure 6.1: The design of the sphere-side end of the cable.

or torque factor, by introducing additional twist to the cable. Therefore, the rotational behavior of the load differs with every transport. To minimize this effect the change of cable properties must be reduced. This is achieved by designing the drum with a large diameter, hence keeping the gradient angle of the drum α and fleet angle between the cable and the lead sheave β (ref. 6.3) as small as possible, which leads to less twist introduced to the cable. Furthermore, the cable should be attached to a swivel. The swivel further helps reducing load rotation by absorbing any outer moments, e.g. established by the drum during conveyance.

6.3 Spherical Robot

6.3.1 Sphere Design

The overall design consists of two main structures, the inner and the outer. Two electrical motors connect them for rotation, and a slip ring for data and power transfer mainly to the cable, which plugs to the outer structure. The inner structure consists of the scanning and

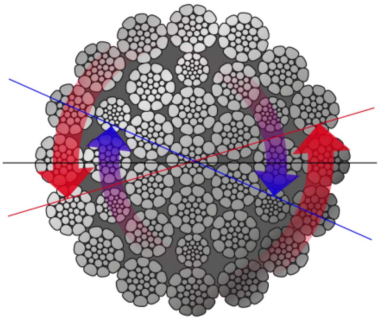

Figure 6.2: A 40xK7 type cable designed for restricting load rotation by countering torques. The inner strands (blue) have opposing lay direction to the outer strands (red).

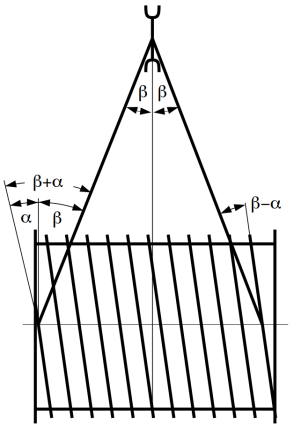

Figure 6.3: A cable rolled around a drum. Gradient angle of the drum α and fleet angle between the cable and the lead sheave β are depicted.

controlling components. More precisely, it consists of two Livox Mid 100 laser scanner, four optical sensors with hemispheric lenses, two micro controllers, two switches, one heater, one battery, which can be folded towards the middle in both directions (see section 6.4.4). The battery leads (in idle position) to a center of mass that is not in the inner structure center. The outer structure holds mainly the pole mechanism, a kind of light source, and the shelf itself.

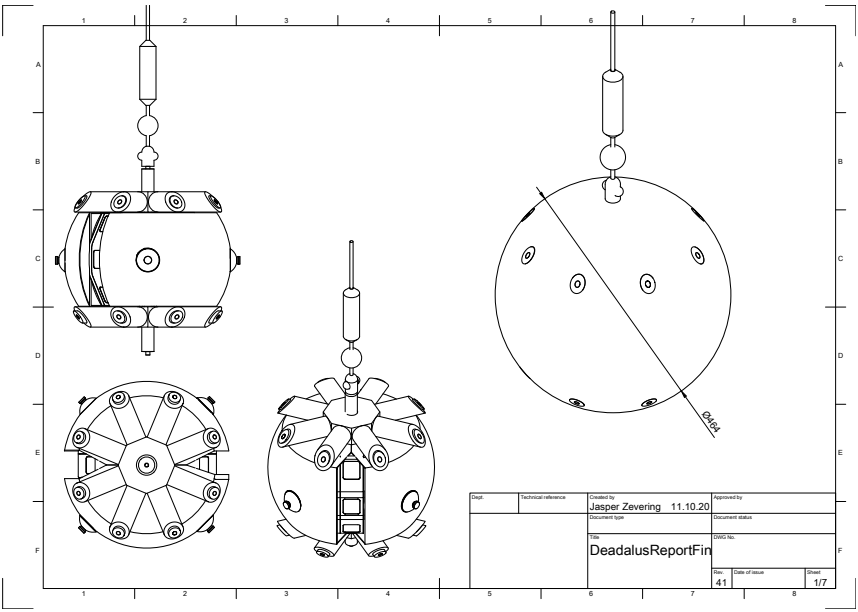

Figure 6.4: Overall sphere design. The CAD shows the sphere with cover.

One of the outer poles is used as a physical, electrical, and data connection to the cable. Due to the motors, the inner and outer structures can rotate relative to each other.

The poles are mounted in a star-shaped form and not a continuous form, as this gives the LIDAR and optical system at nearly half of all possible angles between inner and outer structure a larger side of view. Figures 6.7 and 6.8 show the coverage of the LIDAR scanner in best and worst case positions of inner and outer structure to each other and figures 6.9 and 6.10 the same for the optical system.

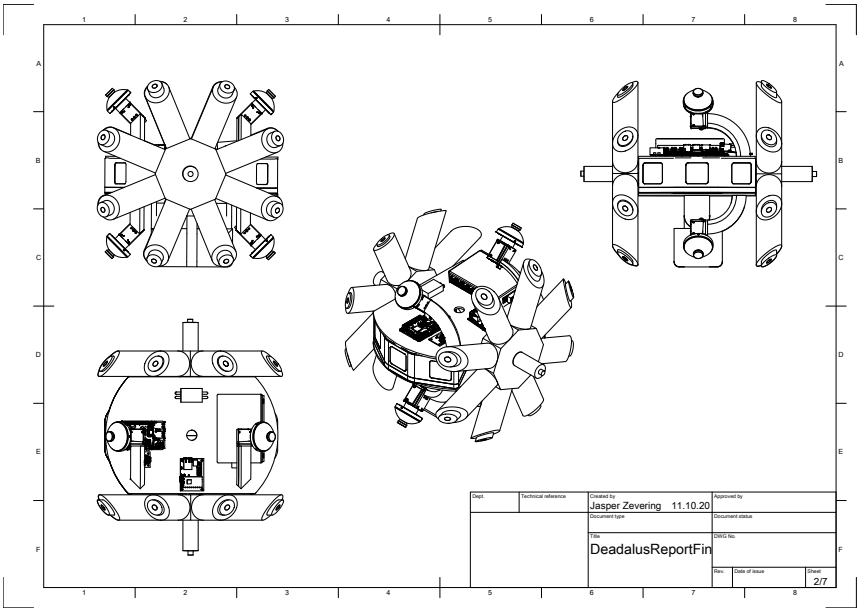

Figure 6.5: Overall sphere design (cont.). THE CAD without cover is shown.

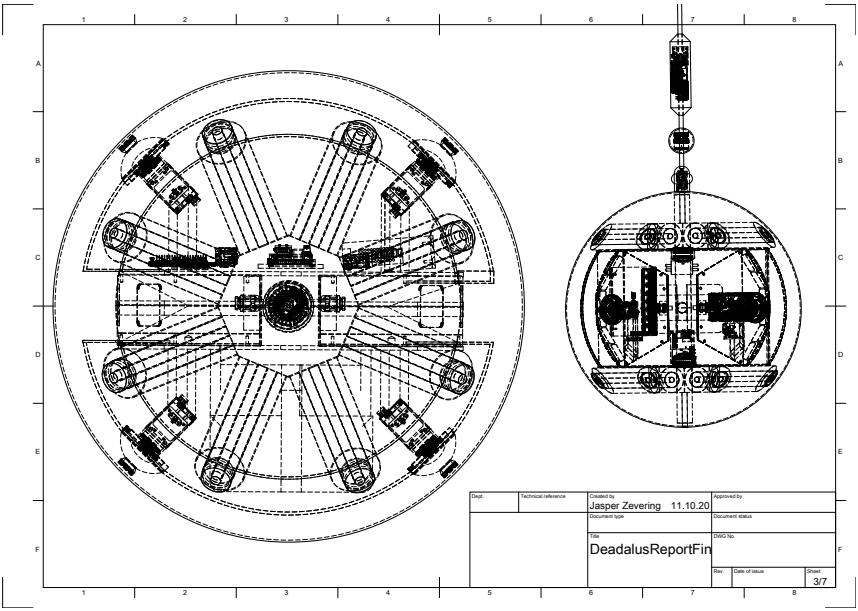

Figure 6.6: Side view while rolling on ground (left) and descending (right).

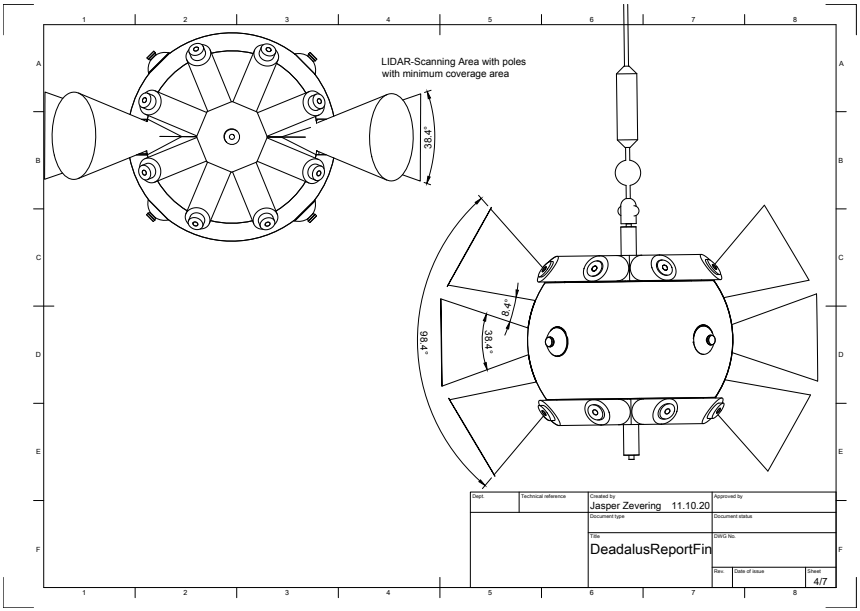

Figure 6.7: Coverage of the LIDAR with the poles in best case position.

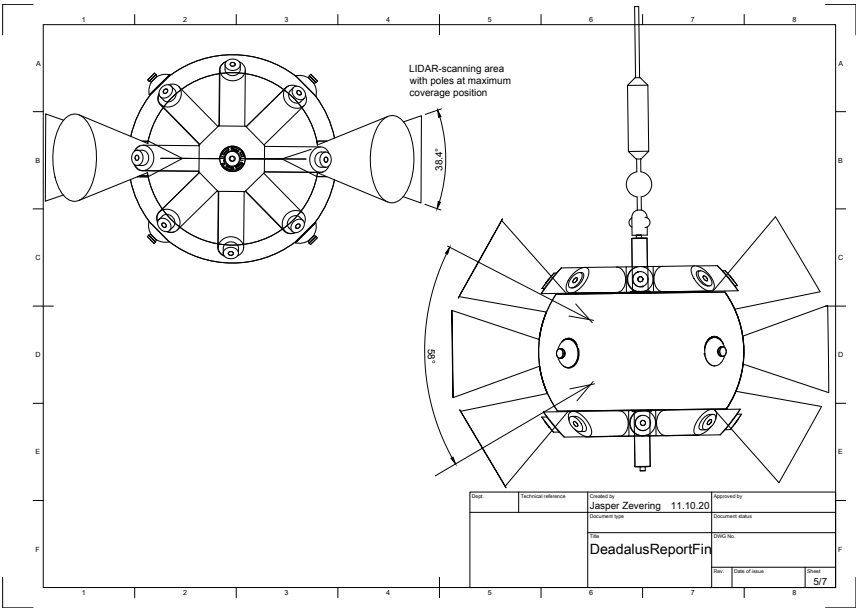

Figure 6.8: Coverage of the LIDAR with the poles in worst case position.

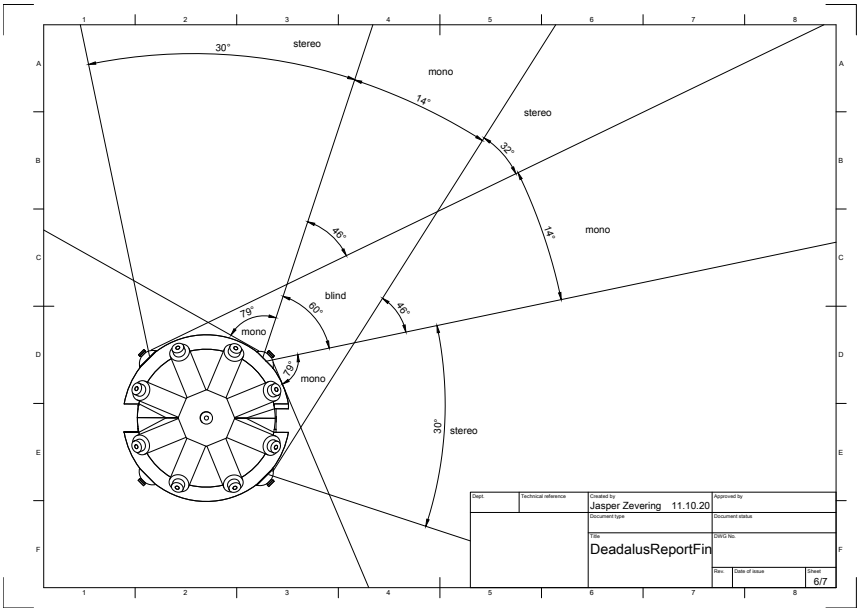

Figure 6.9: Coverage of cameras with hemispherical lenses without linear arm and therefore having blindspots.

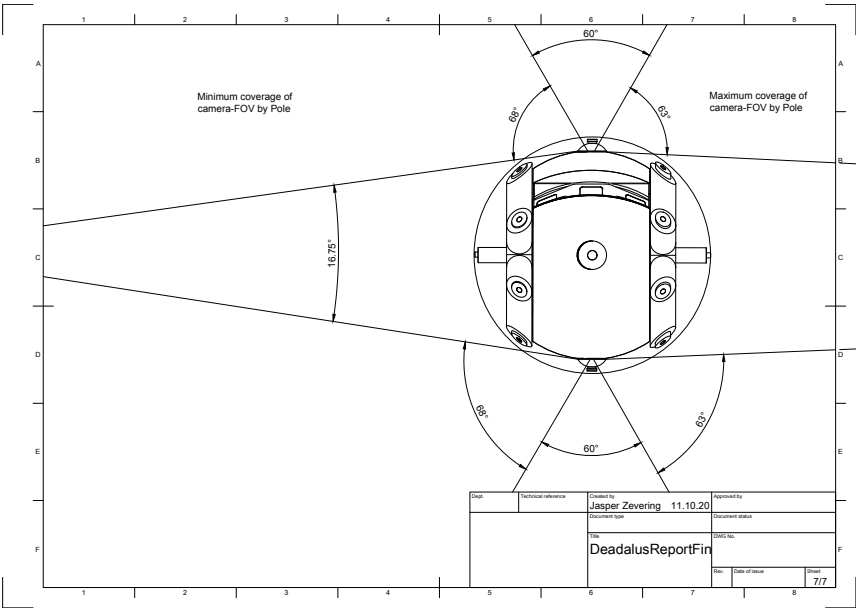

Figure 6.10: Coverage of cameras (cont.)

6.3.2 Power

The Input voltage of all components lies between 5 and 16 Volts. As most of the components have a working voltage range, two groups of 5 and 14 Volts can be formed. Therefore the overall Voltage is 14V, and there will be a voltage converter from 14 to 5 Volts. There is a voltage stabilizer at the sphere side of the cable, as the differing power consumption leads to different voltage drop over the cable. The voltage drop over the cable is shown in table 6.1.

Available voltage stabilizers for 14 V have an input range to up to 50 Volts, so every absolute difference of voltage drop under 40 Volts is suitable. Voltage stabilizers for 14 V start at about 8 V input voltage. This means, depending on the configuration of conductor cross-section and cable length, different voltage inputs at the winch side of the cable are possible. Table 6.2 shows the possible input voltage ranges at the winch side of the cable, for an 8 V to 58 V stabilizer at the sphere side of the cable.

The battery is currently dimensioned 70 mm×160 mm×95 mm. This leads with a Lithium–thionyl chloride battery (ca. 700 mWh/cm^3) to a possible capacity of 744 Wh. This will last for approximately 2hours when detached from the cable and on exploration trip.

Table 6.1: Voltage drop in relation to cable length and the crossection of the conductor.

Minimum to maximum voltage drop
A: conductor cross-section, B: Length of cable

A \ B	40 m	80 m	150 m	300 m
0.75 mm^2	8.3-41.5 V	16.5-83.0 V	31.0-155.6 V	62.0-311.2 V
1.5 mm^2	4.1-20.7 V	8.3-41.5 V	15.5-77.8 V	31.0-155.6 V
2.5 mm^2	2.5-12.4 V	5.0-24.9 V	9.3-46.7 V	18.6-93.4 V
4 mm^2	1.6-7.8 V	3.1-15.6 V	5.8-29.2 V	11.6-58.4 V

Difference between minimum and maximum voltage drop
A: conductor cross-section, B: Length of cable

A \ B	40 m	80 m	150 m	300 m
0.75 mm^2	33.2 V	66.4 V	124.6 V	249.2 V
1.5 mm^2	16.6 V	33.2 V	62.3 V	124.6 V
2.5 mm^2	10.0 V	19.9 V	37.4 V	74.8 V
4 mm^2	6.2 V	12.5 V	23.4 V	46.7 V

Table 6.2: Possible input voltage at the winch-side of the cable for a 8 V to 58 V stabilizer.

A: conductor cross-section, B: Length of cable

A \ B	40 m	80 m	150 m	300 m
0.75 mm^2	16.3-79.5 V			
1.5 mm^2	12.1-58.7 V	16.3-79.5 V		
2.5 mm^2	10.5-50.4 V	13.0-62.9 V	17.3-84.7 V	
4 mm^2	9.6-45.8 V	11.1-53.6 V	13.8-67.2 V	19.6-96.4 V

6.3.3 Computational Power

Computational power depends on three main factors: The stereo mapping of the ground beneath the sphere while descending (see 6.4.3), the SLAM during exploration phases (see 6.4.2), and the data transfer and housekeeping of all data. The ground mapping is a simple stereo image analysis for evaluating the ground. Therefore it has not to be a real-time building of a 3d model, but just the surface estimation. The concept is shown in figure 6.16. With the expected field of view, the ground needs to be 3.4 times the sphere diameter away, for the current design 160cm, to evaluate the ground under the sphere, which covers the diameter of the sphere. This happens as a stereo evaluation of the optical sensors. Supposing the sensors to have 15 MP and the area of interest being 0.04% of the overall sensor coverage, two images of 0.6MP need to be evaluated. The higher the sphere is, the bigger the stereo covered area is on the ground, but the pixel density reduces. Therefore 0.6MP is the worst case and will be used for the computational power calculation. To have this evaluated in 10 seconds, 75MHz processing power is enough. As the data-rate is expected to be at about 30 Mbit/s (see 6.5.2), an efficient handling mechanism will have about 100 instructions per byte that need to be processed for checking, acknowledging, and forwarding to the cable end, and therefore 37MHz is continuously used. Of course, this is an average value, and there will be peaks during scanning, but this is not a time-critical action, as the data is time-stamped and the upload duration does not play a significant role in the data. For the SLAM evaluation 120MHz are considered. As SLAM and stereo evaluation do not need to run parallel, the maximum of them is considered. Therefore 157MHz is considered as the absolute minimum of CPU usage. As the heater and motors dominate the power consumption (see section 6.3.2), the main limiting factor is the price and availability of space-suitable CPUs.

6.3.4 Thermal Management

As mention in section 2.3 we expect the temperatures to vary over a large spectrum (100 K to 360 K). Therefore managing the robot's internal temperature is paramount to keeping the components functional. Given the large temperature range, cooling as well as heating is required to keep the robot in its operating range. The following investigates multiple approaches for both processes.

Cooling

Passive Radiation Passive radiation is used to cool the sphere by increasing the surface area of the robot over which heat can be discharged. Outside the field of view of the cameras and the lidar of the sphere the shell is not required to be transparent. Hence, by fabricating this area with a material with high emmissivity a constant discharge of heat could be installed. However, since there is no possibility to control this heat discharge, it could adversely affect the temperature in a negative way, discharging heat even when the sphere needed to be heated.

The rods used for locomotion and during the scanning mode provide a controllable way of increasing the radiating area's size. By designing the rods in a "star" form the surface area can be further increased (cf. figure 6.12). Given that the rods can be regulated to all states between not extended and fully extended, this grants a high degree of controllability.

Assuming the rods are coated in a material of which we can assume the emissivity to be safely above 0.9 (such as Ball infrared Black [56]) the sphere could disperse heat at temperatures as shown in figure 6.11 given the surface shown in figure 6.12.

In addition, the cable used for descend provides an opportunity for heat discharge. During descend, the sphere directs the excess heat generated by the sphere's components to the cable. The exterior of the cable is then coated with a highly emissive material, thus discharging the heat via radiation.

Selective Component Activation Each component in the sphere generates a substantial amount of excess heat. To stay within operating temperature range this heat needs to be discharged. However, another option to discharging all of the heat is to create less heat by activating less components. In particular, many of the components already provide redundancy and are not required in all operating modes (cf. section 6.4). E.g. during regular navigation a single lidar of the three front facing lidars and none of the back facing lidars need to be active. Similarly the cameras only need to be active during the scanning mode. Deactivating the appropriate devices significantly lowers the burden on the cooling system.

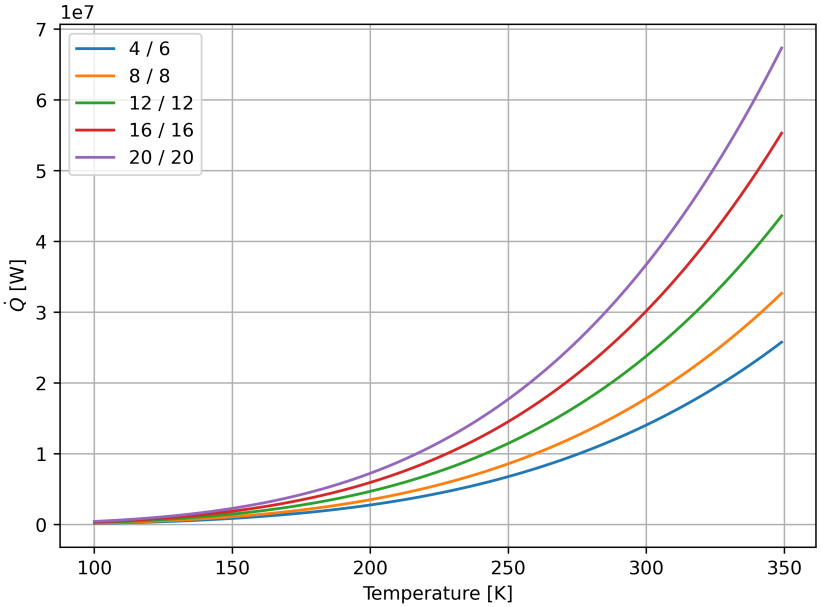

Figure 6.11: Dispersed heat for selected fin configurations at different temperatures. The configurations are given as NumOf-inner Fins/NumOf-outer Fins.

Heating

As mentioned before, all components of the sphere generate heat. This provides a baseline for heating the sphere in a cold environment by activating all components. It is to be expected that the heat generated by the components does not suffice to keep the sphere at operating temperature. Therefore an active heating system needs to be employed.

During descend the energy supply for the active heating system does not pose any challenges as the energy supply via the cable is guaranteed. Additionally, when attached to the cable there exists a strong thermal coupling between the cable and the robot as a solid metal rod connects the two, hence making it easy to heat the sphere using the cable. During exploration and scanning on the ground however, this system would be fueled by the battery. Therefore a possible approach is:

1. Before detachment, heat the sphere using the energy supply of the cable.

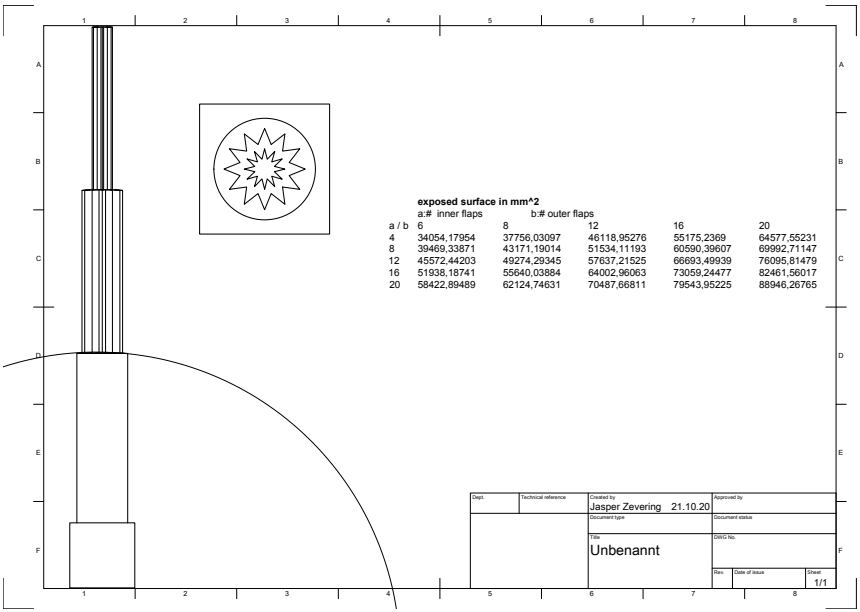

Figure 6.12: A fin design for the locomotion rods of the sphere. The star design is chosen in order to avoid dust agglomerate inside the fins. The table shows different realizable surface sizes given the number of fins.

2. Detach and start exploration cycle

3. During exploration maintain heat via battery energy

4. Return to cable before critical temperature or battery state is reached

The return to the cable is a necessity even without the thermal control component as the battery only provides energy for a limited amount of time, making this approach feasible.

As a first approach to find the magnitude of heating required we model the interior components as mainly aluminum and the exterior as glass. Hence the specific heat capacity is assumed to be the one of aluminum and the emissivity of glass. Simulating this system with all components but the motor active, and a reactive heater that keeps the system within the operating range once the bounds are reached yields temperature curve in figure 6.13. Table 6.3 displays the heating requirements for different time windows and temperatures.

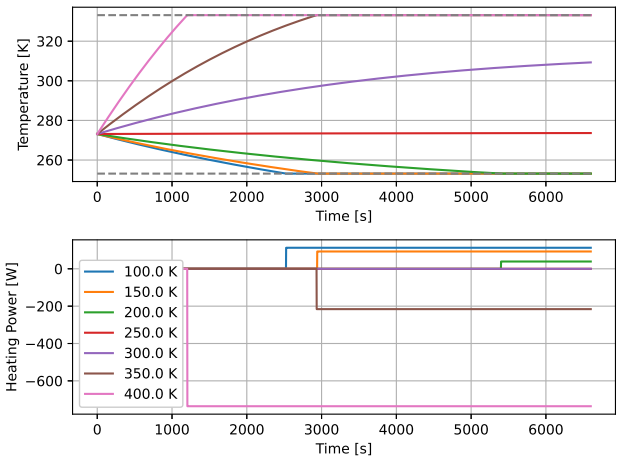

Figure 6.13: Simulated temperature curves for different environment temperatures.

Table 6.3: Energy Required to keep the robot within operating temperature for a set amount of time given the environment temperature. It is assumed that the robot is at central operating (273.15 K) temperature when the time frame starts. Negative Energy implies that this energy needs to be dispersed using the radiators. The simulation can be found in appendix A.

Time \ Temp	100 K	150 K	200 K	250 K	300 K	350 K
10.0 min	0.00 Wh	0.00 Wh	0.00 Wh	0.00 Wh	0.00 Wh	0.00 Wh
20.0 min	0.00 Wh	0.00 Wh	0.00 Wh	0.00 Wh	0.00 Wh	0.00 Wh
30.0 min	0.00 Wh	0.00 Wh	0.00 Wh	0.00 Wh	0.00 Wh	0.00 Wh
40.0 min	0.00 Wh	0.00 Wh	0.00 Wh	0.00 Wh	0.00 Wh	0.00 Wh
50.0 min	14.90 Wh	1.54 Wh	0.00 Wh	0.00 Wh	0.00 Wh	-4.04 Wh
60.0 min	33.67 Wh	17.00 Wh	0.00 Wh	0.00 Wh	0.00 Wh	-40.02 Wh
70.0 min	52.45 Wh	32.45 Wh	0.00 Wh	0.00 Wh	0.00 Wh	-76.01 Wh
80.0 min	71.23 Wh	47.91 Wh	0.00 Wh	0.00 Wh	0.00 Wh	-111.99 Wh
90.0 min	90.01 Wh	63.36 Wh	0.02 Wh	0.00 Wh	0.00 Wh	-147.97 Wh
100.0 min	108.78 Wh	78.82 Wh	6.53 Wh	0.00 Wh	0.00 Wh	-183.96 Wh
110.0 min	127.56 Wh	94.27 Wh	13.03 Wh	0.00 Wh	0.00 Wh	-219.94 Wh
120.0 min	146.34 Wh	109.72 Wh	19.54 Wh	0.00 Wh	0.00 Wh	-255.93 Wh

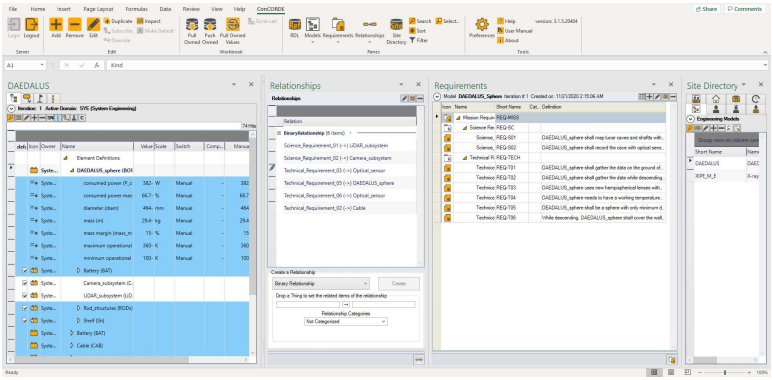

Figure 6.14: Screenshot of the current model in ConCORDE

6.3.5 Datasheet

Table 6.4 preents the data sheet of DAEDALUS and Fig. 6.14 shows a screenshot in OCDT of the current model in ConCORDE.

Table 6.4: Datasheet of current design.

Datasheet of current Design		
Parameter	Value	related
Diameter	464 mm	fig. 6.4; Fig. 6.5
Cable Length	80 m	2.5; Sec. 6.6.3
Power Consumption	127 W–637 W	Sec. 6.5.1
Voltage range of supply	12 V–79 V	Tab. 6.2
Voltage Input of Sphere	14 V	6.3.2
Battery Capacity	744 Wh	Sec. 6.3.2; Sec. 6.6.7
Mass (sphere)	20 kg–30 kg	Sec. 6.5.3
Mass (cable)	12 kg	Sec. 6.5.3
Operating Range (Temperature)	100 K–330 K	Req-T03; Sec. 6.3.4
Minimum CPU	157 MHz	Sec. 6.3.3

6.4 Stages, Phases, Modes and Procedures

In the following chapter the Stages (STG), Mission Phases (MP), Operating Modes (OM) and Procedures (PRC) will be explained. The stages refer to the overall cave-exploration mission, of which the sphere is a part. The stages include every part of the mission from finding the shafts to clean up the mission. Mission Phases divide the overall mission into different parts which differ in their time and scientific interest. So all Phases have different goals regarding whats scanned, independently of which components are used. Operating Modes are the different states the sphere can be in, regarding the technical aspects. This correlates in some parts to the phases, but is independent on what is scanned, it just relies on technical aspects. Procedures cover specialized, non trivial courses of action, and describe the pure technical sequence of events for certain actions.

6.4.1 Stages II + III

The presented sphere is part of the STG II and STG III of ESAs defintion of mission stages. The second stage is the deployment of the probe into the pit, making measurements of the pit walls as it descends. The thrid stage iste the exploration of the pit floor, find a way to access the lava tube and perform science experiments within the cave to find out more.

6.4.2 Mission Phases

The Mission Phases divide the stages into logically and chronologically connected parts of the mission. They deal with only the sphere robot and its deployment, whereas the stages separate the whole overall mission.

Phase I: Descender deployment

The first phase does not include actual mapping but estimation of the exact deployment place of the sphere. Therefore it needs to be lift out of any transportation mechanism and placed above the descending spot. The descending route will be checked by the visual sensors for first obstacles.

Phase II: Shaft mapping

The sphere starts descending. The shaft is scanned with LIDAR and captured fully stereo of the optical system. This directly meets Req-T02. Req-S01 and Req-S02 will be satisfied in this phase.

Phase III: Fixed, elevated cave mapping

The sphere enters the main void. It descends to half the path of void to bottom and scans the cave from that position. This will give en elevated overview of the cave. It is likely to not fulfill Req-S01 and Req-S02, due to the unknown depth of the cave. Therefore the resolution can not be guaranteed from only that position.

Phase IV floor-bound exploration

The sphere will move through the cave and gather data fulfilling Req-T02. Req-S01 and Req-S02 will be satisfied in this phase. It will move away in exploration missions which will have a increasing range and therefore increasing risk. The next exploration trip will be only started if the data of the one before is uploaded successfully.

6.4.3 Operating Modes

Mode 1 : Descending Mode

In the descending mode, the sphere is connected to the cable by one of the outer poles. Both poles are suitable for the connection for redundancy reasons. The powering of the sphere is done

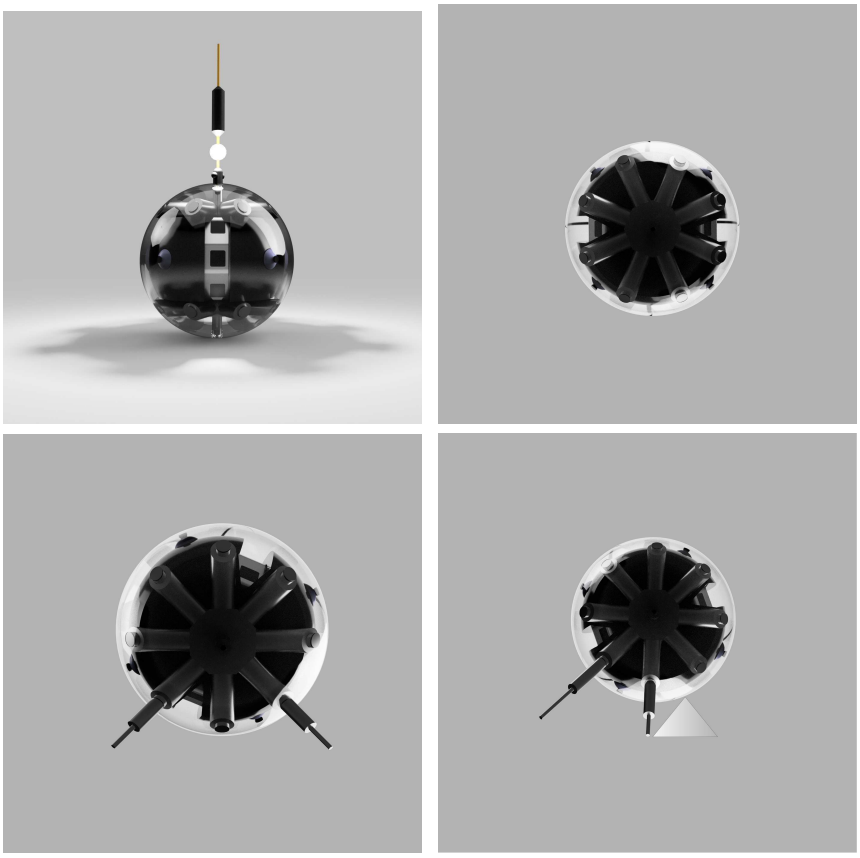

Figure 6.15: The different modes of the Sphere. Top-Left: Mode 1, Desending Mode. Top-Right: Mode 2, Rolling Mode. Bottom-Left Mode 3, Scanning Mode. Bottom-Right: Mode 4, Obstacle Mode.

by the external power over the cable or a combination of it with the own Battery (see 6.5.1). In this mode, the sphere is lowered by the crane into the cave. The inner structure rotates to guarantee full coverage by LIDAR and full stereo coverage by the optical sensors. Full optical mono coverage of the current plane is given at any time (see fig 6.9). The inner structure's rotation will lead to a twist of the cable in the opposite direction if performed too fast. If a twist happens, the motor should stop, and the outer structure will rotate back and eventually over swing till it has the original orientation. This is not a problem, as the source of motion (cable twist or motor rotation) does not influence the scanning result as long as it is full 360 degrees. Without any redundancy, a rotation of 152 degrees at one specific scanning plane is enough to have full LIDAR and optical coverage, as there are two LIDAR scanners with a sideways range of 38.4 degrees. The light source of the cable lights the shaft while descending. The Battery will be at its maximum angle to keep the center of mass in the middle of the sphere as good as possible. This will prevent the sphere from hanging askew. During descending, the ground structure's nature will be evaluated by the overlapping parts of all four cameras, which exists at a certain distance. The closer the sphere gets to the ground, the less stereo coverage of the landing position under the sphere can be evaluated, resulting in only mono coverage and blind spots. When too close to the ground, the sphere can not evaluate the surface exactly under it. However, as the surface is not expected to change, the evaluation from a distance will be enough to get a rough characterization of the surface to expect. This concept is shown in figure 6.16. The scanning of MP III is done in this mode, too, as it is technically seen not different from MP II.

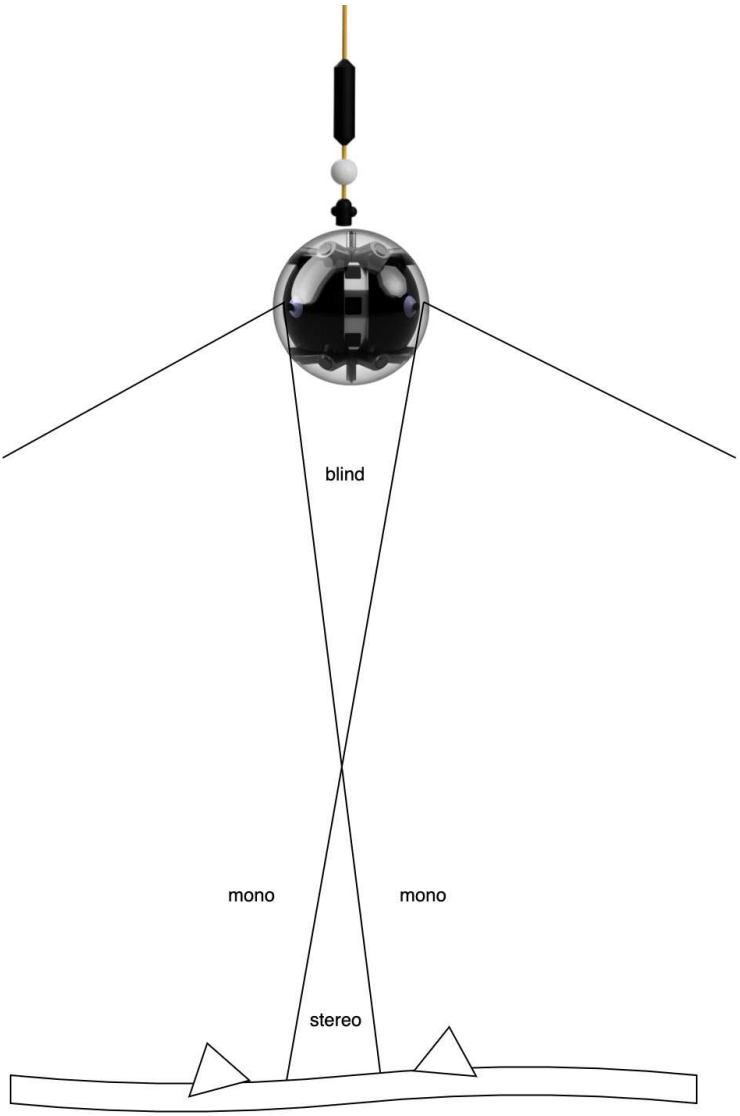

Figure 6.16: Stereo and mono optical coverage of the ground while descending at a certain distance.

Table 6.5: Possible maximum obstacle heights, relative to sphere diameter for different relative positions of the mass center where 0 correspondents to the sphere midpoint and 1 to the shelf. As it is impossible to have the mass center in the shelf itself, if there is any electronic inside the sphere, 0.99 is the maximum calculated value.

A: Relatively position of the mass center between midpoint (= 0) and shelf (= 1)
B:Maximum height of obstacle relative to sphere diameter

A	0.990	0.800	0.600	0.400	0.200	0
B	0.429	0.200	0.100	0. 042	0.010	0
Margins	0.387 - 0.472	0.180 - 0.220	0.090 - 0.110	0.038 - 0.046	0,009 - 0,011	0

Mode 2 : Rolling Mode

The rolling mode is one of the two possibilities for locomotion. The second one is described in 6.4.3. Due to the low center of mass of the inner structure, caused by the low hanging battery, using the motors will lead to a rotation of the outer structure. This again leads to locomotion of the overall sphere. In the direction of movement, the LIDAR scans forward and backward. The width of the scanning field changes periodically, as poles enter and leave the field, according to figure 6.7. The optical system has full mono and partially stereo coverage, according to figure 6.9. Changing the mass distribution to the left or right direction is changed (see 6.4.4). Depending on how low the center of mass is, the mass distribution itself, and the diameter, the sphere can roll over small obstacles. For bigger obstacles, the sphere hast to go to mode 4 (see 6.4.3). Important for overcoming obstacles is the center of mass of the outer and inner structure together. As the inner structure has an unsymmetrical mass distribution with the center of mass lies outside the center of the midpoint, which makes the rolling possible in the first place, the outer structure is supposed to have a symmetrical weight distribution with the center of mass being the center of the sphere. Therefore, the center of both structures together is also quite near the center, depending on the inner and outer structures' overall weight. For the current design, the mass center is expected to lie at around 15% of the sphere radius, so 34,8mm away from the midpoint. Table 6.5 shows for different mass centers the maximum capable obstacle size for this mode, relatively to the sphere, table 6.6 shows them for the 464mm sphere.

Mode 3 : Scanning Mode

This mode compensates for the limited coverage of the LIDAR and the partly stereo coverage of the optical system during mode 1. Four poles extend to touch the ground, stabilizing the sphere. With this configuration, activating the motors will no longer lead to a rotation of the outer Structure but of the inner, as the outer cannot roll because of the poles. Rotating the inner

Table 6.6: Possible maximum obstacle heights for different distances of the mass center from the midpoint, calculated for the 464 mm diameter sphere.

A: Distance of the mass center from the midpoint
B: Maximum height of obstacle

A in mm	229.680	185.600	139.200	92.800	46.400	0
B in mm	99.636	46.400	23.200	9.684	2.344	0
Margins	89.673 - 109.600	41.760 - 51.040	20.880 - 25.520	8.716 - 10.653	2.109 - 2.578	0

Structure leads to the maximum possible scanning area. The optical system will cover the whole visible area from the point of the sphere. Due to its scanning width of 98,4 degrees, the LIDAR misses the part of the cave in the two side poles' directions. Despite the changing scanning width between 98,4 degrees and 58 degrees, the other poles themselves lead to no shortcoming, as the laser scanner is a 3D scanner and not 2D. Therefore the moments before the pole is in the field of view and afterward cover the parts, which would be lost with only a 2D scanner. For complete coverage, the sphere needs to yaw at least 81,6 degrees, better 90 degrees to have overlapping parts with the other scanning section, and perform a second complete scan in this mode.

Mode 4 : Obstacle Mode

If obstacles are to big for mode 2 (see table 6.6), the poles are used to push the sphere over the obstacles. As there is not only one row of poles, but two pole-stars left and right from the center of mass, this happens in a stable manner. Theoretical the sphere can push itself direct 90 degrees upwards, as the inner structure can be slightly rotated, that the center of mass is between the pole and the perpendicular obstacle. This principle is shown in figure 6.17. Table 6.7 shows the maximum size for obstacles in relation to the number of possible extensions of one rod. One extension stands for one solid pole. The current design holds poles with two extensions. As the obstacle will not be rectangular nor have another plan-able form, the obstacles' heights are considered only theoretically maximum possible. The realistic possible heights and restrictions need to be found out with a prototype.

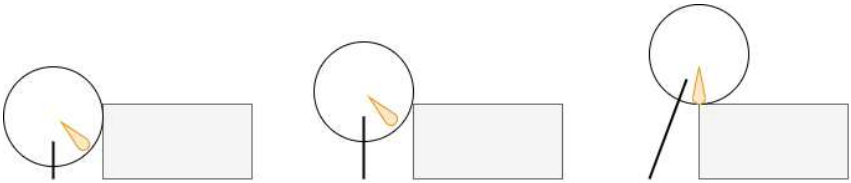

Figure 6.17: Basic concept of overcoming perpendicular obstacles. The orange parts symbolize the battery and therefore the direction of the center of mass.

Table 6.7: Maximum possible rectangular obstacle size for 464mm sphere and relative to sphere diameter, in relation to possible extensions of one pole.

A: number of possible extensions for one pole
B: maximum possible rectangular obstacle height for a 464mm sphere
C: maximum possible rectangular obstacle height relative to sphere diameter

A	1	2	3	4
B in mm	72,00	173,00	277,33	382,50
C	15,52%	37,28%	59,77%	82,44%
Margins in mm	64.80 - 79.20	155.70 - 190.30	249.60 - 305.07	344.25 - 420.75

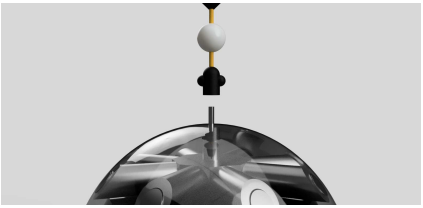

Figure 6.18: Decoupling of the sphere from the cable. One of the poles of the side is used for transfer of data data and power, and for the physical connection.

6.4.4 Procedures

Procedure 1: Decoupling

The decoupling process, cf. Fig. 6.18, takes place after descending and after reloading phases. For safety reasons, while descending, the connection will be mechanical so that power loss does not lead to letting fall the sphere. When the sphere is connected to the cable, connected data transfer and the sphere's power connection are provided through the cable. Therefore the wifi connection between sphere and cable needs to be established before decoupling. Also, the power source needs to be switched to the battery and the success of that confirmed. As the sphere lies sideways on the ground, all poles can be extended as test. Confirmation of successfully extension can happen additionally to the internal sensors, by the optical sensors, simultaneous testing them. If one of these steps fail, decoupling should be prohibited, as a functioning power supply of the sphere and communication are essential for recoupling. If one of two fails, the hardware connection over the cable can again take over. After the disconnection of data and power, the mechanism can release the side pole of the sphere, giving it free. The sphere can pull in that side pole.

Procedure 2: Overturn for Transfer Mode 1 to Mode 2

For mode 2 the sphere needs to be orientated, that the laser scanners are parallel to the ground, cf. Fig. 6.19. This is a turn over of 90 degrees in relation to mode 1. During descending, the battery is near the center of the sphere. For the overturn, it is rotated back to the middle position. Therefore the center of mass is towards on side. This should lead to a turn over by itself. If it turns not over just because of that,e.g. because of an obstacle in the roll direction, the side pole can be extended to help turn over.

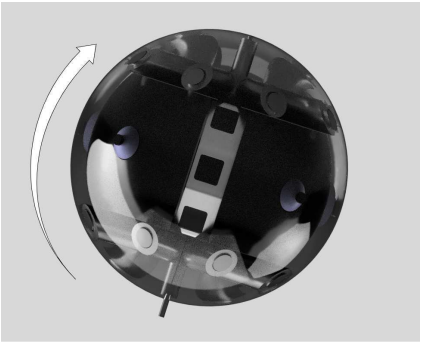

Figure 6.19: To get from descending mode to rolling mode, the sphere need to be turned over. This happen due to the weigth distribution and the help of a sides pole.

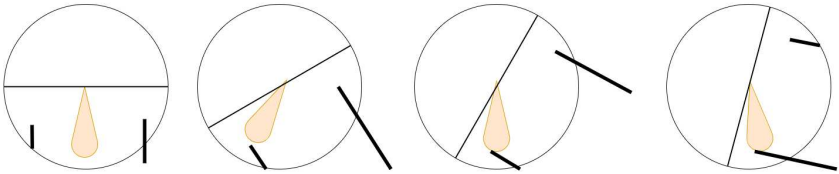

Figure 6.20: Basic concept turn over for recoupling. The orange parts symbolize the battery and therefore the direction of the center of mass.

Procedure 3: Recoupling

For recoupling after expedition trips or pulling the sphere out of the cave, the cable needs to attach to one of the side poles. This can happen either by turning the sphere with the side pole up or by implementing a mechanism into the cable for sideways attachment. The first approach is highly dependable on the possible change o weight distribution by rotating the battery so that the sphere reaches a tilt, that the poles near the ground reach the other side of the sphere, so that extension leads to further tilt and stabilization. This is shown in figure 6.20. The second approach is to avoid turnover and couple sideways. If the connection is just for recharging and data transfer, no further step is required. If the coupling is for pulling the sphere out of the cave, the cable's mechanism will automatically lead to the needed tilt when pulled up. Figure 6.21 shows a possible mechanism for the cable.

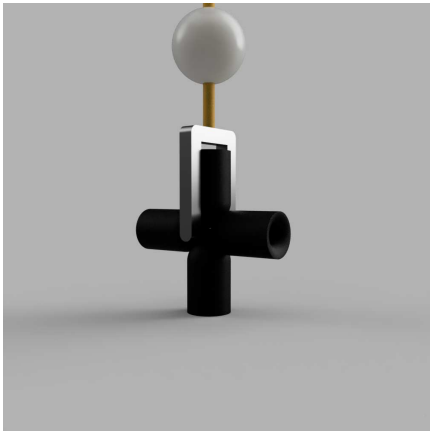

Figure 6.21: Basic concept of wire-mechanism for recoupling, that does not require the sphere to turn over.

Figure 6.22: Changing the weight distribution by changing the pose of the battery laeds to a curved path.

Procedure 4: Changing Weigth Distribution

An actuator connects the battery to the inner structure. It can be rotated to both sides. The battery is supposed o have a significant mass in relation to all other components to control the center of mass in a significant way when rotating. This is used for different purposes. When the battery is in the middle position, the low center of mass enables the rolling mode. Otherwise,

the inner structure and the outer structure would rotate and would not provide controllable movement. Also, the LIDAR could not be used for navigation. During rolling mode, the center of mass displacement leads to a tilt of the whole sphere while the rotation plane stays the same. Therefore the sphere will roll in the direction of the center of mass. this is shown in figure 6.22. While Descending, the battery needs to rotate entirely towards the center of the sphere, as the overall sphere would not be aligned with the cable and tilted a little bit. The same goes for scanning mode, where the center position of the battery would mean much stress for the motors because they circle the center of mass around the sphere's midpoint, as the outer structure can not rotate due to the poles. Therefore only the inner structure can rotate. For obstacle mode, figure 6.17 shows the displacement of the center of mass to the front, to not fall backward. This happens by a small rotation of the inner structure and not by the battery's actuator.

6.4.5 Components during Modes and Procedures

O: Deactivated/Not needed/IDLE; I: Activated; N: as needed/depends on other factors

	LIDAR	Optical Sensors	Side Pole A	Side Pole B	Specific Main Poles	All Main Poles	Rotation Motor	Wired Data Connection	Wireless Data Connection	Sphere Powered by Battery	Charging Battery	Battery Position *	Locking Mechanism of Cable	Winch/Crane
Mode 1	I	I	I	O	O	N**	I	I	O	N	I	I	I	I
Charging after Mode 1	O	O	I	O	O	N**	O	I	O	O	I	I	I	O
Procedure 1 #1	I	I	I	O	O	I	I	I	I	I	I	I	I	O
Procedure 1 #2	I	O	I	O	O	O	O	O	I	I	O	I	I	O
Procedure 2	I	O	O	N	O	O	O	O	I	I	O	O	O	O
Mode 2	I	N	O	O	O	O	I	O	I	I	O	N	O	O
Mode 3	I	I	O	O	I	O	I	O	I	I	O	I	O	O
Mode 4	I	I	O	O	I	O	N	O	I	I	O	O	O	O
Procedure 4 #1	I	O	O	O	I	O	O	O	I	I	O	I	O	N
Procedure 4 #2	I	O	I	O	I	O	O	O	I	I	O	I	I	N
Procedure 4 #3	O	O	I	O	O	O	O	I	I	I	I	I	I	O
Procedure 4 #4	O	O	I	O	O	N**	O	I	O	N	I	I	I	O

* O:middle position, I: rotated completly to one side, N: rotated as needed

** for cooling

6.5 External Interfaces

6.5.1 External Power

Depending on the possible provided power, two general approaches for the interface for power are possible. The minimal approach loads the battery while also powering the minimal life-supporting system of heating/cooling and controllers. Therefore scanning activities are powered over the battery. Although this limits the possible scanning duration and prevents continuous scanning, the required energy provided could be reduced to a minimum. This would mean that the sphere starts fully charged with mode 1 (see 6.4.3), and the scanning activities have to be stopped once the ground to charge the battery again. Depending on the length of the route to be covered and the size of the battery selected, it may also be necessary to charge halfway, and therefore pause the descending. With all Scanning devices turned off, the heater in the sphere and cable are the only sources for warming. They are therefore considered running with full power for the minimum power calculation. Also the peak power needs to be considered, as it can not be compensated by the battery, as it will be low at curtain times during mission.. The needed power for this approach made of the current assumptions of heater dimensions etc. is shown in table 6.8

A second approach is a full-power approach. The sphere is powered during mode 1 (see 6.4.3) fully by the external power source over the cable. This means the external source needs to provide more power. On the other hand, the redundancy is increased, as all battery cells' failure can be compensated, at least during Mode 1 (see 6.4.3). Charging times are also decreased, as more power is available during charging sessions between expeditions trips, as during recharge, no scanning is needed, as it would only be re-scans. This approach is more secure than the minimum power approach, as it can compensate a partial collapse of power providence by switching to

Table 6.8: Table showing the required amount of power for minimal power supply approach

Component	Peak Power per Unit	Number of Units	Total required Power
MicroController (Cable)	5 W	2	10 W
MicroController (Sphere)	5 W	2	10 W
Heating (Cable)	50 W	1	50 W
Heating (Sphere)	50 W	1	50 W
Loss of Volatage Stabilizer	5 W	1	5 W
IMU	0,33 W	3	1 W
battery Charge	>1 W	1	>1 W
		Overall	>127 W

Table 6.9: Table showing the ranges for the required amount of power for minimal power supply approach

Component	Peak Power per Unit	Number of Units	Total required Power
MicroController (Cable)	4 W - 8 W	2	8 W - 16 W
MicroController (Sphere)	4 W - 8 W	2	8 W - 16 W
Heating (Cable)	30 W - 120 W	1	30 W - 120 W
Heating (Sphere)	30 W - 120 W	1	30 W - 120 W
Loss of Volatage Stabilizer	4 W - 6 W	1	4 W - 6 W
IMU	0.25 W - 0.75 W	3	0.75 W - 2.25 W
battery Charge	>1 W	1	>1 W
		Overall	>81 W - 281 W

the minimum power approach. The peak power during starting phase of the LIDAR and other peaking events can be compensated by the battery, if power limitations of the external source would not allow proviadance of the peak power. The needed power for this approach made of the current assumptions of heater dimensions etc. is shown in table 6.10

Table 6.10: Table showing the required amount of power for maximum power supply approach.

Component	Average Power per Unit	Peak Power per Unit	Number of Units	Total required Average Power	Total required Peak Power
MicroController (Cable)	1 W	5 W	2	2 W	10 W
MicroController (Sphere)	1 W	5 W	2	2 W	10 W
Heating (Cable)	30 W	50 W	1	30 W	50 W
Heating (Sphere)	20 W	50 W	1	20 W	50 W
Loss of Volatage Stabilizer	5 W	5 W	1	5 W	5 W
IMU	0.33 W	0.33 W	3	1 W	1 W
Lidar	30 W	60 W	2	60 W	120 W
Optical Sensor	4 W	6 W	4	16 W	24 W
Switch	5 W	6 W	1	5 W	6 W
Motor	100 W	180 W	2	200 W	360 W
battery Charge	>1 W	>1 W	1	>1 W	>1 W
			Overall	>342 W	>637 W

Table 6.11: Table showing the ranges for required amount of power for maximum power supply approach.

Component	Average Power per Unit	Peak Power per Unit	Number of Units	Total required Average Power	Total required Peak Power
MicroController (Cable)	1 W - 4 W	4 W - 8 W	2	2 W - 8 W	8 W - 16 W
MicroController (Sphere)	1 W - 4 W	4 W - 8 W	2	2 W - 8 W	8 W - 16 W
Heating (Cable)	30 W - 60 W	30 W - 120 W	1	30 W - 60 W	30 W - 120 W
Heating (Sphere)	30 W - 60 W	30 W - 120 W	1	30 W - 60 W	30 W - 120 W
Loss of Volatage Stabilizer	2 W - 3 W	4 W - 6 W	1	2 W - 3 W	4 W - 6 W
IMU	0.25 W - 0.75 W	0.25 W - 0.75 W	3	0.75 W - 2.25 W	0.75 W - 2.25 W
Lidar	20 W - 40 W	50 W - 80 W	2	40 W - 80 W	100 W - 160 W
Optical Sensor	3 W - 5 W	5 W - 7 W	4	12 W - 20 W	20 W - 28 W
Switch	4 W - 6 W	5 W - 7 W	1	4 W - 6 W	5 W - 7 W
Motor	80 W - 120 W	160 W - 200 W	2	160 W - 240 W	320 W - 400 W
battery Charge	>1 W	>1 W	1	>1 W	>1 W
			Overall	>283.75 W-488.25 W	>526.75 W - 876.25 W

6.5.2 Data Interface

To meet the requirement Req-T06, 625 (25×25)pixel needs to be provided per square meter. Table 6.12 shows, that 8 MP are sufficient for this requirement. Because Mode 2,3 and 4 (see 6.4.3) are disconnected from the cable, a wifi transmission between the cable end and the sphere is established. But out of redundancy reasons and the possibility of expeditions far away from the cable, there is data storage onboard. Therefore there is no necessity for full instant data transfer. However, data can be gathered in the onboard storage and then transmitted over the cable at the maximum available upload speed. Table 6.13 shows the optical system dominates the maximum data rate. As 17.29 Gbit/s is likely to exhaust or overwhelm existing data transfer structures of the external and internal interfaces, the frame rate needs to be reduced. This could happen without a reduction of coverage because the descend and roll speed can be slowed down as desired. The LIDAR data is not considered to be reduced, as the special scanning pattern (see 3.12 only has full coverage, if all data is continuously recorded for at least 1.5 seconds. A burst-mode like approach with buffering 1.5 seconds and then waiting for the buffer to be uploaded can lower the data rate. However, the data for one picture by one of the four cameras has 288 Mbit, so the majority of data reduction has to be done with the reduction of optical data. The Data Rates of different frame rates are listed in table 6.15.

The overall conclusion for the data interface is that there are multiple ways of reducing data without endangering quality or coverage. However, this goes hand in hand with a considerable slowdown in all processes. Housekeeping Data and IMU data are the only ones that do not reproduce necessarily the same data when staying at one level (considering the sphere to spin around its own axes that need to be tracked by IMU) and, therefore, can not be slowed down. This leads to absolute minimum data, based on the rate of IMU and Housekeeping, of approximately 181Kbit/s. Each additional data rate provided accelerates the entire mission. If not

Table 6.12: Pixel per square meter in relation to shaft diameter and sensor resolution.

optical resolution while descending
A: shaft diamater, B: resolution of sensor

A \ B	8 MP	10 MP	12 MP	14 MP	16 MP
70 m	1034 px/m2	1292 px/m2	1551 px/m2	1809 px/m2	2068 px/m2
80 m	791 px/m2	989 px/m2	1187 px/m2	1385 px/m2	1583 px/m2
90 m	625 px/m2	781 px/m2	938 px/m2	1094 px/m2	1251 px/m2
100 m	506 px/m2	633 px/m2	759 px/m2	886 px/m2	1013 px/m2

Table 6.13: Table showing the maximum data rate of all components

Component	Data Rate per Unit	Number of Units	Total data Rate
Livox Mid-100	4.8 Mbit/s	2	9.6 Mbit/s
Optical Sensor 12 bit 8 MP 15 fps	4.32 Gbit/s	4	17.28 Gbit/s
Imu (Cable and Sphere)	36 Kbit/s	5	180 Kbit/s
Housekeeping Data	1 Kbit/s	1	1 Kbit/s
		Overall	≈ 17.29 Gbit/s

Table 6.14: Table showing estimated data rate margins of all components

Component	Data Rate per Unit	Number of Units	Total data Rate
LIDAR Data-Rate Range	3 Mbit/s - 10 Mbit/s	2	6 Mbit/s - 20 Mbit/s
Optical Sensor 12 Bit 2 MP - 12 MP 15 fps	1 Gbit/s - 6.5 Gbit/s	4	4 Gbit/s - 26 Gbit/s
Imu (Cable and Sphere)	30 Kbit/s - 50 Kbit/s	5	150 Kbit/s - 250 Kbit/s
Housekeeping Data	0.5 Kbit/s - 1 Kbit/s	1	0.5 KBit/s - 1 Kbit/s
		Overall	≈ 4 Gbit/s - 26 Gbit/s

scanned continuously but at certain distances, the following assumptions can be made: for full stereo coverage at one point, 2 pictures of each optical sensor are needed, as we got 360-degree mono coverage but not 360-degree stereo coverage (see figure 6.9). For the LIDAR, one scan gets 38.4-degree coverage. Ten complete scans need to be made for full coverage by each of both Lidars (for redundancy). A complete scan needs 1,5 seconds, and therefore 15 seconds at each desired scanning height/place. So every full scan at one certain point produces 432Mbit (8 times 8MP 12-bit photos with 0.125 factor compression and 15 seconds of 9.6Mbit/s Lidar Scanning). With the assumption of a descending speed of 4m/min, the ratio between overall

Table 6.15: Data rate of optical sensor and alls Components with different frame rates.

Frames rate of optical Sensor	Data Rate for all 4 Sensors together	Data Rate with all other Components
15/s	17.28 Gbit/s	17.29 Gbit/s
5/s	5.76 Gbit/s	5.77 Gbit/s
1/s	1.15 Gbit/s	1.16 Gbit/s
30/min	576.0 Mbit/s	585.8 Mbit/s
1/min	19.2 Mbit/s	29.0 Mbit/s

Table 6.16: Margins for Data rate of optical sensor and all Components with different frame rates.

Frames rate of optical Sensor	Data Rate for all 4 Sensors together	Data Rate with all other Components
15/s	4.32 Gbit/s - 25.92 Gbit/s	4.33 Gbit/s - 25.93 Gbit/s
5/s	1.44 Gbit/s - 8.64 Gbit/s	1.45 Gbit/s - 8.65 Gbit/s
1/s	0.29 Gbit/s - 1.73 Gbit/s	0.30 Gbit/s - 1.74 Gbit/s
30/min	144 Mbit/s - 864 Mbit/s	153.8 Mbit/s - 873.8 Mbit/s
1/min	4.80 Mbit/s - 28.8 Mbit/s	14.60 Mbit/s - 38.6 Mbit/s

Table 6.17: Overall descending time with given step size of scanning. Assuming 4 m/min descend velocity

Step size for scans	Overall duration of descenending process (hh:mm:ss)
1cm	16:50:00
2cm	8:30:00
5cm	3:30:00
10cm	1:50:00
20cm	1:00:00
50cm	0:30:00
100cm	0:20:00

descending time and upload time is shown in table 6.21 for different desired step sizes and data rates. In table 6.17 the absolute descending time and in table 6.19 the absolute upload time is calculated. We assume no movement during scanning and, therefore an alternation between scanning 15 seconds and descending.

Table 6.21 shows the optimum for uploading lies between 20 and 30 Mbit/s, depending on the desired stepsize for scanning.

Table 6.18: Ranges for overall descending time with given step size of scanning. Assuming 2 m/min - 6 m/min descend velocity

Step size for scans	Overall duration of descenending process (hh:mm:ss)
1 cm	17:00:00 - 16:46:40
2 cm	8:40:00 - 8:26:40
5 cm	3:40:00 - 3:26:40
10 cm	2:00:00 - 1:46:40
20 cm	1:10:00 - 0:56:40
50 cm	0:40:00 - 0:26:40
100 cm	0:30:00 - 0:16:40

Table 6.19: Overall upload time with given step size of scanning and upload rate. Assuming 432 Mbit/step as datarate of the imaging data.

Upload rate / Stepsize	0.1 Mbit/s	1 Mbit/s	5 Mbit/s	20 Mbit/s	30 Mbit/s	50 Mbit/s	100 Mbit/s
1cm	4800:00:00	480:00:00	96:00:00	24:00:00	16:00:00	9:36:00	4:48:00
2cm	2400:00:00	240:00:00	48:00:00	12:00:00	8:00:00	4:48:00	2:24:00
5cm	960:00:00	96:00:00	19:12:00	4:48:00	3:12:00	1:55:12	0:57:36
10cm	480:00:00	48:00:00	9:36:00	2:24:00	1:36:00	0:57:36	0:28:48
20cm	240:00:00	24:00:00	4:48:00	1:12:00	0:48:00	0:28:48	0:14:24
50cm	96:00:00	9:36:00	1:55:12	0:28:48	0:19:12	0:11:31	0:05:46
100cm	48:00:00	4:48:00	0:57:36	0:14:24	0:09:36	0:05:46	0:02:53

Table 6.20: Overall upload time with given step size of scanning and upload rate. Assuming a range of 100 Mbit/step - 650 Mbit/step as datarate of the imaging data.

Upload rate / Stepsize	0.1 Mbit/s	1 Mbit/s	5 Mbit/s	20 Mbit/s	30 Mbit/s	50 Mbit/s	100 Mbit/s
1 cm	1111:06:40 - 7222:13:20	111:06:40 - 722:13:20	22:13:20 - 144:26:40	5:33:20 - 36:06:40	3:42:13 - 24:04:27	2:13:20 - 14:26:40	1:06:40 - 7:13:20
2 cm	555:33:20 - 3611:06:40	55:33:20 - 361:06:40	11:06:40 - 72:13:20	2:46:40 - 18:03:2 0	1:51:07 - 12:02:13	1:06:40 - 7:13:20	0:33:20 - 3:36:40
5 cm	222:13:20 - 1444:26:40	22:13:20 - 144:26:40	4:26:40 - 28:53:20	1:06:40 - 7:13:20	0:44:27 - 4:48:53	0:26:40 - 2:53:20	0:13:20 - 1:26:40
10 cm	111:06:40 - 722:13:20	11:06:40 - 72:13:20	2:13:20 - 14:26:40	0:33:20 - 3:36:40	0:22:13 - 2:24:27	0:13:20 - 1:26:40	0:06:40 - 0:43:20
20 cm	55:33:20 - 361:06:40	5:33:20 - 36:06:40	1:06:40 - 7:13:20	0:16:40 - 1:48:20	0:11:07 - 1:12:13	0:06:40 - 0:43:20	0:03:20 - 0:21:40
50 cm	22:13:20 - 144:26:40	2:13:20 - 14:26:40	0:26:40 - 2:53:20	0:06:40 - 0:43:20	0:04:27 - 0:28:53	0:02:40 - 0:17:20	0:01:20 - 0:08:40
100 cm	11:06:40 - 72:13:20	1:06:40 - 7:13:20	0:13:20 - 1:26:40	0:03:20 - 0:21:40	0:02:13 - 0:14:27	0:01:20 - 0:08:40	0:00:40 - 0:04:20

Table 6.21: Ratio between overall upload time and descending time, with given step size of scanning and upload rate. Assuming 4.32 Gbit/s as datarate of the imaging data.

Upload rate / Stepsize	0.1 Mbit/s	1 Mbit/s	5 Mbit/s	20 Mbit/s	30 Mbit/s	50 Mbit/s	100 Mbit/s
1cm	285.15	28.51	5.70	1.43	0.95	0.57	0.29
2cm	282.35	28.24	5.65	1.41	0.94	0.56	0.28
5cm	274.29	27.43	5.49	1.37	0.91	0.55	0.27
10cm	261.82	26.18	5.24	1.31	0.87	0.52	0.26
20cm	240.00	24.00	4.80	1.20	0.80	0.48	0.24
50cm	192.00	19.20	3.84	0.96	0.64	0.38	0.19
100cm	144.00	14.40	2.88	0.72	0.48	0.29	0.14

Table 6.22: Margings for the Ratio between overall upload time and descending time, with given step size of scanning and upload rate. Assuming a range of 1 Gbit/s - 6.5 Gbit/s as datarate of the imaging data.

Upload rate / Stepsize	0.1 Mbit/s	1 Mbit/s	5 Mbit/s	20 Mbit/s	30 Mbit/s	50 Mbit/s	100 Mbit/s
1 cm	65.36 - 430.46	6.54 - 43.05	1.31 - 8.61	0.33 - 2.15	0.22 - 1.43	0.13 - 0.86	0.07 - 0.43
2 cm	64.10 - 427.63	6.41 - 42.76	1.28 - 8.55	0.32 - 2.14	0.21 - 1.43	0.13 - 0.86	0.06 - 0.43
5 cm	60.61 - 419.35	6.06 - 41.94	1.21 - 8.39	0.30 - 2.10	0.20 - 1.40	0.12 - 0.84	0.06 - 0.42
10 cm	55.56 - 406.25	5.56 - 40.63	1.11 - 8.13	0.28 - 2.03	0.19 - 1.35	0.11 - 0.81	0.06 - 0.41
20 cm	47.62 - 382.35	4.76 - 38.24	0.95 - 7.65	0.24 - 1.91	0.16 - 1.27	0.10 - 0.76	0.05 - 0.38
50 cm	33.33 - 325.00	3.33 - 32.50	0.67 - 6.50	0.17 - 1.63	0.11 - 1.08	0.07 - 0.65	0.03 - 0.33
100 cm	22.22 - 260.00	2.22 - 26.00	0.44 - 5.20	0.11 - 1.30	0.07 - 0.87	0.04 - 0.52	0.02 - 0.26

Table 6.23: Mass calculation of the current design; expected nominal values

Component	Mass per unit	Number of Units	Total Mass
LIDAR	2.2 kg	2	4.4 kg
Optical Sensor and Lens	0.5 kg	4	2 kg
Battery	5 kg	1	5 kg
Rod-structure	4 kg	2	8 kg
Shelf	3 kg	1	3 kg
Pheripherie, controller and structure	2.6 kg	1	2.6 kg
			25 kg

6.5.3 Physical Interface

The mechanism for descending the sphere, most likely a winch, should be capable of holding, lowering, and pulling up 32 kg, consisting of 20 kg Sphere and 80 Meters of 150 g/m cable. The cable needs to be centered to one point, as unrolling would lead to a left to right movement of the cable. The cable centering mechanism should move up to 20 cm in each direction to fine adjust the path and control unexpected oscillations. As the last meter of the cable on the sphere side consists of multiple electronic parts, the centering mechanism has to have a varying opening. That part of the cable is not rolled onto the winch during transportation. During transportation, either a cooling system must be provided, or the poles need room to extend to cool the sphere down by the larger surface.

Table 6.24: Mass calculation of the current design; error margin ranges

Component	Mass per unit	Number of Units	Total Mass
LIDAR	2.0 kg - 2.4 kg	2	4.0 kg - 4.8 kg
Optical Sensor and Lens	0.3 kg - 0.7 kg	4	1.2 kg - 2.8 kg
Battery	5 kg - 8 kg	1	5 kg - 8 kg
Rod-structure	4 kg - 5 kg	2	8 kg - 10 kg
Shelf	2.8 kg - 3.2 kg	1	2.8 kg - 3.2 kg
Pheripherie, controller and structure	2.6 kg - 5 kg	1	2.6 kg - 5 kg
			25 kg - 33.8 kg

6.6 Shortcomings and Outlook on Risks

Due to the early stage of the project and design, some shortcomings need to be considered in further development and research. Also, some overall risks come with the basic concept. The Risks and shortcomings are categorized by their severity on the mission and how likely the problem occurs in the current state. Therefore the probability, if a risk or shortcoming, will be a problem in the final study is rated. Therefore the categories low, medium, and high are used. If a risk has a low probability, it means it has a low probability to occur. For shortcomings, this means the probability of not solving it is low. The exact definition of the categorizations and the risks and shortcomings will be part of the study's next phase. At this point, it provides just an overview.

6.6.1 Dust Mitigation

Category: Risk
Severity: High
Probability: Medium
Lunar dust is expected to be electrostatically charged by solar UV irradiation, solar wind and cosmic rays. Though within a pit the associated clinging property could be self-mitigated thanks to the shielded environment, the accumulation of dust particles on the DAEDALUS sphere should be in any case prevented. Several dust mitigation methods have been proposed and developed in the last decades, most of them aiming to increase the efficiency of solar panels and thermal radiators [1]. Of them all, active dust shields seem to be suited for a transparent sphere with an optical payload that rolls on a dusty surface. Specifically, shields based on electrostatic curtains use electrostatic forces to lift and move charged dust particles off surfaces, preventing accumulations (e.g., [9, 147]). As an example, the Dust Shield [31, 32] developed by the NASA Electrostatics and Surface Physics Laboratory of the Kennedy Space Center consists of a series of parallel electrodes connected to an AC source that generate a traveling wave that drives particles along or against the direction of the wave, depending on their polarity. Dust Shield can be made transparent and can operate under dry and high vacuum conditions: as long as the system is active, the surface remains free of dust. Such a shield can be adapted to a spherical shape and activate partially and sequentially during the rolling, aiming to maintain the FOV free of dust.

6.6.2 Lighting

Category: Shortcoming
Severity: Medium
Probability: Low

In the current state, the only source of light is the cable (see 6.2). However, for exploration trips, away from the cable, an own light source is needed. This should cover the same area as the coverage of the optical sensors. This is satisfied by multiple configurations of multiple light sources on the sphere. Therefore they will be implemented as a final design for the study is made and adapted to the positions of all components. Theoretically, an LED strip between the lenses, with a gap in the lidar, satisfies the requirement.

6.6.3 Length of Wire

Category: Risk
Severity: High
Probability: Low
The current study assumes a depth of 40 meters. Therefore, the design plans with 80 meters of wire. Technically a longer wire is possible. Depending on the length, the voltage and power need to be increased at the winch. Depending on the wire, a 300m is technically possible (with 4qmm, 1000W and 60V, 15V arrive at the sphere.)

6.6.4 Cable Load Rotation Speed

Category: Risk
Severity: Medium
Probability: Low
Even when using a rotation-resistant cable design as described in 6.2.2, rotation might not be fully compensated. The actuators inside the sphere allow to counteract some amount of torque if needed. Unfortunatley, prediction and modelling of load rotation, i.e the cable parameters, torque factor specifically, is not precisely possible since they change with every usage. This is why several tests have to be done with the cable/sphere setup to ensure that load rotation speed will not exceed a certain threshold, depending on mapping resolution criteria.

6.6.5 Pole Mechanism

Category: Shortcoming
Severtiy: High
Probability: Low
The current design includes 18 Poles (two Side poles and two poleholders with eight poles each). The mechanism for extending still needs to be investigated. An electrical and hydraulic solution is discussed. Between shelf and poleholder, there is enough space for a mechanism.

6.6.6 Cooling

Category: Shortcoming and Risk
Severity: Medium
Probability: Medium
The cooling is currently performed to the extraction of the poles and over the cable. This is by fare less plannable than the heating, as the heater can be dimensioned more easily than the cooling surface. Also, with more power, active heating can be performed quicker than passive cooling. This brings better controllability of the heating than cooling.

6.6.7 Weight Distribution

Category: Shortcoming
Severity: Medium
Probability: Low
The current design has the battery as a rectangular box at the foreseen place. As the battery is the main actor regarding weight distribution, its weight and therefore its volume must be maximized. This will be done by fitting the shape to the sphere's shape on the corresponding side and therefore maximizing the volume. Of course, this also leads to a higher capacity. If the shape is restricted due to the cells' shape, space that can not be filled by cells can be by, for example, lead to add weight.

6.6.8 Recoupling Mechanism

Category: Shortcoming
Severity: High
Probability: Medium
As of right now the proposed design requires the robot to recouple with the cable to recharge the battery. This demands the execution of a precise maneuver to steer the robot under the cable, tilt the robot and attach the cable to the charging pole of the robot. If this maneuver cannot be completed before the battery is depleted the robot is lost. Hence, the robustness of the recoupling procedure is very critical. Inspired by conversations with the team at the University of Oviedo (Robotic crane for wireless power and data transmission between surface and cave) we propose the following possible solution for further investigation. As shown in figure 6.23 the new recoupling mechanism consists of a metal ring on the sphere and a conical grasping interface at the end of the cable. The new coupling mechanism is a combination of magnetic and mechanical coupling and could proceed as follows:

1. The robot navigates approximately under the cable/interface.
2. The robot tilts partially onto its side such that the metal ring points towards the interface

Table 6.25: TRL definition by ESA

TRL 1	–	Basic principles observed
TRL 2	–	Technology concept formulated
TRL 3	–	Experimental proof of concept
TRL 4	–	Technology validated in lab
TRL 5	–	Technology validated in a relevant environment (industrially relevant environment in the case of key enabling technologies)
TRL 6	–	Technology demonstrated in relevant environment (industrially relevant environment in the case of key enabling technologies)
TRL 7	–	System prototype demonstration in an operational environment
TRL 8	–	System complete and qualified
TRL 9	–	Actual system is proven in operational environment (competitive manufacturing in the case of key enabling technologies; or in space)

3. The interface is put over the robot and the magnetic coupling is activated.

4. The robot slips into the position defined by the magnetic coupling.

5. The location of the poles is now aligned with the holes in the conical interface. The robot can extend its poles and thus establishes the mechanical connection.

6. The magnetic coupling can be turned of to spare energy.

This new recoupling procedure has a higher tolerance of error and requires less accurate pointing my the robot for a successful coupling. Further, it provides additional redundancy, since the coupling is possible via the magnetic interface, as well as the mechanical interface.

6.6.9 Technology Readiness Level

The Technology Readiness Level(TRL) estimates the maturity of technology. Therefore, it indicates which risk of realization of technical components exists and indicates whether and how much research is expected to be done for certain technology. Therefore the definitions by ESA of TRL, shown in table 6.25 will be used.

Optical System: TRL 4 The system with hemispherical lenses was tested successfully in a lab environment (see 3.2.2).

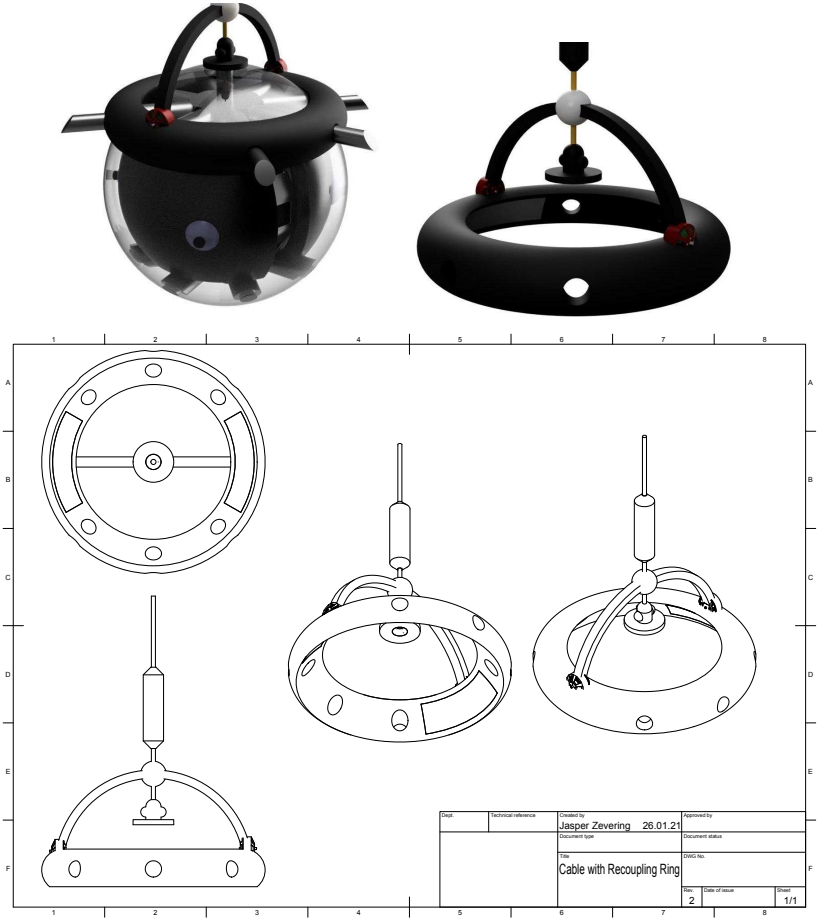

Figure 6.23: Proposed design for an improved recoupling mechanism. Top-Left: Render of how the ring attaches. Top-Right: The ring by itself. Bottom: Blueprint of the Ring.

LIDAR: TRL 4 The lasersystem was tested in descending and rolling mode in a lab environment (see 3.2.1)

Dual-wavelengths LIDAR: TRL 1 The chosen scanning principle of prism-based lidar allows for operation at different wavelengths. A concept to operate at two different wavelengths simultaneously needs to be further studied.

SLAM via LIDAR: TRL 6 The SLAM algorithm on LIDAR basis was demonstrated in caves at Lanzarote and therefore a relevant environment (see 5.2).

Locomotion: Change of center of Mass: TRL 3 There is an experimental robot proofing the concept of locomotion by changing the center of mass(see 3.1.3)

Locomotion: Rods: TRL 2 The concept of locomotion by extending rods and all other procedures involving them have been formulated and basic requirements for hydraulic rods have been named(see OM3-4 PRC1-3 in 6.4 and 6.6.5).

Heating mechanism: TRL 2 The concept of heating up the sphere by an external heater has been formulated and described (see 6.3.4).

Sphere shell: TRL 1 The basic requirements for the shell have been formulated. No space suitable technical solutions have been found (see 5.3 and 6.6.1).

Chapter 7

Related Approaches

This chaper discusses related approaches for robotic systems. The Daedalus sphere is designed to work in two stages of the exploration mission. In STG II the sensor system is lowered into the pit making measurements while descending to map the shaft. Section 7.1 presents a commercial system for mapping manholes and shafts in underground mines, an application similar to this stage.

In STG III the robot explores the pit floor autonomously requiring advanced mobility. For the Daedalus system the sphere design was chosen due to its ability to shield all sensors and control units from the harsh lunar environment. Spherical-shaped robots have gained special and notable interest in the scientific community in the last decade. Section 7.2 gives an overview about existing systems with a focus on the different locomotion schemes.

7.1 Wire Shaft Mapping System

DMT GmbH & Co. KG is an internationally active, independently working engineering and consulting company based in Essen, Germany. The tasks of DMT consists in improving mining training and research in mining with the aim of making work in mining safer. DMT has developed a so-called wire shaft scanner, cf. Figure 7.1 and 7.2, that consists among other things of a

camera which is a PtGray Ladybug panoramic camera,

laser scanner that is a Zoller+Fröhlich profiler, i.e., a single laser slice with a 360 degree field-of-view, and an

IMU which is a high-end inertial measurement unit.

The weight adds to a total of 182 kg and the total height is 218 cm. The wire shaft mapping system is used to map manholes and shafts in underground mines. After installing the system the mapping is performed by moving the scanner from the bottom of the mine upwards. During

the lifting motion, the whole unit rotates and performes pendulum motions such that the 3D point cloud becomes inaccurate. The Telematics group in Würzburg cooperated through the Nuremberg Institute of Technology Georg Simon Ohm with the DMT group in the project EU-funded project UNDROMEDA[1] for underground mine mapping.

Compared to this wire shaft scanning system our system is lightweight. Boths system do not use the laser scanner to scan in the up- or down-directions. The camera used in the shaft scanner does not enable any stereo vision.

[1] https://eitrawmaterials.eu/project/undromeda/

DMT

DMT Wireline Shaft Mapping System

Your shaft in a new dimension

The **DMT Wireline Shaft Mapping System** is a fast, complete, reliable and precise laser scanner for a geometrical and photorealistic documentation of shaft lining, installations and shaft position in 3D.

The system comprises a 2D laser scanner, an Inertial Measurement Unit (IMU) and a panoramic camera to give comprehensive documentation of vertical shafts.

While the main data is stored internally in the tool, excerpts are transmitted over the cable and thus allow for online monitoring of the logging.

The modular setup allows for easy handling and installation on site.

The acquired data can be used for numerous applications, example:

- Documentation (by processing to images of the unwrapped shaft wall)
- Infrastructure planning (by converting into 3D CAD model)
- Documentation and monitoring of damages and changes, e.g. deformations (by comparison of different shaft slices over time)

Your Advantages:

- Minimal disturbance of business operations thanks to very fast data acquisition
- Enhancement of safety level by avoiding dangerous work inside the shaft
- High precision by using modern and field approved measuring and evaluation technology

High reliability guaranteed by long time experience in international mining projects

Figure 7.1: The wire shaft scanner.

Technical Data		
Tool length	Total	218 cm
	Without cable and laser protection	207 cm
	Telemetry module	55 cm
	Camera module	40 cm
	IMU module	48 cm
	Battery module	27 cm
	Laser module	37 cm
Tool diameter	Laser module	33 cm
	All other modules	26 cm
Weight	Total	183 kg
	Telemetry module	23 kg
	Camera module	27 kg
	IMU module	42 kg
	Battery module	37 kg
	Laser module	39 kg
	Cable	0.5kg/m
Maximum depth		~2000 m
Maximum temperature		40° C
Working time		~2.5 hrs
Vertical resolution at standard deployment		< 1 cm
Horizontal resolution at 6 m shaft diameter		< 2 mm

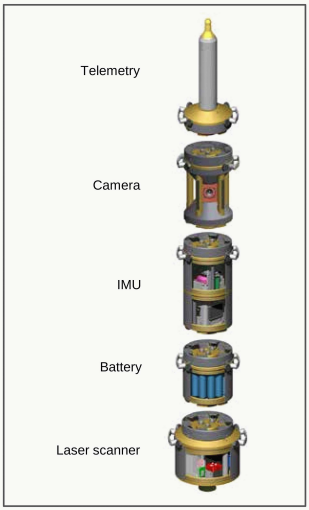

System-Modules

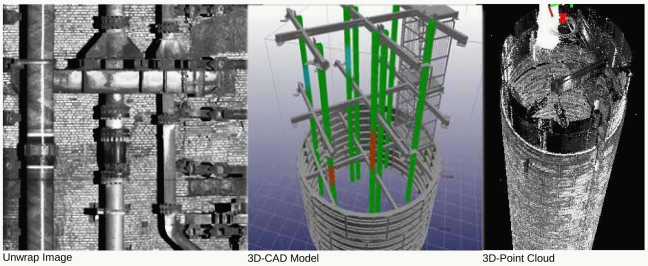

Unwrap Image 3D-CAD Model 3D-Point Cloud

DMT GmbH & Co. KG

Am Technologiepark 1
45307 Essen, Germany

Phone +49 201 172-1970
Fax +49 201 172-1971
exploration@dmt-group.com
www.dmt-group.com

TÜV NORD GROUP

DIN EN ISO 9001 certified | DIN EN ISO 14001 certified

Figure 7.2: The wire shaft scanner (cont.).

7.2 Spherical Exploration Robots

Due to the growing interest in the exploration of caves both on earth and in other celestial bodies such as the moon and other planets of the solar system, spherical-shaped robots have gained special and notable interest in the scientific community in the last decade, where these type of scout robots can help map and perform terrain identification tasks, which may be crucial in future human exploration missions, but also in locating potential sites to host future human colonies outside of their mother planet. However, it is not necessary to explore the depths of the Earth's crust, or leave the orbit of the planet to find applications that can be very useful for everyday citizens. In fact, these robots can be especially useful developing actions of search and rescue during earthquakes, landslides, or even in a building collapse, where every second counts in saving human lives. Thus, the design is crucial, but also the materials are highly important, since the durability of the robot and the extent of the tasks it performs depends on this. Usually, the type of material used to manufacture the main sphere, which is generally polystyrene, although some authors have used additive manufacturing (3D printing) to make the main sphere, the friction with the ground surface is crucial to allow a proper movement around the surroundings. Then, one of the most prominent research challenges on their design is the ability to have a driving system that allows the spherical shell to rotate freely in all degrees of freedom indepentend of the current direction of motion or orientation [38]. For this, researchers devised a number of propulsion mechanisms and governing principles to address the aforementioned challenge. However each mechanism and principle comes with certain limitations and trade-offs. Thus, this section covers the propulsion mechanisms used on current spherical-shaped robot projects.

7.2.1 Drivetrain systems for spherical robots

Spherical robots achieve motion by transferring power from the internal body of the sphere to its shell [39]. Multiple ways of propelling spherical robots have been developed. Often times the movement of a spherical robot occurs due to the change in its center of mass, allowing the entire structure to move in the direction of such change, produced usually by different internal drive units using wheels and masses distribution configurations such as: a pendulum located on the rotating axis, a 'hamster ball' or 'hamster car', a single wheel configuration, a gimbal mechanism, omni-wheels, change of masses configuration, orthogonally mounted flywheels, or a flywheel on a pendulum, and parallel mounted flywheels. The driving force on most of these robots is direct drive, but for others, the movement is produced by a change in the angular momentum or just using the gravitational force. The following literature review includes some of the most important and relevant locomotion techniques for operating in a hazardous environment. An overview of these techniques is given in Table 7.1.

Mechanism Type	Slopes <30°	Obstacles 1/10th of its diameter	Extension	Advantages	Disadvantages
Pendulum	No	No	None	Few and simple mechanisms	Low torque
Hamster ball	No	No	None	Holonomic	Restricted materials
Shift of masses	No	No	None	Holonomic	Complex control low torque
Deformable models	Partially	Yes	Deformable Skeleton	Able to leave hollows	Limited materials, weight of the robot, fixed initial unstucking state.

Table 7.1: Characteristics of the different configurations of spherical robots [112].

Pendulum

The most commonly used technique to achieve motion in a spherical robot is by utilizing a pendulum. The pendulum drivetrain system consists of a base frame connected between the left and right hemisphere of the robot aligned with the rotating axis and a pendulum system attached to it. In order to achieve motion, the pendulum system follows the governing principle of the Barycenter Offset. This concept refers to achieving motion in a robot by shifting the center of mass. As shown in Figure 7.3 moving the pendulum perpendicular to the base frame causes the sphere to move. The center of mass of the sphere changes and the robot moves to a new position of equilibrium. Moving to a specific angle continuously, the pendulum provides the needed impulse that enables the shell-sphere to keep the momentum going. When rotating a mass around the fixed axis to the left or to the right, the sphere will start to turn [39]. This rotation has a mechanically limited range but enables side movements [112] [34] Research done by Hernández et al., on pendulum-driven robots, determined that the rotation angle is an important factor to induce locomotion to the system, their research demonstrated that the further the center of mass is from the geometrical center, the smaller the angle needed to produce motion, inducing momentum more easily [70].

Roball A first prototype designed by Michaud and Caron in 1998, Roball is intended for several applications: as mobile robotic platform to be used as a toy, as a pedagogical tool to help kids and teenagers with autism [102], or as a planetary surface exploration robot [103]. Roball's dynamics create interesting new interplay situations with children, and this same concept will be used in the next decade for several toy companies worldwide, but also in movies, such as Disney's Star Wars BB8, which will be discussed in further detail later in this report. Roball

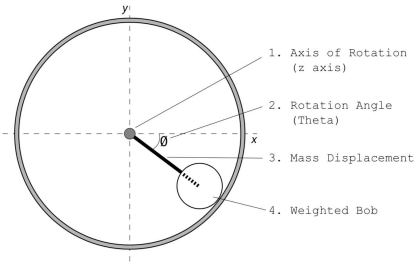

Figure 7.3: Principle of motion in a pendulum driven robot by shifting the mass out its equilibrium position to cause a rotation of the sphere [39].

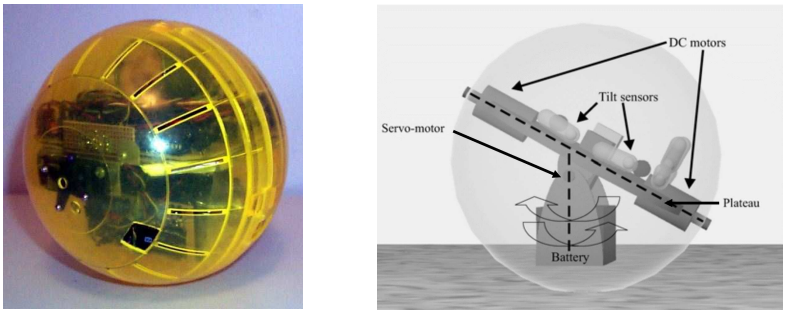

(a) **(b)**

Figure 7.4: First prototype of Roball and the Propulsion and steering mechanisms [102].

has a plastic-shell diameter of 15 cm and weighs around 2 kg. It also incorporates a Motorola 68HC11 microcontroller board, placed over a plateau. Two DC motors are located on the side of this plateau, perpendicular to the front heading of the robot. Both motors are attached to the shell as shown in figure 7.4b, and move the robot forward or backward by changing the center of gravity of the plateau. The speed of the DC motor is regulated based on longitudinal inclination of the internal plateau, keeping the center of gravity of the entire system closer to the ground. Steering mode was done using the 12 V 1.2 Ah non-spillable rechargeable SLA battery as a counterweight mounted on a servo motor, allowing the robot to tilt to one side or the other [102].

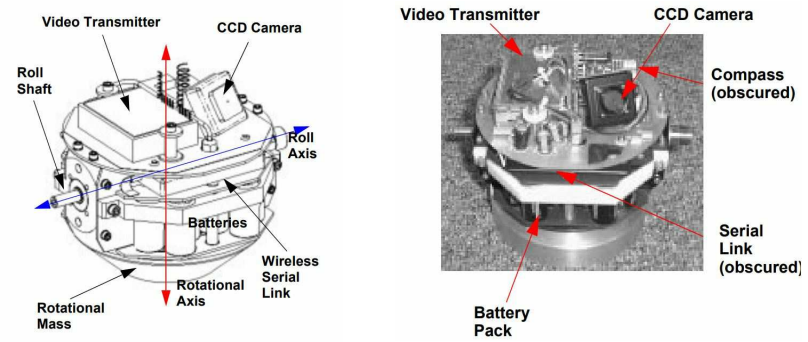

Figure 7.5: CAD model and Cyclops prototype the its mechanisms [40].

Cyclops Designed by Chemel et al. [40], in the Robotics Institute at the Carnegie Mellon University, with the purpose of forward reconnaissance role and patrol agent, scanning either unknown and secured areas following a pre-set patrol route through an indoor space, Cyclops is composed of a 14 cm diameter transparent acrylic sphere, with a vertical tread strip for improving the friction with the ground. The 2-DoF locomotion shown in figure 7.5a is generated by a forward/reverse rolling mechanism with inertial steering. A rotating inertial actuator allows pivoting in place along its vertical axis, and a small motor and gearhead provides forward and backward movement along a fixed horizontal axis. The rotational mass is attached directly to the output shaft of an electrical motor that accelerates it in seconds. The voltage applied to the motor is controlled by one of the three onboard microcontrollers linked to a standard H-Bridge motor driver chip, and the applied torque to the mass is controlled by varying the motor control signal output from the microcontroller.

A miniature ceramic gyro (used for producing smooth rotations) and an electronic flux-gate compass control inputs for the torque system, providing information on angular rate at nearly 10 Hz and heading data at 5 Hz, respectively. The control subsystem of Cyclops are three PIC16C73A microcontrollers and a wireless serial transceiver, connecting the robot to the operator's remote control station.

Rosphere Developed by the Robotics and Cybernetics Research Group at the Universidad Politécnica de Madrid (UPM), Rosphere's goal is to perform inspection tasks, such as agricultural crop monitoring [146]. In order to keep the friction force with the ground to create traction, the Rosphere's shell of 30 cm in diameter incorporates rubber ridges. The driving mechanism consists

(a)

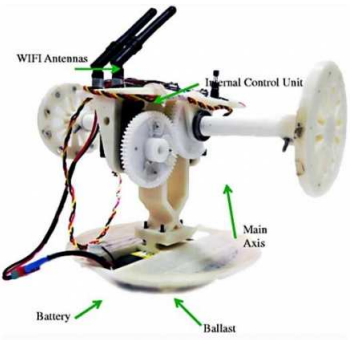

(b)

Figure 7.6: Mechanical framework of Rosphere rolling robot [123].

of a pendulum with a capacity of two independent motions with a hanging mass as ballast and the central control unit fixed to the main axis. The hardware includes an embedded computing system using a Robovero and an Overo Fire. It also incorporates Wi-Fi, Bluetooth, and Xbee modules as communication mediums for transmitting and receiving data to the base station, but it can also send data to external sensors. Navigation and control (GNC) systems, such as a low-cost inertial measurement unit (IMU) for measuring angular velocities and accelerations, a magnetometer with pan-tilt correction capability, and a single GPS, are included as well [70].

The 3D printed mechanical assembly consists of two wheels that make direct soft-contact with the inner shell-sphere, in such a way as to allow it to move with a certain degree of friction, as shown in Figure 7.6b. The central axis is constructed so that the servo transmits the movement to the axle using a simple gear train, located just below the central computer unit. Also, to stabilize the system in stationary and moving states, the servos are located in positions making the center of mass as close as possible to the pendulum body axis. Finally, the ballast is where the batteries are contained and the mass that is moved to generate back and forward movements. The team behind this project measured in-situ environmental variables in crop fields (ref. Figure7.6a), where the robot shape is suitable for rolling and gathering information that can be used to monitor precision farming techniques [123].

Groundbot Developed by Rotundus AB in 2009 [81], composed by a polycarbonate spherical shell of 60 cm in diameter covered with rubber, and capable of navigating different types of terrain, including mud and water with an acceleration of up to 3 m/s, the rolling movement is achieved by displacing the sphere's center of mass. The counterweight is mounted on the axle

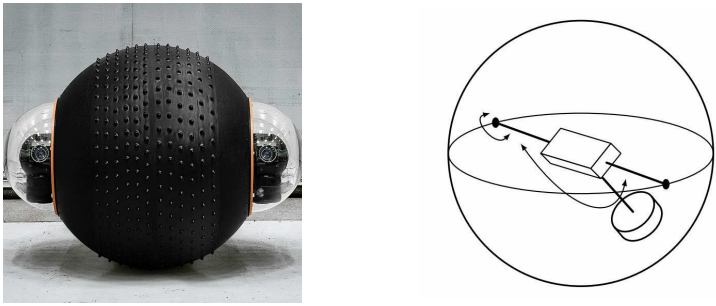

(a) (b)

Figure 7.7: Groundbot spherical robot and its schematic illustration [136] [81].

framework rotating around the central axis by two perpendicular motors. Most of the pendulum weight is composed by a lithium-ion battery pack able to provide power for up to 12 hours of continuous operation [137]. The ICU is composed of a PC/104+ format computer with an 800 MHz Crusoe CPU, and a long-range 802.11a/g wireless network card. Two pan-tilt-zoom network video cameras, providing 360 degree field-of-view with JPEG (M-JPEG) video stream to the tele-operation interface, and attitude-controlled through a VISCA (over RS-232) interface by the internal control unit (mission computer), are located at the intersection of the shell with the main axle, adding 20 cm to the robot's width. The robot's pendulum is controlled by two motors, one motor for each of the pendulum's DoF: the longitudinal rotation is controlled by the drive motor, and the position of the pendulum positioning allowing sideways motion and lateral rotation is controlled by the steer motor.

Groundbot also includes a Microstrain 3DM-GX1 gyro enhanced orientation sensor, located at the center of its body, including three accelerometers to measure Earth's gravity, three magnetometers to measure magnetic fields, and three rate gyroscopes to measure rate of rotation along and about the respective axis of each sensor, allowing to provide Euler angle attitude measurements [136].

Picorover A project proposal from Universitat Politècnica de Catalunya includes a mobile lunar rover as part of the FREDNET team of the former Google Lunar X-Prize. PicoRover was one of the three rovers intended to be sent to the Moon, incorporating the pendulum-driven system described above. In this proposal, the shell-sphere was manufactured out of Methacrylate, but for the final implementation, the team was considering to manufacture it using aluminium with a lateral glass window (similar to Groundbot) [92].

The first concept of the rover was proposed in 2010 with a sphere diameter smaller than

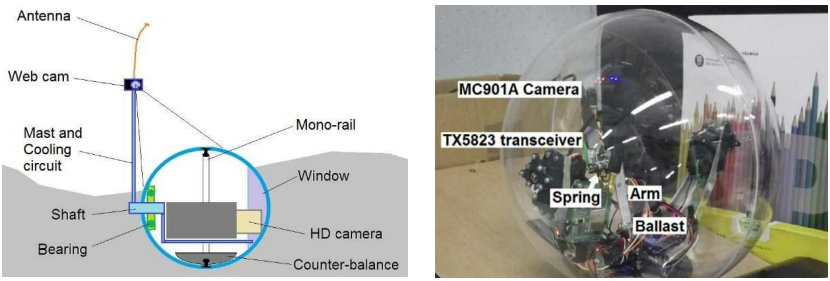

(a) **(b)**

Figure 7.8: PicoRover prototype design and engineering model [92]

0.15 m, and weighting less than 500 gr. It incorporated an external arm which held a data transmission antenna and the HD camera, as seen in Figure 7.8a, connected to the internal control unit through a shaft. A bearing allowed the spherical-shell to move freely [152]. However, further designs moved all the subsystems and payload inside the shell, as seen in Figure 7.8b. The purpose of the payload camera MC901A (18 mm × 9.5 mm × [9]mm, and 1.1 gr) is to transmit a HD video to the Lunar Lander using a TX5823 transmitter (22 mm × 19 mm × 3 mm and 2.2 gr). Both systems are attached to an arm, close to the the geometric centre of the sphere, which has a small weight on the opposite side to compensate the moment created by the camera and transmitter masses. The small weight tends to keep the camera in the highest elevation.

The arm acts like a seesaw pendulum that pivots in the shaft (which is an M3×50 mm steel bolt of 3.2 gr) in the centre of the PicoRover. Additionally, a spring for damping is allocated in the shaft, as seen in Figure 7.9. The team also allocated a servo attached to the lateral of the sphere aligned with the turning axis. Further field test showed that there was interference due to the two reception antennas placed together, as well as the proximity of the servos to the video-link antenna.

Maneuverable Rolling Robot Designed by David Carabis in 2013 at Union College New York [35], this spherical-shaped robot features a polycarbonate sphere with a diameter of 46 cm, using a counterweight attached to a carriage plate that is hanging from the driveshaft through four mounting brackets. Thus, no direct contact is made with the inner spherical-shell as seen in Figure 7.10a. The author used two pillow block ball bearings connecting the counterweight to the driveshaft, the Gearmotor 37Dx54Lmm 12 V is linked by two gears (with a 1:1 ratio) to the shaft, and the sphere is driven by a Futuba servo with a gear and rack configuration, as shown in Figure 7.11a. This servo was modified in order to turn around 180 degree allowing the rack a full motion of about 5 cm in either direction. This mechanism is rigidly attached to the

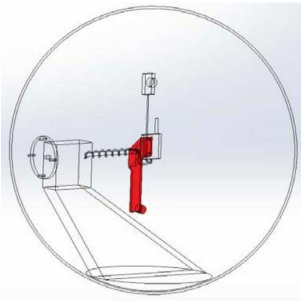

Figure 7.9: Arm CAD model

(a)

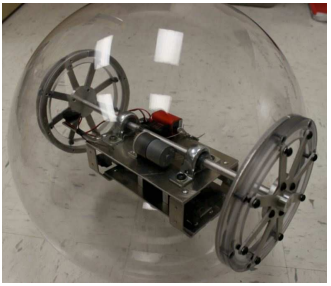

(b)

Figure 7.10: CAD model and engineering model [35].

spherical-shell by two polycarbonate and aluminum mounting plates, both bolted into the shell as seen in Figure 7.10b.

The counterweight is composed of two small masses mounted inside the aluminum undercarriage on a flat piece of ABS plastic (chosen for its low frictional coefficient) which is shifted either left or right by the servo with the gear and rack. A 12 V NiMH battery pack mounted in the undercarriage is used for powering the forward and backward motion mechanism. A second 6 V NiCd battery pack mounted atop the carriage plate is used for powering the servo and radio control receiver. Industrial grade Velcro is used to fasten the turning weights to either end of the rack.

The banking mechanism in Figure 7.11b is placed within the undercarriage, allocating the Futuba servomotor, the gear, the rack and its mounts, and the two weights. The rack is composed of a plastic gear rack, and a larger square-stock piece of ABS plastic sliding over the aluminum

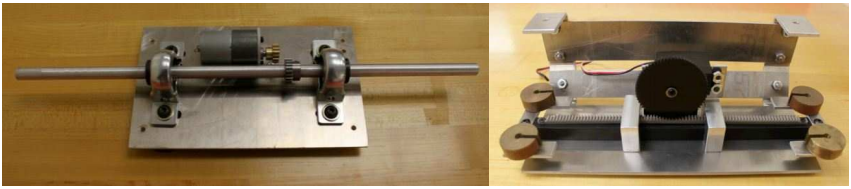

(a) (b)

Figure 7.11: Gear and rack mechanism (left); banking mechanism (right) [35].

undercarriage plate, and two rack-mounts stop the latter from moving upwards or laterally.

Finally, one circuit for the driveshaft motor, and another circuit for the radio transceiver and servo control are used in this approach. Given the differences between the voltage and power requirements from the drive motor and the banking servo, both circuits are not integrated with one another. In order to provide speed control and reverse direction for the driving motor, the author integrated a FingerTech tiny ESC motor speed controller into its circuit [35].

Norma Designed by Moazami et al. [106] at Lamar University in Beaumont, TX. in 2019, this 2-DoF mobile spherical robot under the shifting gravity center concept, consists of a transparent rigid spherical-shell, a fixed diagonal shaft attached to two plates bolted to the shell (similar to Carabis 2013 [35]), and two actuators: a linear slider and a rotational pendulum. As illustrated in the Figure 7.12, the servo is connected to the shaft via a drive belt, transmitting torque to the shaft which rotates to propel the robot to roll forward and backward. The linear slider translates a sliding weight (composed by one of the battery packs) along the axis of the shaft. This translation motion shifts Norma's center of gravity in the transverse direction. This is translated in the shaft and the sphere to tilt about the longitudinal axis, giving the robot the ability to roll towards the longitudinal axis and to tilt around the same axis, thus enabling a non-holonomic turning motion.

Salamander A two-axis pendulum mechanism spherical robot with amphibious capabilities was proposed by Satria et al. [131], in 2015 at the National University of Singapore as a tool for providing assistance in coastal and marine biology, as well as research on search and rescue missions. Salamander design has a similar configuration as Groundbot but is less bulky with a sphere of 15.5 cm in diameter and the total weight of 807 gr, meaning that it is a small and light robot relative to previous amphibious versions. The fixed two-axis pendulum for the robot's powertrain is battery-powered, providing the robot with a self-righting capability. The outer-shell incorporates a custom-made 3D-printed NinjaFlex sleeve with 1.75 mm ridges designed to improve the robot's traction and propulsion on both land and water. This robot configuration

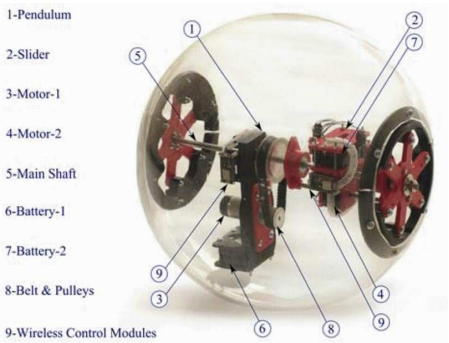

Figure 7.12: Engineering model of Norma Robot [105].

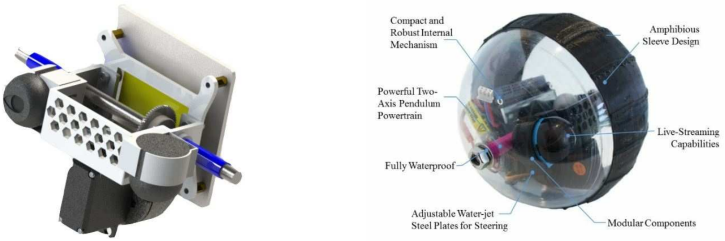

(a) **(b)**

Figure 7.13: Two axis pendulum mechanism (left); engineering model features (right) [131].

also integrates two Ai-Ball live-feed cameras mounted on each side of the robot's main housing, providing live-streaming, but the system structure was designed in a way that both cameras can be replaced by other sensors if needed. As seen in Figure 7.13a, the team mounted one camera as forward-facing and the other one as downward-facing, enabling under water monitoring while maintaining the forward view. Two 3D-printed mounts were designed to hold the cameras, and M2 screws are used to secure the two mounts in place. The team also added a GPS module enabling real-time tracking of the robot's position via Google Maps [132].

Salamander is driven by a Pololu 298:1 Micro gear Motor with a 3:1 gear ratio, the team used Newton's second law for rotation determining that a gear ratio of 100:1 Micro gear Motor with the same 3:1 gear ratio would be enough. A 20-teeth, 0.5 module Delrin spur gear is placed on the motor shaft, and a 60-teeth, 0.5 module Delrin spur gear is mounted on the shaft. A

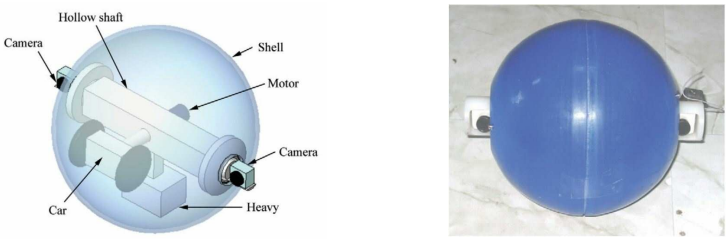

(a) (b)

Figure 7.14: Structure and prototype of BHQ-2[30].

safety factor of 3 improves the robot's reliability. Similarly, the steel counterweights mounted below a custom-made box on the secondary mild-steel pendulum are driven by an HS-422 servo, this main box also houses various sensors, such as the MPU6050 Triple Axis Accelerometer, a Gyro Breakout, and the HMC5883L Triple Axis Magnetometer. This box is held in place by two custom-made 3D-printed spacers, and the 60-teeth spur gear is fixed on the shaft by a M3 set screw [132].

BHQ-2 Based on a previous version called BHQ-1 by Cai et al., in 2011 [30] which was focused only on the dynamics of the spherical shell, and simplified by the Boltzmann-Hamel equation [121] the BHQ-2 project was instead focused on a neural network compensation method to solve the dynamics control with one underactuated DoF [157]. The application behind the BHQ project idea was unmanned environment land-exploration, and the robots were composed of a two-wheeled car propelled by a servo and fixed on the hollow shaft through a link. A main motor driving a counterweight pendulum is fixed on the hollow shaft and tied to the counterweight by a link, a second servomotor drives the counterweight to swing around the motor shaft, and two cameras are located at the ends of the shaft that protrude from the sphere. As seen in previous versions, two ball bearings connect the shaft to the shell. Its cubic shape is used as a frame where the other components are installed.

The cameras transmit the images to the control center through a wireless transmission system. The robot is controlled by an operator that remote controls every step of the robot. The rolling movement is achieved when the car moves on the inner-shell surface, making all the system components rotate at once, thus, causing the center of gravity to offset creating a gravity moment moving the robot on a straight line. A rotation of the motor rotates the counterweight pendulum around the motor axis, creating a side offset of the gravity moment to drive the robot to tilt aside. Thus, both motions of BHQ-2 can be easily achieved by joint control of the car and the motor [30, 121].

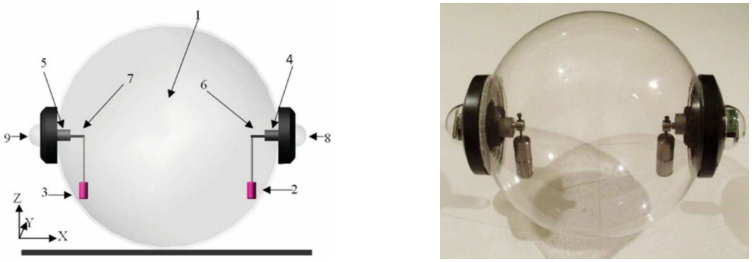

(a) **(b)**

Figure 7.15: CAD structure and Prototype of SMR[99].

SMR Developed by Mahboubi et al., in 2011 at the Mechatronics Research Laboratory, from the University of Tabriz, in Iran [99], the robot is composed of a spherical-shell, two pendulums attached to two DC motors with gearboxes for linear motion, and two control units. This design incorporates four modes such as *driving* and *steering*, achievable while moving two internal masses (both independent from each other), giving the robot the ability to move along straight and circular trajectories, respectively. The *jumping* mode overcomes obstacles, and on the *zero-radius turning* mode the robot can rotate on the spot about its vertical axis to improve the motion flexibility [99].

As seen in Figure 7.15a, the internal systems of SMR is composed of one internal driving unit (IDU) that incorporates two pendulums indicated by numbers 2 and 3, two geared DC motors 4 and 5, and two small linear motors or two ball screws for linear motion (Elshin Linear Motor, ELM) of the pendulums numbered by 6 and 7, connected between the pendulums and DC motors. These ELMs are controlled by two control board units located at opposite ends of the robot alongside two RF radio connection modules protected by two transparent cases as indicated by numbers 8 and 9. The *straight trajectory motion* of SMR is carried out by keeping the two pendulums symmetrical on both sides of the robot, achieved when the DC motors run in the same direction, causing the pendulums to rotate about the X-axis displacing the gravity center of the robot. *The steering mode* is achieved when the ELMs shift the positions of the pendulums towards the side, which displaces the center of gravity, tilting the robot to the left or right depending on the side that the center of gravity is displaced. Finally, *the jumping mode* of the SMR is achieved when both pendulums rotate in two opposite directions simultaneously, and when reducing the speed of rotation of the pendulums. SMR can rotate with zero-radius turning [99].

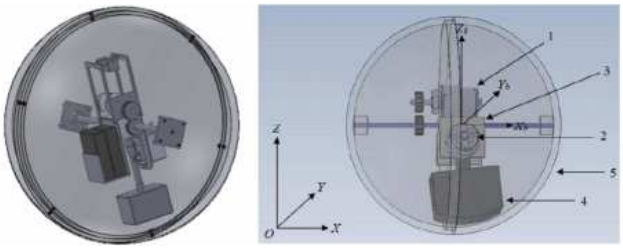

Figure 7.16: Spherobot CAD assembly view [120].

Spherobot Designed by Pokhrel, Deepak, et al. in the Department of Mechanical Engineering at EIILM University in India, with a shell-sphere of 32 cm, and weighting 2.910 kg without the counterweight, this design implements the principle of an inverted pendulum [120]. As seen in Figure 7.16, the robot propulsion system is composed of the driving and steering motors indicated by numbers 1 and 2, which drive the counter and rotate about the horizontal and vertical axes. To roll along the straight line, a driving torque is generated along the vertical axis while a leaning torque along the horizontal axis will make the sphere turn. The main shaft is connected to the shell at two ends through a square plug and socket, serving as frame to install other subsystems. The output shaft of one motor is fitted with a spur gear that meshes with another spur gear mounted on the main shaft, which is connected to the shell by two square plugs and sockets at the end. The internal drive unit indicated by number 3, is also mounted across the main shaft. The counterweight of the pendulum, indicated by number 5, is connected to the shaft of the second motor by a link.

In order to control the motion, a micro-controller drives the two geared motors in clockwise and anti-clockwise rotation through an H-bridge. Additionally, a 3-axis gyro is used for correcting the course of motion of the robot from environmental disturbances. The robot is currently controlled manually but for autonomous control an infrared (IR) sensor can be installed. The video taken from the wireless camera is transmitted to the monitoring station and saved automatically using a USB-based tuner card [120].

KisBot II A spherical robotic design was developed by Yoon et al. to improve the maneuverability and overcome the mobility disadvantages of a singular pendulum driven robot [160]. Instead of having just one pendulum hanging in the middle of the internal frame, this robot consists of two curve-shaped weights connected to the left and right side of the main axis that can be driven either independently or at the same time. Utilising two pendulums enables the robot to turn on the spot by deflecting both weights in the opposite direction and spontaneously

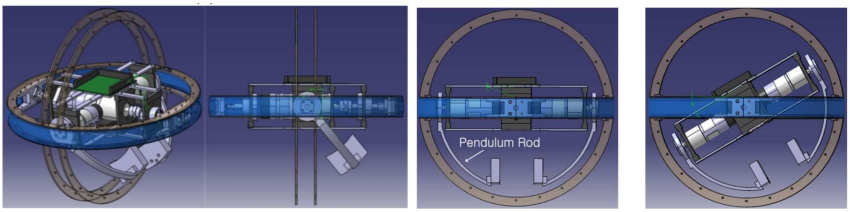

(a) (b)

Figure 7.17: CAD design of KisBot II [160]. (Left) The spherical robot is being propelled by shifting the two masses out of their equilibrium. (Right) In addition to moving the two individual weights, the sphere can be propelled by rotating the main frame of the robot, following the same principle of motion by shifting the center of mass.

releasing them to fall back into their initial position. The created momentum allows the robot to turn on the spot. Figure 7.17a shows how the weights move inside the sphere and achieve motion by changing the center of mass.

Furthermore, the internal body can be rotated perpendicular to the movement of the two individually movable weights via an electric motor as shown in Figure 7.17b. This allows the robot to move not only forwards and backwards, but also to the left and to the right. The novel idea here is to combine both driving principles to create omnidirectional motion.

In tests carried out with the robot driving in a straight line or performing strictly circular motion it was shown that the robot could follow the line and circle well, but was not spared of small deviation from the trajectory. According to the authors reasons for small deviations could be due to the complexity of the drivetrain system such as perfectly synchronizing the two weights. They also mentioned that the oscillations could arise from the unevenness of the ground implying that a rougher terrain required the robot to have a much better stabilisation system. With respect to the mission goal of the robot to drive on moon-like terrain, it makes this drivetrain system less favourable or at least more complex to control. There were also no tests conducted driving up a slope or over obstacles. This robot developed in [160] contains a novel idea of a double pendulum system to achieve omnidirectional motion that still needs enhancements to function more reliable.

Conclusions pendulum drive While the pendulum method has been widely implemented, it has a few drawbacks. The maximum amount of torque the robot can produce is limited, since the mass cannot be shifted outside of the sphere. Increasing the weight would lead to an increase in torque, however the energy required to move the robot would also increase [39]. A careful balance is needed for optimal propulsion. Due to the size of the pendulum system,

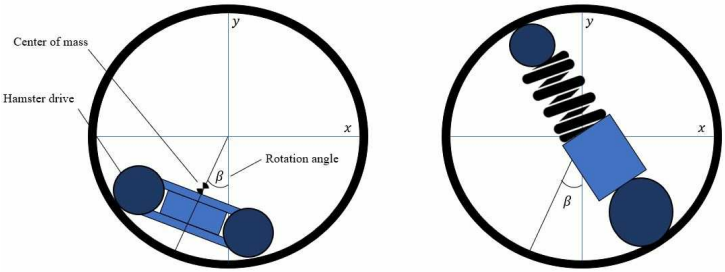

Figure 7.18: Cross-section of a spherical robot concept with Hamster mechanism [4].

more than half of the inner sphere will be occupied for locomotion resulting in little to no space for the mission's intended sensors and camera technology. Furthermore, this type of drivetrain system is non-holonomic meaning that the robot needs to be moving in order to turn. Another weakness of spherical robots using a pendulum is that it has difficulties driving in a straight line without shaking or oscillating to the left and right.

Internal Drive Unit (IDU)

The motivation behind an internal drive unit is to improve the mobility of spherically shaped robots by controlling the steering mechanism independently from the driving mechanism, creating a higher degree of holonomy [161]. In the most simple configuration this spherical-robot is composed of a wheeled mechanism, similar to a hamster wheel, resting inside the sphere as seen in Figure 7.18. Using a similar principle to the pendulum-based model, the movement of the vehicle changes the location of the center of mass of the system, as most of the mass of the sphere is concentrated in the internal wheeled vehicle. In order to ensure constant motion of the sphere, an internal wheeled vehicle with enough grip to the internal wall of the sphere is needed [112]; however, the driving mechanism can be either an internal car or sprung central member.

A wheeled mechanism with differential drive leads to omnidirectional locomotion. A further omnidirectional configuration is shown in Figure 7.19, the top half of the design controls the direction of motion, while the lower half is used for propulsion. Since both systems are connected, the upper wheel changes the orientation of the lower wheel by moving on top of the plate. Nevertheless, the same governing principle as in a pendulum driven robot is being used here. The robot moves by driving up the sphere and thus changing its center of mass. However, in this example the velocity of the robot is being controlled by the angular velocity of the wheel.

Generally in IDU driven robots, the contact between the wheel and the inner shell of the robot needs to be established at all times. Increasing the friction will however also increase the

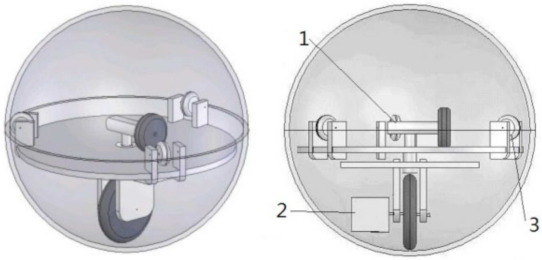

Figure 7.19: Structure of the IDU driven robot presented by Zhan et al. The lower wheel propels the sphere by driving up the shell while the upper wheel changes the orientation of the lower wheel and thus the orientation of movement [161].

energy needed to propel the sphere. More advanced designs that utilize omni-drive wheels to increase the robot's operability will also suffer from this dilemma. Choosing a material for the wheels needs careful consideration as it should not wear off too fast. Another challenge presents with the orientation of the cameras and sensors. Since the shell of the robot constantly changes its orientation, the cameras and sensors cannot be mounted directly into the shell. One solution would be to make the sphere transparent and place the cameras behind the shell. Considering the ground composition on the moon or even here on earth, the robot will get dirty very quickly thus blocking the view for the cameras and sensors. The following presents several systems using an IDU.

BHQ-3 BHQ-3 is the continuation of the research done on spherical robots by Yao Cai and his team in the Robotics Institute at the Beijing Aeronautics and Astronautics University in 2010. BHQ-3 uses the principle of barycenter offset for achieving its omni-directional motion as shown in Figure 7.19. The robot is designed using a sphere with a diameter of 24 cm, and the system's total weight is 1.12 kg [161]. The system incorporates three small supporting wheels, to prevent the latitudinal slipping, placed on a plaque with the wireless camera and the rest of the science sensors. The friction torques between the three small supporting wheels and the inner shell cause the motion of the sphere. BHQ-3 also uses two DC drive motors. The first one (M2) placed on the top of the plaque is used to change the direction of the latter causing a steering movement in arbitrary directions. The second motor (M1) drives the big wheel located underneath the plaque, and the change on the moment of gravity moves the entire IDU causing BHQ-3 to have a straight motion either forward or backwards. Both motors move the robot in arbitrary directions with zero turning radius [161].

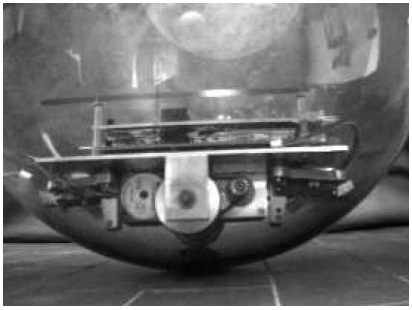

(a)

(b)

Figure 7.20: (Left) Close up of Sphericle rolling mechanism [20]. (Right) Prototype of Alves and Diaz hamster spherical robot [4].

Zhan et al. state that the robot could climb a slope up to 17 degrees and has the ability to overcome a 30 mm obstacle [161]. Despite small shaking during the acceleration, the authors reported great performance capabilities. The robot was tested in different environments such as smooth floors, sand, tarmac and water, but performed best on a flat terrain. Changing the outer shell of the sphere to a material with more grip would increase the traction towards the ground. The paper did not include any long-term testing to estimate the wear of traction between the wheel and the shell. Additionally, the study conducted by Zhan et al. did not provide any information about the power consumption, which is very important to consider when choosing a drivetrain system for operating in an environment like the moon.

Sphericle Developed by Bicchi et al. in 1997 [20], this spherical vehicle with all the subsystems such as actuators, drivers, sensors, battery pack, and radio modem are mounted on a plaque on the top of the moving mechanism comprised by a small car with unicycle kinematics. The control logic is partly implemented on-board, but also in a base-station sending planning control commands to the microcontroller TI TMS370C756 mounted on-board, through a two-way serial radio link at 19200 bps guaranteeing communications to within 80 m in a noisy environment. In this is a hamster-like mechanism, gravity keeps the car in contact with the spherical shell rolling without slipping, with two elastic suspensions mounted as well on the front and back of the car. The system integrates two motors with 200 steps per revolution and a 3.2 belt reduction gear. This circuit is driven by a square wave generated directly by the microcontroller. The entire setup acts like a free-pendulum and its angle is measured by the encoder, then the microcontroller uses this position to implement a local feedback stabilization controller, which is then superimposed to the path following commands [20].

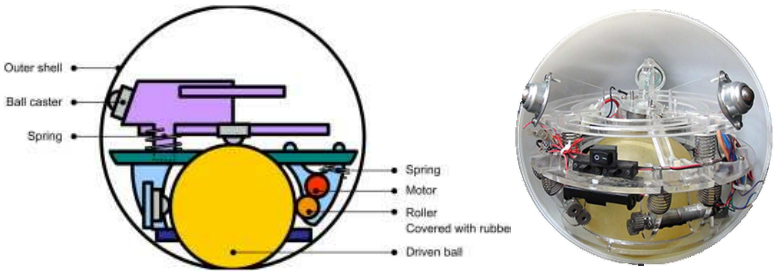

Figure 7.21: CAD model and Prototype of OmniQiu [41].

Spherical mobile robot from University of Coimbra Designed by Alves and Diaz in 2002 at the University of Coimbra [4] with the purpose of carrying sensing devices or actuators in harsh environments, this four-wheeled hamster mechanism was chosen based on the solution adopted by Halme et al. in their research on spherical robots back in 1996 [61, 62]. The driving mechanism incorporates modified radiocontrolled servos for continuous rotation. A closed loop control system under a digital PLD approach was incorporated using a three-axis accelerometer, and a three-axis rate gyro for controlling the robot's acceleration, velocity, and position relative to the inertial reference frame. Likewise, each wheel is controlled separately with different motion curves.

OmniQiu Developed by Chen et al., at the National Taiwan University [41] in 2013, this hamster-like mechanism design is similar to the traditional computer ball-mouse. The shell-sphere has 12.15 cm of diameter. The IDU main body is composed by a solid sphere covered with a rubber tube and a diameter of 6 cm. Three orthogonally-oriented ball casters of 5 mm in diamater are installed to adequately keep the IDU attached to the spherical shell as seen in Figure 7.21. The internal structure is made of acrylic and composed of three main rings. In the upper ring three supports are placed orthogonally where the ball casters are screwed. Two arms screwed to the second ring hold two rollers located in contact on top of the driven ball. A spring mechanism is mounted underneath the ball caster as well as beneath the second ring to improve the rolling behavior between the driven ball and the outer shell. Two spur-gear transmissions (ratio 1:1) are used between the roller and the small IG-12GM 01 DC motor with a planetary gearbox (ratio 64:1). A RF-based T2ER transmitter/receiver pair provides telecommunication between the robot and the remote operator, and six nickel–metal hydride (NiMH) AA batteries are used as power source [41]. The third and lower ring is where the entire structure is bolted and also prevents the driven ball to move out of its place.

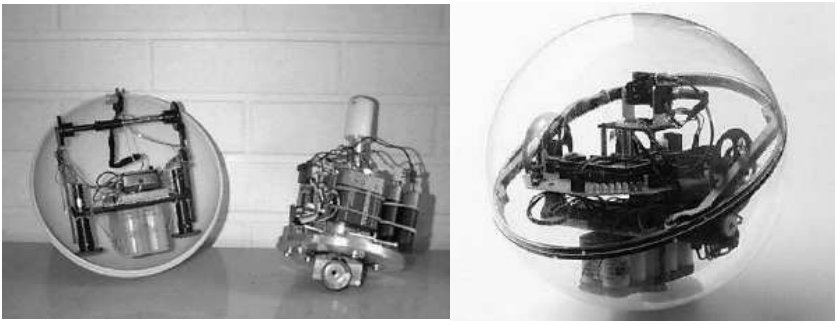

(a) **(b)**

Figure 7.22: Second and first prototypes of Rollo (left); Rollo third prototype (right) [144].

Rollo Designed to be a home-operations robot, Rollo is a 2-DoF mobile spherical robot intended to operate as a rolling telephone, calendar-event reminder, and safety guard. TKK built the first Rollo prototype using the sprung central member design, and the second prototype used a combination of the internal wheeled and sprung central member mechanisms, as shown in Figure 7.22a. Both approaches were rejected mainly for the requirement of a spherical shell to be very rigid and uniform. Then the third generation of Rollo was built using the pendulum mechanism [135], with the rotational rim gear carrying a rolling axis, and the instruments suspended on the latter, as shown in Figure 7.22b [144]. All three approaches were provided with full steerability easy to control. The system is equipped camera, microphone, and video link, but also incorporates sensors for temperature, pan, tilt, and heading of the inner mechanics and pulse encoders for motor-rotation measurement. A radio modem allows communication between Rollo and the control station. The robot is equipped with a Phytec MiniModul-167 microcontroller board using a Siemens SAB C167 CR-LM micro controller [144].

Spherical rolling robot with internal two-wheel cart Designed by Szymon Firlej at the AGH University of Science and Technology in Krakow, Poland (cf. Figure 7.23a) [54]. This approach consists of a two-wheel cart with central sprung hamster mechanism mounted on a rectangular PCB board, where the control processing unit, control systems, batteries and two Pololu HP 50:1 DC motors with 15 mm diameter wheels and rubber tires mounted at the sides, are located. The sprung central member, which consists of a threaded rod of 6 mm diameter used as a shaft, connects the aluminum roller on top with the PCB board, it has 2-DoF rolling freely in the internal surface of the spherical shell, and the spring in the center keeps both elements in balance guaranteeing that the roller and robot's wheels never loose contact with the interior

(a)

(b)

Figure 7.23: (Left) Firlej's spherical robot prototype [54]. (Right) SAR internal structure [129].

surface of the 18 cm diameter acrylic sphere [54].

Spherical Autonomic Robot (SAR) Developed in 2006 by the Israeli youtuber "rusil" [129], this spherical robot was built using an internal car with 3 holonomic Swedish wheels in a triangular configuration that allows the internal car to move the sphere in omnidirectional motion. As seen in the video from YouTube, the wheeled mechanism also incorporates an arm with a small supporting wheel (similar to BHQ-3) to prevent the latitudinal slipping, placed under a circular plaque with the driving motors. Figure 7.23b shows that any science sensor or payload can be placed on top of the circular plaque.

Solar Powered Miniball Wannabe Designed by the team behind the YouTbe channel Solarbotics [140] for hobbyists and kids getting initiated into Robotics, this solar powered rolling robot uses the sprung central member locomotion mechanism (cf. Figures 7.24a and 7.24b). It is composed of a spheric shell of 8 cm in diameter, one high-efficiency coreless motor, one motor mounting clip, three rubber wheels on nylon hubs, and two paper clips acting like a shaft for the wheels. Breadboard wire is used to make a guide for the wheels, preventing them from sliding too far. The energy is provided by a 37 mm × 33 mm solar cell, and stored in a 0.35 F 2.5 V capacitor [48]. Since this miniball rover does not include control unit and communications radio control, its entire locomotion and steerability cannot be remotely controlled by an human operator. However, this concept is very useful for getting non-robotics related people into the topic of rolling robots.

Conclusions IDU An internal drive unit allows for smooth operation on even terrain. The main downfall of this approach is the required friction of the drive unit inside the sphere. With a wheeled mechanism inside the sphere slippage of the wheel disables movement of the sphere.

(a)

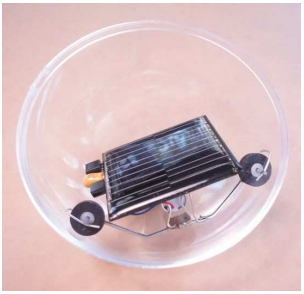

(b)

Figure 7.24: Solar Powered Miniball prototype [140].

Obstacles on the way require even higher friction inside. The lower gravity on the moon worsens this problem. Since the drive unit is not fixed to the sphere there is a high risk of failure without the ability to recover, in case the sphere ever looses control, e.g., rolls down a slope. A configuration with a sprung member is less fragile. Howeverm the more sturdy the construction to hold the drive unit in place is, the more space will be occupied within the shell, leaving less space for the sensor payload. The slippage problem persists also in this szenario.

Reaction wheels

A popular technique to change the orientation and attitude of satellites is the use of reaction wheels. The underlying principle for motion is the conservation of angular momentum. By spinning masses connected to motors around an axis with a high speed, the conservation of angular momentum can be used to control the motion and direction of the spherical robot. A collaborator in the Daedalus project, the University of Würzburg, has developed a spherical robot that uses this drivetrain system (refer Section 3.1.2). It was concluded that the use of flywheels leads to shaky and imprecise movement. It also used too much power to achieve motion. This technique was therefore not further considered.

BYQ-III BYQ-III is a spherical mobile robot equipped with a gyroscope designed by Liu et al., [90] at the Beijing University of Aeronautics and Astronautics in 2008, and based on a previous theoretical work by Hanxu et al. [64] on the same type of mechanisms for a nonholonomical robot. BYQ-III has a weight of 25 kg, and is composed of a counterweight pendulum, a gyro case and a spherical body of 60 cm in diameter with 10 mm wall thickness. The robot is remotely tele-operated by a joystick through a 4-channel 72.870 MHz radio control system, a 48 V nickel hydrid battery provides power for 10 hours to BYQ-III. Computing is performed on board by

Figure 7.25: Prototype of the spherical robot BYQ-III [90].

a 16 MHz microprocessor. The internal structure is composed of a gyro, which is linked to the outer shell by the driving motor that generates the torque about the lateral rotation axis of the gyro case. The system direction is changed by two sets of DC motors and gears. The steer motor, located at the longitudinal axis of the gyro case, generates the leaning torque about the longitudinal rotation axis [90]. The 3DM-GX1 IMU mounted on the gyro case, provides Kalman-filtered pitch, roll and yaw angles rating with respect to gravity. Both the IMU and encoders provide all data required for full-state feedback control.

7.2.2 Extended models of spherical-shaped robots

Differential drive system

When using a differential drive system, the robot is divided into three parts. Two semi-hemispheres that are connected to two individually driven electric motors and an internal corpus that inhabits the scientific equipment [43]. The robot moves by controlling each of the semi-hemispheres individually, which enables it to move into any direction with a zero-turn radius and thus making it a holonomic system. Besides its stability and high maneuverability, the robot's internal sphere will have more space for the required technology. Considering it needs only two motors to propel the robot, the space savings are incomparable to the previously discussed methods. Raura (2016) has developed a differential driven spherical robot for planetary exploration [122]. They implemented a differential drive system for precise control and maneuverability. Figure 7.26 shows the design of the developed robot. In order for the robot to overcome small obstacles and gaps, the robot was equipped with a hopping mechanism that enabled the robot to jump. Furthermore, Raura (2016) investigated the actual performance of

Figure 7.26: A differential driven robot developed with two individually operated wheels [122].

the robot under simulated lunar gravity and provided information about the power consumption of the electric motors.

While motion and jumping has been tested separately, Raura (2016) did not mention whether the robot was able to locomote immediately after a jump. Figure 7.26 indicates that the robot might not be able to land properly on its wheels or tilt over after landing. There is no information about flying or landing characteristics. Furthermore, the shape of the robot seemed to be susceptible to small obstacles. Even though Raura (2016) specifically indicated that the hopping systems purpose is to overcome obstacles, in a rocky environment like the moon, the sphere needs to be able to roll over small stones as well. The shape of the sphere however suggests that a small rock under one side of the wheel might tip the robot over.

The drivetrain system presented in this paper offers a high degree of mobility that the previously mentioned techniques lack. It offers an insight into a hybrid locomotion technique by utilising a rolling and jumping system. Since the robot has been specifically designed for lunar environments and tested under artificial lunar gravity, the paper serves as an inspiration and basis for the developed prototype presented in Section 3.1.1.

Deformable shell

A further type of related robots uses deformation of the shell to initialize rotation. Therefore, the robot's outer shell is divided into soccer ball like pentagonal sections, which can be pressurised to deform the shell and achieve motion as shown in Figure 7.27a [154]. Another idea is to construct a sphere consisting of four dielectric elastomer actuators [11]. By applying an electric field, the shell will deform and cause rotation.

NASA JPL TUMBLEWEED As Mars exploration rover developed in 2004 by the Jet Propulsion Laboratory (JPL) based on concepts going back to the 1970's [108], the Tumbleweed rover is a large, windblown, 1.5 m inflated ball, which carries a payload-tube in its rolling axis [15] as shown in Figure 7.27b. The ambient air is drawn inward by a pump through the ends of the

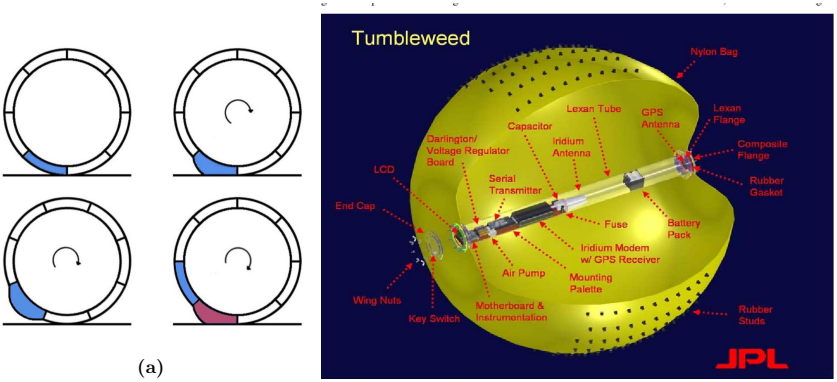

(a) (b)

Figure 7.27: (Left) A spherically shaped robot that achieves motion by deforming the outer shell [154]. (Right) Tumbleweed Rover developed at JPL [14].

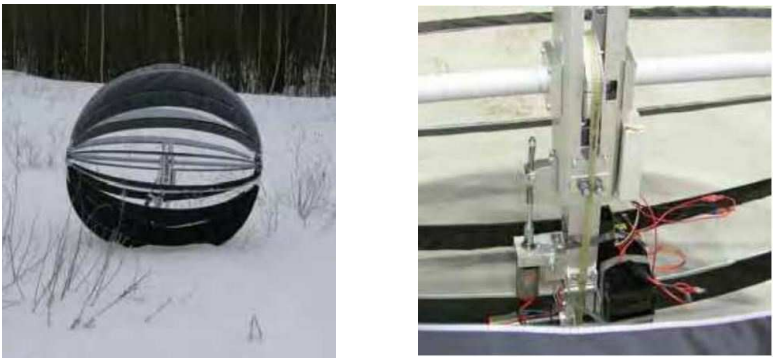

(a) (b)

Figure 7.28: Thistle prototype and the motion mechanism [158].

tube, where the instruments inside the latter measure ambient air composition and temperature. The robot movement is entirely dependant on the wind, however it also has the ability to control the speed by regulating its internal pressure. The robot also keeps track of its path incorporating a GPS that communicates with a stationary ground station [86].

Thistle Rover This research project was developed by Ylikorpi et al. [158] under the ARIADNA-program funded by the European Space Agency at the Helsinki University of Technology in 2004. Inspired by the Russian Thistle plant, and partially based on the Tumbleweed rover, this low-mass wind-propelled 1.3 m diameter spherical-shaped robot with structural flexibility and sectional circumference making the ball proceed in short bursts with the intention to operate on the surface of Mars for autonomous surface exploration [144]. Since the robot must keep moving ideally even without windy conditions, the team equipped the robot with a 2-DoF motorized 5.1 kg ballast mass that provides full steerability and motorized locomotion, rolling over 4.3 cm obstacles [158]. As shown in figure 7.28a, the driving and steering mechanism is composed by the battery and the two motors all mounted on a pendulum-like lever hanging from bearings on the central rolling axis of Thistle. The drive motor rotates the pendulum using a tooth belt and a sprocket wheel, the angle of the lever is adjusted by the tilting motor with the aid of a lead screw, the entire driving mechanism is controlled with a radio control system [158, 159].

Rollbot Designed in 2007 at the Centre for Biomimetic and Natural Technologies of the Department of Mechanical Engineering at the University of Bath in the UK by Armour et al., [10], this spherical robot can roll in any direction and jump to overcome obstacles by releasing the energy stored in the spring-hoops that composed the main spherical skeletal structure, compressing them along the central axis then launching and jumping making up the outer rolling surface. The jump direction is achieved by adjusting the centre of gravity of the device slightly leaning the axis over before launch. Similarly, by orienting the central axis parallel to the ground, adjusting the centre of gravity of the sphere, rolling motion is achieved. A 4.8 V 600 mAh battery pack supplies energy to two 4.8 V servos and to a radio control receiver. The servos have been modified for allowing continuous rotation. As seen in Figure 7.29a, the compression mechanism is a servo located at the top of the robot, rotating a continuously variable length crank connected directly to the bottom of the spherical skeletal structure. As the servo rotates, the top and bottom are pulled together storing energy in the spring-hoops [10]. A later version of Jollbot is also able to carry a payload of 250 grams [84].

Hex-A-Ball (HAB) Designed by Phipps and Minor [119] and inspired by the Namibia Desert Wheeling spider, HAB is a hybrid rolling-walking robot with a spherical exoskeleton where the bottom hemisphere, mounted on a ring-like plaque, is composed of six synchronized shell-leg sections. The top hemisphere encapsulates the science sensors, as shown in Figure 7.30. All internal components, shell-legs, and the top shell are attached to the ring-plaque. This design approach provides different motion modes as it can adapt itself to different terrains and inclinations where a completely spherical configuration could not [119], allowing it to perform tasks on greater slopes. Each leg locomotion is provided by a geared DC motor attached alongside two batteries to the shell-leg for increasing the mass of the latter, providing an appreciable mass

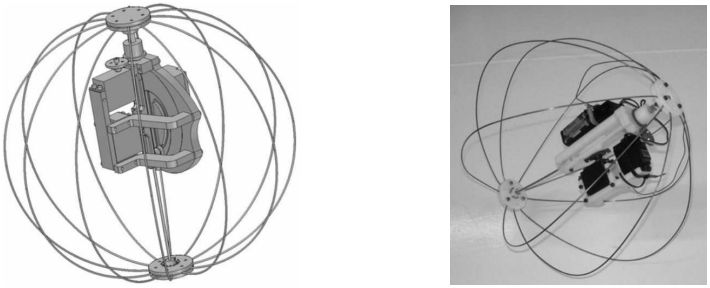

(a) (b)

Figure 7.29: CAD model and Prototype of Jollbot [10].

Figure 7.30: Hybrid Hex-A-Ball spherical robot with walking and climbing locomotion [119].

moment to the legs for controlling rolling locomotion, the motor drives a self-locking single-lead worm-gear, which allows the motor to be mounted perpendicular to the turning axis. Likewise, the worm gearing is coupled by chain drive to the turning axis, providing additional reduction and allowing the motor to be mounted near the tip of the leg while not interfering with other components [119]. Maximum velocity is achieved during the rolling mode. On the other hand, for reaching maximum stability during the walking mode, either the "even legs" (Set 1) or the "odd legs" (Set 2) are always in contact with the ground.

MorpHex Designed and created in 2012 by Norwegian hobbyist Kåre Halvorsen, similar to the configuration of Hex-a-ball [119], this robot is a combination of a spherical robot with a hexapod integrating six legs in each hemisphere (twelve synchronized shell sections in total) extending them when needed to deal with difficult terrain. MorpHex can roll with omnidirectional motion but also transform from sphere to a hexapod and vice versa [63]. High accuracy is achievable

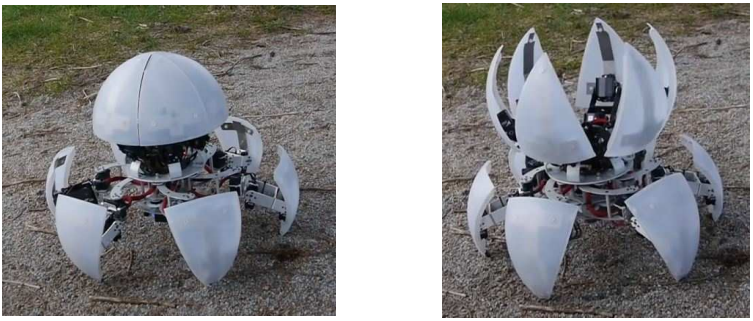

(a) **(b)**

Figure 7.31: MorpHex prototype with shell fully deployed on both hemispheres [63]

using a SparkFun inertial measurement unit (IMU), then the robot can gauge orientation and speed, stabilizing and controlling its rolling motion [142]. MorPhex locomotion is entirely similar to HAB, three legs either Set 1 or Set 2 are always in contact with the ground. To move forward the robot lifts Set 1 using turning actuation, then propels itself forward using gaiting actuation of Set 2 while Set 1 simultaneously rotates in the opposite direction, then lowers Set 1 and raises Set 2, moving itself forward with Set 1. The process continues until the controller decides to change otherwise, and maximum velocity is achieved during the rolling mode [119].

Hopping Rover Design for Magnetometer A hopping rover designed was proposed by Lopez-Arreguin et al., in 2019 as a cooperation between the University of Würzburg and the Technical University of Braunschweig [94], and inspired in the mission of MASCOT, the lander built by the German Aerospace Center launched on-board the Japanese Hayabusa2 spacecraft in 2014. The mission of this spherical magnetometer is to measure the lunar magnetic field near the landing zone of Apollo XVII. The simultaneous measurements of radial components in at least two locations will allow calculating the external driving field without requiring data from a lunar orbiting satellite. The concept design for this lunar rolling robot is to fit all MASCOT'S scientific instruments, including magnetometer Micro-Omega, GNC sensors, solar arrays and antennas adopting similar positions and distribution as in MASCOT, into a spherical body of 20 cm in diameter, improving mobility and the travel distance. For reference, MASCOT had a size of 30 cm × 30 cm × 20 cm. The locomotion mechanisms will be replaced by three reaction wheels, controlling the three axis (roll, yaw, pitch). Lab experiments showed that a Kalman filter with non-linear controller type (SDRE), in a low power consumption board (Arduino MEGA), has great accuracy in the pointing accuracy with the reaction wheels. Finally, a second design

(a) (b)

Figure 7.32: Hopping rover design concept from University of Würzburg [94].

approach has been also considered since the first iteration had difficulty to carve spherical surfaces, as shown in Figure 7.32b [94].

Sea-urchin type robot [112]

This is a basic model of spherical robots propelled by an inner pendulum, with the purpose to overcome the physical constraint of basic spherical robots to surpass obstacles and hollows of more than 1/10th of their diameter, proposing an extension inspired by the shell of sea urchins. In this extension, a basic pendulum-based spherical robot was circumscribed within a bigger sphere. The former is referred to as endoskeleton and the latter to as exoskeleton. The role of the exoskeleton is to shelter the set of modifications needed for this extension, namely for new actuators. Actuators are retractable or telescopic antennas, each one activated by one motor, that have a full length equivalent to the double of the radius of the endoskeleton. Actuators represent the spines of the sea urchin and can be used for a better leverage. These actuators are uniformly distributed over the surface of the exoesqueleton, using the algorithm suggested by Edward Saff and Arno Kuijlaars in their research from 1997 [130].

7.2.3 Conclusions about the drivetrain system

The ability to operate in an environment like the moon requires a very high degree of mobility and maneuverability. The specific characteristics of the moon surface, however, require also a high degree of protection against dust. The goal is therefore, to have all sensors and the actuators comprised within the protective shell of the sphere. Table 7.2 summarises advantages and disadvantages of the various locomotion options. The mission's proposal outlines the use of scientific equipment like laser scanners and cameras that need a transparent sphere for functioning. A shell transformation technique complexifies making the sphere perfectly transparent.

Table 7.2: Advantages and disadvantages of drivetrain systems for spherical robots in relation to the mission's goals.

Drivetrain system	Advantages	Disadvantages
Pendulum	Sealed internal body	Limited torque
		Imprecise movement
		Not space efficient
Internal Drive Unit (IDU)	Sealed internal body	High friction between wheel and shell
	Holonomic system	Imprecise movement
		Not space efficient
Differential drive system	Precise maneuverability	Apertures for motor shaft (no sealed shell)
	Space efficient	Two ground contact points
	Holonomic system	

Even though the deformation of the shell enables the robot to overcome obstacles, small lunar dust particles can get into the mechanism during the deformation process. Therefore, this type of drivetrain system has not been further investigated.

Due to the inability to overcome obstacles and the lack of stability an internal drive unit has been considered as inappropriate for the mission goal. Also during descent, the instability of the drive unit inside the sphere might cause problems. A further limiting factor is the required space inside the sphere.

As elaborated above, the differential drive train system offers the precision that is needed for the lunar surface. Contrary to the pendulum drive where the amount of torque is limited, a differential drive system can use any type of motor and torque. Additionally, a pendulum driven robot takes up more than half the space inside the robot, while a differential drive consists of merely two motors propelling the left and right hemisphere. It is important to note that by utilising a differential drive system the shell of the sphere needs to have apertures for the motor shafts thus breaking the sealed environment.

Although a high degree of precision in mobility and manoeuvrability is certainly a goal to strive for, a self-contained robot that can move without any apertures with the external world is a very important asset, considering the harsh terrain of the Moon. The added challenges in the control of a pendulum-based robots are balanced by the unique advantage of a completely sealed internal body, and therefore makes this type of robotic system the primary goal of our exploration.

Chapter 8

Conclusion

The Daedalus OSIP study has shown, that a spherical robot is well-suited for lunar exploration and that this robot type should further be studied. Indeed, the close work with geologists and field experts together with the landing site characterization gave the possibility to better constrain both the locomotion and the scientific payload. The study shows that the robot can be used for many firsts in lunar science and exploration. We have identified and parameterized the external interfaces in OCDT to achieve full compliance, and we believe that such synergy between science and technology will benefit from a CDF study and further developments.

Appendix A

Thermal Simulation

```python
import numpy as np
import matplotlib.pyplot as plt

#################### Define Constants ########################
SPHERE_WEIGHT = 20e3  # g
# All in Watt
POWER_COMPONENTS_SPHERE = [2 * 1.0,  # Two Microcontrollers
                           3 * 0.33,  # Three IMUs
                           2 * 30,  # Two Lidars
                           4 * 4,  # 4 Optical Sensors
                           1 * 5,  # Switch
                           # 2 * 100  # Motor
                           ]
POWER_EXERTED_SPHERE = np.sum(POWER_COMPONENTS_SPHERE)


POWER_COMPONENTS_CABLE = [2 * 1.0,  # Two Microcontrollers
                          1 * 5  # Loss of Voltage stabilizer
                          ]
POWER_EXERTED_CABLE = np.sum(POWER_COMPONENTS_CABLE)

TEMP_RANGE = np.arange(100.0, 401.0, 50)  # 100 K to 400 K

OPERATING_RANGE = [253.15, 333.15]  # -20C -> 60C
# 10 minutes to 60 minutes in seconds
TIME_RANGE = np.arange(10.0 * 60, 130.0 * 60, 10.0 * 60)


STEFAN_BOLTZMANN_CONSTANT = 5.6704e-8  # W/m^2K^4
HEAT_CAPACITY_AL = 0.91  # J/g K
HEAT_CAPACITY_GLASS = 0.840  # J/g K
EMISSIVITY_GLASS = 0.91
EMISSIVITY_AL = 0.03  # Aluminum Foil
# https://www2.physics.ox.ac.uk/sites/default/
# files/2012-03-08/2_thomas_pdf_10647.pdf
EMISSIVITY_REGOLITH = 0.9
SURFACE_AREA = 4 * np.pi * 0.29 ** 2  # m^2
```

```

TIME_STEP = 0.01  # s
START_TEMP = 273.15  # K = 0C

######################## Simulate Temperature ################
data = open("required_heat.txt", 'w')
data.write("\t\t & " + "{K} &".join(map(str, TEMP_RANGE)) + "\\\\\n")

# For all considered Durations
for i in range(len(TIME_RANGE)):
    temp_plot = plt.subplot(2, 1, 1)
    heat_plot = plt.subplot(2, 1, 2)
    data.write(f"\\unit[{TIME_RANGE[i]/60.0}]{{min}} & ")
    # For all considered Environment Temperatures
    for temp in range(len(TEMP_RANGE)):
        curr_temp = START_TEMP
        Q_heat = []
        temperatures = []
        time = np.arange(0, TIME_RANGE[i], TIME_STEP)

        # For every timestep within the duration
        for t in time:
            temperatures.append(curr_temp)
            # The heat radiated by the sphere towards the moon minus the
            # Generated heat by all components. In Watt
            Q_dot_lost = STEFAN_BOLTZMANN_CONSTANT * EMISSIVITY_GLASS *\
                EMISSIVITY_REGOLITH * SURFACE_AREA * \
                (curr_temp**4 - TEMP_RANGE[temp]**4) - POWER_EXERTED_SPHERE

            # The lost energy assuming constand Q_dot during a time step
            E_lost = Q_dot_lost * TIME_STEP

            curr_temp += - E_lost / (HEAT_CAPACITY_AL * SPHERE_WEIGHT)
            if curr_temp < OPERATING_RANGE[0] or curr_temp > OPERATING_RANGE[1]:
                Q_heat.append(Q_dot_lost)
                curr_temp += Q_dot_lost * TIME_STEP / \
                    (HEAT_CAPACITY_AL * SPHERE_WEIGHT)
            else:
                Q_heat.append(0.0)
        heat_plot.plot(time, Q_heat, label=f'{TEMP_RANGE[temp]} K')
        temp_plot.plot(time, temperatures, label=f'{TEMP_RANGE[temp]} K')
        data.write(
            f"\\unit[{np.sum(np.multiply(Q_heat,TIME_STEP))/60.0/60.0:.2f}]{{Wh}} &")

    data.write("\\\\\n")
    heat_plot.grid()
    heat_plot.set_ylabel("Heating Power [W]")
    heat_plot.set_xlabel("Time [s]")
    heat_plot.legend(loc="lower left")

    temp_plot.grid()
    temp_plot.set_ylabel("Temperature [K]")
    temp_plot.set_xlabel("Time [s]")
    temp_plot.plot(time, OPERATING_RANGE[0] *
```

```
92                  np.ones(len(time)), ls='--', color='grey')
93      temp_plot.plot(time, OPERATING_RANGE[1] *
94                  np.ones(len(time)), ls='--', color='grey')
95
96      plt.tight_layout()
97      plt.savefig(f"Thermal_Plot_{TIME_RANGE[i]/60.0}_Minutes.png", dpi=500)
98      plt.close()
```

Bibliography

[1] Nima Afshar-Mohajer, Chang-Yu Wu, Jennifer Sinclair Curtis, and James R. Gaier. Review of dust transport and mitigation technologies in lunar and Martian atmospheres. *Advances in Space Research*, 56(6):1222–1241, September 2015. 127

[2] Vahid Alizadehyazdi, Elizabeth McQueney, Koki Tanaka, and Matthew Spenko. Ultrasonic and electrostatic self-cleaning microstructured adhesives for robotic grippers. In *Proceedings of the IEEE/RSJ International Conference on Intelligent Robots and Systems (IROS '18)*, Madrid, Spain, October 2018. 83

[3] Vahid Alizadehyazdi, Mehdi Modabberifar, S. M. Javid Mahmoudzadeh Akherat, and Matthew Spenko. Electrostatic self-cleaning gecko-like adhesives. *Journal of The Royal Society Interface*, 15:20170714, 04 2018. 83

[4] J Alves and J Dias. Design and control of a spherical mobile robot. *Proceedings of the Institution of Mechanical Engineers, Part I: Journal of Systems and Control Engineering*, 217(6):457–467, 2003. 151, 153, 154

[5] M. Anand, I. A. Crawford, M. Balat-Pichelin, S. Abanades, W. van Westrenen, G. Péraudeau, R. Jaumann, and W. Seboldt. A brief review of chemical and mineralogical resources on the Moon and likely initial in situ resource utilization (ISRU) applications. *Planetary and Space Science*, 74(1):42–48, December 2012. 13

[6] J A Anderson, S C Sides, D L Soltesz, T L Sucharski, and K L Becker. Modernization of the integrated software for imagers and spectrometers. In *35 th Lunar and Planetary Science Conference; Abstracts of the Papers*, 2004. 26

[7] De Giovanni Angelis, J.W. Wilson, M.S. Clowdsley, J.E. Nealy, D.H. Humes, and J.M. Clem. Lunar Lava Tube Radiation Safety Analysis. *Journal of Radiation Research*, 43(Suppl):S41–S45, 12 2002. 19

[8] G De Angelis, J W Wilson, M S Clowdsley, J E Nealy, D Humes, and J M Clem. A RADIATION SAFETY ANALYSIS FOR LUNAR LAVA TUBES. *Journal of Radiation Research*, 43:2, 2002. 15, 16

[9] M. Aoyoma and S. Masuda. Characteristics of electric dust collector based on electric curtain. In *Proceedings of the General Conference of the Institute of Electronic Engineers in Japan*, number 821 in Proc. of Albany Conference on Electrostatics, 1971. 127

[10] Rhodri Armour, Keith Paskins, Adrian Bowyer, Julian Vincent, and William Megill. Jumping robots: a biomimetic solution to locomotion across rough terrain. *Bioinspiration & biomimetics*, 2(3):S65, 2007. 161, 162

[11] Matteo Artusi, Marco Potz, Jeydmer Aristizabal, Carlo Menon, Silvio Cocuzza, and Stefano Debei. Electroactive elastomeric actuators for the implementation of a deformable spherical rover. *IEEE/ASME Transactions on Mechatronics*, 16(1):50–57, 2011. 159

[12] J. Atkinson and K. Zacny. Mechanical Properties of Icy Lunar Regolith: Application to ISRU on the Moon and Mars. In *Mechanical Properties of Icy Lunar Regolith: Application to ISRU on the Moon and Mars*, pages 109–120, November 2018. Publisher: American Society of Civil Engineers. 13

[13] A. Baumberg. Reliable Feature Matching Across Widely Separated Views. In *Proceedings of the IEEE Computer Society Conference on Computer Vision and Pattern Recognition*, volume 1, 09 2001. 80

[14] A. Behar, J. Matthews, F. Carsey, and J. Jones. Nasa/jpl tumbleweed polar rover. *2004 IEEE Aerospace Conference Proceedings (IEEE Cat. No.04TH8720)*, 1:–395 Vol.1, 2004. 160

[15] Alberto Behar, Jaret Matthews, Frank Carsey, and Jack Jones. Nasa/jpl tumbleweed polar rover. In *2004 IEEE Aerospace Conference Proceedings (IEEE Cat. No. 04TH8720)*, volume 1. IEEE, 2004. 159

[16] P. Besl and N. McKay. A method for Registration of 3-D Shapes. *IEEE Trans. Pattern Analysis and Machine Intelligence (PAMI)*, 14(2):239–256, 1992. 81

[17] S. Besse, J. Sunshine, M. Staid, J. Boardman, C. Pieters, P. Guasqui, E. Malaret, S. McLaughlin, Y. Yokota, and J.-Y. Li. A visible and near-infrared photometric correction for Moon Mineralogy Mapper (M3). *Icarus*, 222(1):229 – 242, 2013. 68

[18] S. Besse, J. M. Sunshine, M. I. Staid, N. E. Petro, J. W. Boardman, R. O. Green, J. W. Head, P. J. Isaacson, J. F. Mustard, and C. M. Pieters. Compositional variability of the Marius Hills volcanic complex from the Moon Mineralogy Mapper (M3). *Journal of Geophysical Research: Planets*, 116(E6), 2011. _eprint: https://agupubs.onlinelibrary.wiley.com/doi/pdf/10.1029/2010JE003725. 22, 70

[19] Ross A. Beyer, Oleg Alexandrov, and Scott McMichael. The Ames Stereo Pipeline: NASA's Open Source Software for Deriving and Processing Terrain Data. *Earth and Space Science*, 5(9):537–548, 2018. _eprint: https://agupubs.onlinelibrary.wiley.com/doi/pdf/10.1029/2018EA000409. 26, 27

[20] Antonio Bicchi, Andrea Balluchi, Domenico Prattichizzo, and Andrea Gorelli. Introducing the" sphericle": an experimental testbed for research and teaching in nonholonomy. In *Proceedings of International Conference on Robotics and Automation*, volume 3, pages 2620–2625. IEEE, 1997. 153

[21] Paul S. Blaer and Peter K. Allen. Data acquisition and view planning for 3-D modeling tasks. In *IEEE/RSJ International Conference on Intelligent Robots and Systems (IROS '07)*, pages 417–422, 2007. 61, 62

[22] David M. Blair, Loic Chappaz, Rohan Sood, Colleen Milbury, Antonio Bobet, H. Jay Melosh, Kathleen C. Howell, and Andrew M. Freed. The structural stability of lunar lava tubes. *Icarus*, 282:47–55, January 2017. 13

[23] David M. Blair, Loic Chappaz, Rohan Sood, Colleen Milbury, Antonio Bobet, H. Jay Melosh, Kathleen C. Howell, and Andrew M. Freed. The structural stability of lunar lava tubes. *Icarus*, 282:47–55, 2017. 18

[24] Haleh Boostani and Sama Modirrousta. Review of nanocoatings for building application. *Procedia Engineering*, 145:1541–1548, 12 2016. 83

[25] D. Borrmann, J. Elseberg, K. Lingemann, A. Nüchter, and J. Hertzberg. Globally consistent 3d mapping with scan matching. *Journal Robotics and Autonomous Systems (JRAS)*, 56(2):130–142, February 2008. 82

[26] D. Borrmann, A. Nüchter, M. Dakulović, I. Maurović, I. Petrović, D. Osmanković, and J. Velagić. A mobile robot based system for fully automated thermal 3d mapping. *Journal Advanced Engineering Informatics (JAdvEI)*, 28(4):425–440, October 2014. 60, 62, 63

[27] Michael Bosse and Robert Zlot. Continuous 3D Scan-Matching with a Spinning 2D Laser. In *Proceedings of the IEEE International Conference on Robotics and Automation (ICRA '09)*, pages 4312–4319, May 2009. 82

[28] Peter A. Burrough, Rachael McDonnell, Rachael A. McDonnell, and Christopher D. Lloyd. *Principles of Geographical Information Systems*. OUP Oxford, 2015. Google-Books-ID: kvoJCAAAQBAJ. 29

[29] D. Ben J. Bussey, Paul D. Spudis, and Mark S. Robinson. Illumination conditions at the lunar South Pole. *Geophysical Research Letters*, 26(9):1187–1190, 1999. _eprint: https://agupubs.onlinelibrary.wiley.com/doi/pdf/10.1029/1999GL900213. 13, 16

[30] Yao Cai, Qiang Zhan, and Xi Xi. Neural network control for the linear motion of a spherical mobile robot. *International Journal of Advanced Robotic Systems*, 8(4):32, 2011. 147

[31] C. I. Calle, C. R. Buhler, M. R. Johansen, M. D. Hogue, and S. J. Snyder. Active dust control and mitigation technology for lunar and Martian exploration. *Acta Astronautica*, 69(11):1082–1088, December 2011. 127

[32] C. I. Calle, C. R. Buhler, J. L. McFall, and S. J. Snyder. Particle removal by electrostatic and dielectrophoretic forces for dust control during lunar exploration missions. *Journal of Electrostatics*, 67(2):89–92, May 2009. 127

[33] Sonia Calvari and Harry Pinkerton. Formation of lava tubes and extensive flow field during the 1991–1993 eruption of Mount Etna. *Journal of Geophysical Research: Solid Earth*, 103(B11):27291–27301, 1998. _eprint: https://agupubs.onlinelibrary.wiley.com/doi/pdf/10.1029/97JB03388. 13

[34] Leandro Cancar, David Sanz, Juan D Hernández, Jaime del Cerro, and Antonio Barrientos. Precision humidity and temperature measuring in farming using newer ground mobile robots. In *ROBOT2013: First Iberian Robotics Conference*, pages 443–456. Springer, 2014. 37, 138

[35] David Carabis. The design of a maneuverable rolling robot. B.S. honor thesis, Union College, 2013. 143, 144, 145

[36] Loic Chappaz, Rohan Sood, Henry J. Melosh, Kathleen C. Howell, David M. Blair, Colleen Milbury, and Maria T. Zuber. Evidence of large empty lava tubes on the Moon using GRAIL gravity. *Geophysical Research Letters*, 44(1):105–112, 2017. _eprint: https://agupubs.onlinelibrary.wiley.com/doi/pdf/10.1002/2016GL071588. 13

[37] Loic Chappaz, Rohan Sood, Henry J. Melosh, Kathleen C. Howell, David M. Blair, Colleen Milbury, and Maria T. Zuber. Evidence of large empty lava tubes on the moon using grail gravity. *Geophysical Research Letters*, 44(1), 2017. 18

[38] A. Chase, R.; Pandya. *A Review of Active Mechanical Driving Principles of Spherical Robots*. Robotics 2012, 1, 3-23. 137

[39] Richard Chase and Abhilash Pandya. A review of active mechanical driving principles of spherical robots. *Robotics*, 1(1):3–23, 2012. 137, 138, 139, 150

[40] Brian Chemel, Edward Mutschler, and Hagen Schempf. Cyclops: Miniature robotic reconnaissance system. In *Proceedings 1999 IEEE International Conference on Robotics and Automation (Cat. No. 99CH36288C)*, volume 3, pages 2298–2302. IEEE, 1999. 140

[41] Wei-Hsi Chen, Ching-Pei Chen, Jia-Shiuan Tsai, Jackie Yang, and Pei-Chun Lin. Design and implementation of a ball-driven omnidirectional spherical robot. *Mechanism and Machine Theory*, 68:35–48, 2013. 154

[42] R. N. Clark. Chapter 1: Spectroscopy of rocks and minerals, and principles of spectroscopy. In A.N. Rencz, editor, *Manual of Remote Sensing*, volume 3 of *Remote Sensing for the Earth Sciences*, pages 3– 58. John Wiley and Sons, New York, 1999. 71

[43] Vincent A Crossley. A literature review on the design of spherical rolling robots. *Pittsburgh, Pa*, pages 1–6, 2006. 158

[44] D. P. Cruikshank and C. A. Wood. Lunar rilles and Hawaiian volcanic features: Possible analogues. *The Moon*, 3(4):412–447, March 1972. 15

[45] D. P. Cruikshank and C. A. Wood. Lunar rilles and hawaiian volcanic features: Possible analogues. *The moon*, pages 412–447, 1972. 18

[46] T. A. Davis. Algorithm 849: A Concise Sparse Cholesky Factorization Package. *ACM Trans. Math. Softw.*, 31(4):587–591, 2005. 82

[47] D. N. DellaGiustina, J. P. Emery, D. R. Golish, B. Rozitis, C. A. Bennett, K. N. Burke, R.-L. Ballouz, K. J. Becker, P. R. Christensen, C. Y. Drouet d'Aubigny, V. E. Hamilton, D. C. Reuter, B. Rizk, A. A. Simon, E. Asphaug, J. L. Bandfield, O. S. Barnouin, M. A. Barucci, E. B. Bierhaus, R. P. Binzel, W. F. Bottke, N. E. Bowles, H. Campins, B. C. Clark, B. E. Clark, H. C. Connolly, M. G. Daly, J. de Leon, M. Delbo', J. D. P. Deshapriya, C. M. Elder, S. Fornasier, C. W. Hergenrother, E. S. Howell, E. R. Jawin, H. H. Kaplan, T. R. Kareta, L. Le Corre, J.-Y. Li, J. Licandro, L. F. Lim, P. Michel, J. Molaro, M. C. Nolan, M. Pajola, M. Popescu, J. L. Rizos Garcia, A. Ryan, S. R. Schwartz, N. Shultz, M. A. Siegler, P. H. Smith, E. Tatsumi, C. A. Thomas, K. J. Walsh, C. W. V. Wolner, X.-D. Zou, and D. S. Lauretta. Properties of rubble-pile asteroid (101955) Bennu from OSIRIS-REx imaging and thermal analysis. *Nature Astronomy*, 3(4):341–351, April 2019. Number: 4 Publisher: Nature Publishing Group. 32

[48] Jerome Demers. Solar powered miniball wannabe, Nov 2017. 156

[49] R. Deriche, Z. Zhang, Q. Luong, and O. Faugeras. *Robust recovery of the epipolar geometry for an uncalibrated stereo rig*, pages 567–576. Springer Berlin Heidelberg, Berlin, Heidelberg, 1994. 80

[50] E. Digor, A. Birk, and A. Nüchter. Exploration strategies for a robot with a continously rotating 3d scanner. In *Proceedings of the Second International Conference on Simulation, Modeling and Programming for Autonomous Robots (SIMPAR '10)*, volume 6472 of *Lecture Notes in Computer Science*, pages 374–386, Darmstadt, Germany, November 2010. 60

[51] Steven Dubowsky, Jean-Sébastien Plante, and Penny Boston. Low cost micro exploration robots for search and rescue in rough terrain. In *IEEE International Workshop on Safety, Security and Rescue Robotics, USA*, pages 25–30, 2006. 37

[52] A. Ekman, A. Torne, and D. Stromberg. Exploration of polygonal environments using range data. *Systems, Man, and Cybernetics, Part B: Cybernetics*, 27(2):250–255, 1997. 61

[53] J. Elseberg, D. Borrmann, and A. Nüchter. Algorithmic solutions for computing accurate maximum likelihood 3D point clouds from mobile laser scanning platforms. *Remote Sensing*, 5(11):5871–5906, November 2013. 82

[54] Szymon Firlej. Design, construction and control of a spherical rolling robot with internal two-wheel cart. *Automatyka/Automatics*, 19(2), 2015. 155, 156

[55] Marco Franceschi, Giordano Teza, Nereo Preto, Arianna Pesci, Antonio Galgaro, and Stefano Girardi. Discrimination between marls and limestones using intensity data from terrestrial laser scanner. *ISPRS Journal of Photogrammetry and Remote Sensing*, 64(6):522–528, November 2009. 71

[56] Randy Franck and Michael Renbarger. Cryogenic emissivity properties of ball infrared black. *AIP Conference Proceedings*, 1434(1):1497–1504, 2012. 98

[57] Golombek. Size-frequency distributions of rocks on the northern plains of Mars with special reference to Phoenix landing surfaces, 2008. 16

[58] M. P. Golombek, A. F. C. Haldemann, N. K. Forsberg-Taylor, E. N. DiMaggio, R. D. Schroeder, B. M. Jakosky, M. T. Mellon, and J. R. Matijevic. Rock size-frequency distributions on Mars and implications for Mars Exploration Rover landing safety and operations. *Journal of Geophysical Research: Planets*, 108(E12), 2003. _eprint: https://agupubs.onlinelibrary.wiley.com/doi/pdf/10.1029/2002JE002035. 16

[59] H. González-Baños and J. C. Latombe. A Randomized Art Gallery Algorithm for Sensor Placement. In *Proceedings of the Seventeenth Annual Symposium on Computational Geometry 8SCG ' 01)*, pages 232–240, 2001. 61

[60] John A. Grant, Matthew P. Golombek, Sharon A. Wilson, Kenneth A. Farley, Ken H. Williford, and Al Chen. The science process for selecting the landing site for the 2020 Mars rover. *Planetary and Space Science*, 164:106–126, December 2018. 16, 29

[61] Aarne Halme, Torsten Schonberg, and Yan Wang. Motion control of a spherical mobile robot. In *Proceedings of 4th IEEE International Workshop on Advanced Motion Control-AMC'96-MIE*, volume 1, pages 259–264. IEEE, 1996. 154

[62] Aarne Halme, Jussi Suomela, Torsten Schönberg, and Yan Wang. A spherical mobile micro-robot for scientific applications. *ASTRA*, 96, 1996. 154

[63] Kåre Halvorsen. Morphex, the incredible hexapod robot!, Apr 2014. 162, 163

[64] Sun Hanxu, Xiao Aiping, Jia Qingxuan, and Wang Liangqing. Omnidirectional kinematics analysis on bi-driver spherical robot. *Journal of Beijing University of Aeronautics and Astronautics*, 31(07):735, 2005. 157

[65] J. Haruyama, K. Hioki, Motomaro Shirao, T. Morota, H. Hiesinger, C. H. V. D. Bogert, H. Miyamoto, A. Iwasaki, Y. Yokota, M. Ohtake, T. Matsunaga, S. Hara, Shunsuke Nakanotani, and C. Pieters. Possible lunar lava tube skylight observed by selene cameras. *Geophysical Research Letters*, 36(17), 2009. 18, 22

[66] J. Haruyama, S. Sawai, T. Mizuno, T. Yoshimitsu, S. Fukuda, and I. Nakatani. Exploration of lunar holes, possible skylights of underlying lava tubes, by smart lander for investigating moon (slim). *Transactions of The Japan Society for Aeronautical and Space Sciences, Aerospace Technology Japan*, 10, 2012. 19

[67] Junichi Haruyama, Kazuyuki Hioki, Motomaro Shirao, Tomokatsu Morota, Harald Hiesinger, Carolyn H. van der Bogert, Hideaki Miyamoto, Akira Iwasaki, Yasuhiro Yokota, Makiko Ohtake, Tsuneo Matsunaga, Seiichi Hara, Shunsuke Nakanotani, and Carle M. Pieters. Possible lunar lava tube skylight observed by SELENE cameras. *Geophysical Research Letters*, 36(21), 2009. _eprint: https://agupubs.onlinelibrary.wiley.com/doi/pdf/10.1029/2009GL040635. 13

[68] Junichi Haruyama, Tomokatsu Morota, Shingo Kobayashi, Shujiro Sawai, Paul G. Lucey, Motomaro Shirao, and Masaki N. Nishino. Lunar Holes and Lava Tubes as Resources for Lunar Science and Exploration. In Viorel Badescu, editor, *Moon: Prospective Energy and Material Resources*, pages 139–163. Springer, Berlin, Heidelberg, 2012. 15

[69] David J. Heather, Sarah K. Dunkin, and Lionel Wilson. Volcanism on the Marius Hills plateau: Observational analyses using Clementine multispectral data. *Journal of Geophysical Research: Planets*, 108(E3), 2003. 70

[70] Juan D Hernández Vega, David Sanz Muñoz, Gonzalo R Rodríguez-Canosa, Jorge Barrientos, Jaime del Cerro, and Antonio Barrientos. Sensorized robotic sphere for large exterior critical infrastructures supervision. *Jorunal of Applied Remote Sensing*, 7(1), 2013. 138, 141

[71] J. Hertzberg, K. Lingemann, and A. Nüchter. *Mobile Roboter: Eine Einführung aus Sicht der Informatik*. eXamen.press. Springer, Heidelberg, Germany, 2012. 61

[72] P J Hickson. Lunar surface temperatures from Apollo 11 data. *Thermal Characteristics of the Moon*, 28:27, 1972. 13, 16

[73] A. P. Ingersoll, T. Svitek, and B. C. Murray. Stability of polar frosts in spherical bowl-shaped craters on the moon, mercury, and mars. *Icarus*, 100(1):40–47, 1992. 18

[74] Andrew P. Ingersoll, Tomas Svitek, and Bruce C. Murray. Stability of polar frosts in spherical bowl-shaped craters on the Moon, Mercury, and Mars. *Icarus*, 100(1):40–47, November 1992. 13

[75] Peter J. Isaacson, Amit BASU Sarbadhikari, Carlé M. Pieters, Rachel L. Klima, Takahiro Hiroi, Yang Liu, and Lawrence A. Taylor. The lunar rock and mineral characterization consortium: Deconstruction and integrated mineralogical, petrologic, and spectroscopic analyses of mare basalts. *Meteoritics & Planetary Science*, 46(2):228–251, 2011. 69, 70

[76] Hickson P. J. Lunar surface temperatures from apollo 11 data, filing case no. 340. Apollo 11 Technical Memorandum, 1970. 18

[77] D. G. Jones and J. Malik. A computational framework for determining stereo correspondence from a set of linear spatial filters. In *Computer Vision — ECCV'92: Second European Conference on Computer Vision Santa Margherita Ligure*, pages 395–410, Berlin, Heidelberg, 1992. Springer Berlin Heidelberg. 80

[78] S. Kaasalainen, H. Niittymaki, A. Krooks, K. Koch, H. Kaartinen, A. Vain, and H. Hyyppa. Effect of Target Moisture on Laser Scanner Intensity. *IEEE Transactions on Geoscience and Remote Sensing*, 48(4):2128–2136, April 2010. 72

[79] T. Kaku, J. Haruyama, W. Miyake, A. Kumamoto, K. Ishiyama, T. Nishibori, K. Yamamoto, Sarah T. Crites, T. Michikami, Y. Yokota, R. Sood, H. J. Melosh, L. Chappaz, and K. C. Howell. Detection of Intact Lava Tubes at Marius Hills on the Moon by SELENE (Kaguya) Lunar Radar Sounder. *Geophysical Research Letters*, 44(20):10,155–10,161, 2017. _eprint: https://agupubs.onlinelibrary.wiley.com/doi/pdf/10.1002/2017GL074998. 13

[80] T. Kaku, J. Haruyama, W. Miyake, A. Kumamoto, K. Ishiyama, T. Nishibori, K. Yamamoto, Sarah T. Crites, T. Michikami, Y. Yokota, R. Sood, H. J. Melosh, L. Chappaz, and K. C. Howell. Detection of intact lava tubes at marius hills on the moon by selene (kaguya) lunar radar sounder. *Geophysical Research Letters*, 44(20), 2017. 18

[81] Viktor Kaznov and Mattias Seeman. Outdoor navigation with a spherical amphibious robot. In *2010 IEEE/RSJ International Conference on Intelligent Robots and Systems*, pages 5113–5118. IEEE, 2010. 141, 142

[82] Stephan Kempe. Chapter 131 - volcanic rock caves. In William B. White, David C. Culver, and Tanja Pipan, editors, *Encyclopedia of Caves (Third Edition)*, pages 1118 – 1127. Academic Press, third edition edition, 2019. 16

[83] Stephan Kempe, Ingo Bauer, Peter Bosted, Don Coons, and Ric Elhard. Inflationary versus crusted-over roofs of pyroducts (lava tunnels). In *Proceedings 14th International Symposium on Vulcanospeleology*, August 2010. 13

[84] Ralf Simon King. State of the art in robotics and robotic actuation. In *BiLBIQ: A Biologically Inspired Robot with Walking and Rolling Locomotion*, pages 29–47. Springer, 2013. 161

[85] Raymond F. Kokaly, Roger N. Clark, Gregg A. Swayze, K. Eric Livo, Todd M. Hoefen, Neil C. Pearson, Richard A. Wise, William M. Benzel, Heather A. Lowers, Rhonda L. Driscoll, and Anna J. Klein. USGS Spectral Library Version 7. USGS Numbered Series 1035, U.S. Geological Survey, Reston, VA, 2017. IP-075936. 73, 75

[86] Kimberly R. Kuhlman, Alberto Behar, Jack Jones, Penelope Boston, Jeffrey Antol, Gregory Hajos, Warren Kelliher, Max Coleman, Ronald Crawford, Lynn Rothschild, Martin Buehler, Greg Bearman, and Daniel W. Wilson. *Tumbleweed: A New Paradigm for Surveying the Surface of Mars for In-situ Resources*, pages 401–429. Springer Berlin Heidelberg, Berlin, Heidelberg, 2009. 160

[87] LaserFocusWorld. Mechanical scanners: Risley prism scanners improve on gimbal/galvo alternatives. `https://www.laserfocusworld.com/optics/article/16550223/mechanical-scanners-risley-prism-scanners-improve-on-gimbalgalvo-alternatives`, October 2014. 46, 47

[88] Shuai Li, Paul G. Lucey, Ralph E. Milliken, Paul O. Hayne, Elizabeth Fisher, Jean-Pierre Williams, Dana M. Hurley, and Richard C. Elphic. Direct evidence of surface exposed water ice in the lunar polar regions. *Proceedings of the National Academy of Sciences*, 115(36):8907–8912, September 2018. Publisher: National Academy of Sciences Section: Physical Sciences. 13

[89] T. Lindeberg and J. Gårding. Shape-adapted smoothing in estimation of 3-D shape cues from affine deformations of local 2-D brightness structure. *Image Vision Comput.*, 15:415–434, 1997. 80

[90] Daliang Liu, Hanxv Sun, Qingxuan Jia, and Liangqing Wang. Motion control of a spherical mobile robot by feedback linearization. In *2008 7th World Congress on Intelligent Control and Automation*, pages 965–970. IEEE, 2008. 157, 158

[91] Zheng Liu, Fu Zhang, and Xiaoping Hong. Low-cost retina-like robotic lidars based on incommensurable scanning. *Computing Research Repository (CoRR) in arxiv*, abs/2006.11034, 2020. 46, 47

[92] Carlos Lledo Ardila. Study and validation of a 5.8 ghz video-link for a lunar pico-rover. B.S. thesis, Universitat Politècnica de Catalunya, 2013. 142, 143

[93] H. C. Longuet-Higgins. A Computer Algorithm for Reconstructing a Scene from Two Projections. In Martin A. Fischler and Oscar Firschein, editors, *Readings in Computer Vision: Issues, Problems, Principles, and Paradigms*, pages 61–62. Morgan Kaufmann Publishers Inc., San Francisco, CA, USA, 1987. 81

[94] A.J.R Lopez-Arreguin, Sergio Montenegro, H. Hercik, and U. Auster. Magnetometry on the moon: towards a new program era of in-situ measurements. *Manuscript in preparation for Review in Physics*, 2019. 163, 164

[95] K.L. Low and A. Lastra. Efficient constraint evaluation algorithms for hierarchical next-best-view planning. In *Proceedings of the 3rd IEEE International Symposium on 3D Data Processing, Visualization, and Transmission*, pages 830–837, 2007. 61

[96] D.G. Lowe. Object recognition from local scale-invariant features. In *International Conference on Computer Vision, 1999*, pages 1150–1157. IEEE, 1999. 80

[97] Landgraf M., Carey W., Hipkin V., Carpenter J., and Hiesinger H. Heracles – exploring the moon in an international context. In *Europlanet Science Congress, EPSC Abstracts*, volume 12, 2018. 18, 22, 29

[98] P. C. Mahalanobis. On the generalised distance in statistics. In *Proceedings National Institute of Science, India*, volume 2, pages 49–55, April 1936. 80

[99] Saber Mahboubi, Mir Masoud Seyyed Fakhrabadi, and Ahmad Ghanbari. Design and implementation of a novel spherical mobile robot. *Journal of Intelligent & Robotic Systems*, 71(1):43–64, 2013. 148

[100] Alfred S. McEwen, Eric M. Eliason, James W. Bergstrom, Nathan T. Bridges, Candice J. Hansen, W. Alan Delamere, John A. Grant, Virginia C. Gulick, Kenneth E. Herkenhoff, Laszlo Keszthelyi, Randolph L. Kirk, Michael T. Mellon, Steven W. Squyres, Nicolas Thomas, and Catherine M. Weitz. Mars Reconnaissance Orbiter's High Resolution Imaging Science Experiment (HiRISE). *Journal of Geophysical Research: Planets*, 112(E5), 2007. eprint: https://agupubs.onlinelibrary.wiley.com/doi/pdf/10.1029/2005JE002605. 16

[101] Merck KGaA (Merck Group). https://www.merckgroup.com/en/products/pm/listing.html?tf=categories:areas_of_expertise(categories:areas_of_expertise/architecture),pm:application(pm:application/scratch-protection), 2020 (accessed: December 04, 2020). 83

[102] Francois Michaud and Serge Caron. Roball, the rolling robot. *Autonomous robots*, 12(2):211–222, 2002. 138, 139

[103] Francois Michaud, Jean de Lafontaine, and Serge Caron. A spherical robot for planetary surface exploration. In *Proceeding of the 6th International Symposium on Artificial Intelligence and Robotics & Automation in Space*, 2001. 138

[104] Tatsuhiro Michikami, Akiko M. Nakamura, Naru Hirata, Robert W. Gaskell, Ryosuke Nakamura, Takayuki Honda, Chikatoshi Honda, Kensuke Hiraoka, Jun Saito, Hirohide Demura, Masateru Ishiguro, and Hideaki Miyamoto. Size-frequency statistics of boulders on global surface of asteroid 25143 Itokawa. *Earth, Planets and Space*, 60(1):13–20, January 2008. 32

[105] S. Moazami, S. Palanki, and H. Zargarzadeh. Kinematics of norma, a spherical robot, rolling over 3d terrains. In *2019 American Control Conference (ACC)*, pages 1330–1335, 2019. 146

[106] Saeed Moazami, M Naddaf-Sh, Srinivas Palanki, Hassan Zargarzadeh, et al. Design, modeling, and control of norma: a slider & pendulum-driven spherical robot. *arXiv preprint arXiv:1908.02243*, 2019. 145

[107] S. J. Moorehead, R. Simmons, and W. L. Whittaker. Autonomous exploration using multiple sources of information. In *Proceedings of the IEEE International Conference on Robotics and Automation (ICRA '01)*, Seoul, Korea, May 2001. 61

[108] Jpl news – tumbleweed rover goes on a roll at south pole, 2004. 159

[109] A. Nüchter, J. Elseberg, P. Schneider, and D. Paulus. Study of Parameterizations for the Rigid Body Transformations of The Scan Registration Problem. *Journal Computer Vision and Image Understanding (CVIU)*, 114(8):963–980, August 2010. 82

[110] A. Nüchter, H. Surmann, and J. Hertzberg. Planning Robot Motion for 3D Digitalization of Indoor Environments. In *Proceedings of the 11th IEEE International Conference on Advanced Robotics (ICAR '03)*, pages 222–227, Coimbra, Portugal, June 2003. 60

[111] H. Nyquist. Certain Topics in Telegraph Transmission Theory. *Transactions of the American Institute of Electrical Engineers*, 47(2):617–644, April 1928. Conference Name: Transactions of the American Institute of Electrical Engineers. 32

[112] Jorge Ocampo-Jiménez, Angelica Muñoz-Meléndez, and Gustavo Rodríguez-Gómez. Enhanced locomotion of a spherical robot based on the sea-urchin characteristics. In Armin Duff, Nathan F. Lepora, Anna Mura, Tony J. Prescott, and Paul F. M. J. Verschure, editors, *Biomimetic and Biohybrid Systems*, pages 238–248, Cham, 2014. Springer International Publishing. 37, 138, 151, 164

[113] J. O'Rourke. *Art Gallery Theorems and Algorithms*. Internat. Series of Monographs on Computer Science. Oxford University Press, New York, NY, 1987. 61

[114] Maurizio Pajola, Riccardo Pozzobon, Alice Lucchetti, Sandro Rossato, Emanuele Baratti, Valentina Galluzzi, and Gabriele Cremonese. Abundance and size-frequency distribution of boulders in Linné crater's ejecta (Moon). *Planetary and Space Science*, 165:99–109, January 2019. 29

[115] Maurizio Pajola, Sandro Rossato, Emanuele Baratti, Riccardo Pozzobon, Cathy Quantin, John Carter, and Patrick Thollot. Boulder abundances and size-frequency distributions on Oxia Planum-Mars: Scientific implications for the 2020 ESA ExoMars rover. *Icarus*, 296:73–90, November 2017. 16, 32

[116] Maurizio Pajola, Sandro Rossato, John Carter, Emanuele Baratti, Riccardo Pozzobon, Marco Sergio Erculiani, Marcello Coradini, and Karen McBride. Eridania Basin: An ancient paleolake floor as the next landing site for the Mars 2020 rover. *Icarus*, 275:163–182, September 2016. 16

[117] Maurizio Pajola, Jean-Baptiste Vincent, Carsten Güttler, Jui-Chi Lee, Ivano Bertini, Matteo Massironi, Emanuele Simioni, Francesco Marzari, Lorenza Giacomini, Alice Lucchetti, Cesare Barbieri, Gabriele Cremonese, Giampiero Naletto, Antoine Pommerol, Mohamed R. El-Maarry, Sébastien Besse, Michael Küppers, Fiorangela La Forgia, Monica Lazzarin, Nicholas Thomas, Anne-Thérèse Auger, Holger Sierks, Philippe Lamy, Rafael Rodrigo, Detlef Koschny, Hans Rickman, Horst U. Keller, Jessica Agarwal, Michael F. A'Hearn, Maria A. Barucci, Jean-Loup Bertaux, Vania Da Deppo, Björn Davidsson, Mariolino De Cecco, Stefano Debei, Francesca Ferri, Sonia Fornasier, Marco Fulle, Olivier Groussin, Pedro J. Gutierrez, Stubbe F. Hviid, Wing-Huen Ip, Laurent Jorda, Jörg Knollenberg, J.-Rainer Kramm, Ekkehard Kürt, Luisa M. Lara, Zhong-Yi Lin, Jose J. Lopez Moreno, Sara Magrin, Simone Marchi, Harald Michalik, Richard Moissl, Stefano Mottola, Nilda Oklay, Frank Preusker, Frank Scholten, and Cecilia Tubiana. Size-frequency distribution of boulders $\geq$7 m on comet 67P/Churyumov-Gerasimenko. *Astronomy & Astrophysics*, 583:A37, November 2015. Publisher: EDP Sciences. 32

[118] Claudio Pernechele. Hyper hemispheric lens. *Optics Express*, 24(5):5014–5019, 2006. 53, 54, 56

[119] C. C. Phipps and M. Minor. Introducing the hex-a-ball, a hybrid locomotion terrain adaptive walking and rolling robot. In *CLAWAR*, pages 525–532. Springer, 2006. 161, 162, 163

[120] Deepak Pokhrel, Nutan Rajm Luitel, Sukanta Das, and Dip Narayan Ray. Design and development of a spherical robot (spherobot). In *Proceedings of the 1st International and 16th National Conference on Machines and Mechanisms (iNaCoMM2013), IIT Roorkee, India*, pages 735–741, 2013. 149

[121] Zhan Qiang, Liu Zengbo, and Cai Yao. A back-stepping based trajectory tracking controller for a non-chained nonholonomic spherical robot. *Chinese Journal of Aeronautics*, 21(5):472–480, 2008. 147

[122] Laksh Deepak Raura. *Design and Development of Rolling and Hopping Ball Robots for Low Gravity Environment*. Arizona State University, 2016. 158, 159

[123] Rosphere – a spherical robot for exploration and monitoring, Nov 2013. 141

[124] D.P. Robertson and R. Cipolla. *Practical Image Processing and Computer Vision*, chapter Structure from Motion. John Wiley, 2009. 79, 81

[125] M. S. Robinson, J. W. Ashley, A. K. Boyd, R. V. Wagner, E. J. Speyerer, B. Ray Hawke, H. Hiesinger, and C. H. van der Bogert. Confirmation of sublunarean voids and thin layering in mare deposits. *Planetary and Space Science*, 69(1):18–27, August 2012. 15, 68

[126] M. S. Robinson, J. W. Ashley, A. K. Boyd, R. V. Wagner, E. J. Speyerer, B. Ray Hawke, H. Hiesinger, and C. H. van der Bogert. Confirmation of sublunarean voids and thin layering in mare deposits. *Planetary and Space Science*, 69(1):18–27, 2012. 18, 19, 22, 24

[127] M. S. Robinson, S. M. Brylow, M. Tschimmel, D. Humm, S. J. Lawrence, P. C. Thomas, B. W. Denevi, E. Bowman-Cisneros, J. Zerr, M. A. Ravine, M. A. Caplinger, F. T. Ghaemi, J. A. Schaffner, M. C. Malin, P. Mahanti, A. Bartels, J. Anderson, T. N. Tran, E. M. Eliason, A. S. McEwen, E. Turtle, B. L. Jolliff, and H. Hiesinger. Lunar Reconnaissance Orbiter Camera (LROC) Instrument Overview. *Space Science Reviews*, 150(1):81–124, January 2010. 16

[128] Angelo Pio Rossi and Stephan Van Gasselt. *Planetary geology*. Springer, 2018. 14

[129] Rusil. Sar, Jun 2006. 156

[130] Edward B Saff and Amo BJ Kuijlaars. Distributing many points on a sphere. *The mathematical intelligencer*, 19(1):5–11, 1997. 164

[131] Stevanus Satria and Lee Jia Wen. Portable amphibious spherical rolling robot with live-streaming capability for ground and aquatic deployment. *IRC SCT*, 2015. 145, 146

[132] Stevanus Satria, Lee Jia Wen, and Samantha Chan Wei Ting. Salamander, portable amphibious spherical robot. *SALAMANDER Closing Report*, 2016. 146, 147

[133] Francesco Sauro, Riccardo Pozzobon, Matteo Massironi, Pierluigi De Berardinis, Tommaso Santagata, and Jo De Waele. Lava tubes on Earth, Moon and Mars: A review on their size and morphology revealed by comparative planetology. *Earth-Science Reviews*, 209:103288, October 2020. 13

[134] Francesco Sauro, Riccardo Pozzobon, Tommaso Santagata, Ilaria Tomasi, Matteo Tonello, Jesús Martínez-Frías, Laurens M. Johannes Smets, Gustavo David Santana Gómez, and Matteo Massironi. Volcanic Caves of Lanzarote: A Natural Laboratory for Understanding Volcano-Speleogenetic Processes and Planetary Caves. In Elena Mateo, Jesús Martínez-Frías, and Juana Vegas, editors, *Lanzarote and Chinijo Islands Geopark: From Earth to Space*, pages 125–142. Springer International Publishing, Cham, 2019. 16

[135] Gregory C Schroll. *Dynamic model of a spherical robot from first principles*. PhD thesis, Colorado State University. Libraries, 2010. 155

[136] Mattias Seeman. Tele-operated remote inspection with a spherical robot. Technical report, Örebro University, 2009. 142

[137] Mattias Seeman, Mathias Broxvall, Alessandro Saffiotti, and Peter Wide. An autonomous spherical robot for security tasks. In *2006 IEEE International Conference on Computational Intelligence for Homeland Security and Personal Safety*, pages 51–55. IEEE, 2006. 142

[138] E. Simioni, C. Pernechele, C. Re, L. Lessio, and G. Cremonese. GEOMETRICAL CALIBRATION FOR THE PANROVER: A STEREO OMNIDIRECTIONAL SYSTEM FOR PLANETARY ROVER. In *Int. Arch. Photogramm. Remote Sens. Spatial Inf. Sci., XLIII-B3-2020*, pages 1151–1158, April 2020. 54

[139] E. Simioni, C. Re, V. Da Deppo, G. Naletto, D. Borrelli, M. Dami, I. Ficai Veltroni, and G. Cremonese. Indoor calibration for stereoscopic camera STC: a new method. In *Proceedings Volume 10563, International Conference on Space Optics – ICSO 2014; 105634E*, April 2017. 54

[140] Solarbotics. The 'wanna be' miniball - beam robot by solarbotic, Sep 2009. 156, 157

[141] Paul D. Spudis, Patrick J. McGovern, and Walter S. Kiefer. Large shield volcanoes on the Moon. *Journal of Geophysical Research: Planets*, 118(5):1063–1081, 2013. _eprint: https://agupubs.onlinelibrary.wiley.com/doi/pdf/10.1002/jgre.20059. 22

[142] Michelle Starr. Morphex transforming robot is more than meets the eye, Aug 2014. 163

[143] Todor Stoyanov and Achim J. Lilienthal. Maximum Likelihood Point Cloud Acquisition from a Mobile Platform. In *Proceedings of the IEEE International Conference on Advanced Robotics (ICAR '09)*, pages 1 – 6, June 22–26 2009. 82

[144] Jussi Suomela and Tomi Ylikorpi. Ball-shaped robots: an historical overview and recent developments at tkk. In *Field and service robotics*, pages 343–354. Springer, 2006. 155, 161

[145] H. Surmann, A. Nüchter, and J. Hertzberg. An autonomous mobile robot with a 3D laser range finder for 3D exploration and digitalization of indoor environments. *Journal Robotics and Autonomous Systems (JRAS)*, 45(3–4):181–198, December 2003. 60, 61

[146] David Szondy. Rosphere spherical robot could be rolling up for work to monitor and tend crops, May 2015. 140

[147] F.B. Tatom, V. Srepel, R.D. Johnson, N.A. Contaxes, J.L. Adams, H. Seaman, and B.L. Cline. Lunar dust degradation effects and removal/prevention concepts. Technical report, NASA, 1967. 127

[148] Wee Kian Teo and Kai Leong Wong. Systems and methods for contactless automatic dust removal from a glass surface. Patent US 8,091,167 B2, `https://patentimages.storage.googleapis.com/46/1a/44/eb45cf06b9daf9/US8091167.pdf`, January 2012. 83

[149] Audai K. Theinat, Anahita Modiriasari, Antonio Bobet, H. Jay Melosh, Shirley J. Dyke, Julio Ramirez, Amin Maghareh, and Daniel Gomez. Lunar lava tubes: Morphology to structural stability. *Icarus*, 338:113442, March 2020. 13

[150] ThorLabs. Application note risley prism scanner. `https://www.thorlabs.com/images/tabimages/Risley_Prism_Scanner_App_Note.pdf`. 46, 47

[151] B. Tovar, R. Murrieta-Cid, and S.M. LaValle. Distance-optimal navigation in an unknown environment without sensing distances. *IEEE Transactions on Robotics (TRO)*, 23(3):506–518, 2007. 61

[152] Joshua Tristancho, Michael Barrucco, Ryan Weed, David Masten, and Sean Casey. A lunar explorer self-contained picorover. *38th COMMITTEE ON SPACE RESEARCH Scientific Assembly*, 2010. 143

[153] Robert V. Wagner and Mark S. Robinson. Distribution, formation mechanisms, and significance of lunar pits. *Icarus*, 237:52–60, July 2014. 14, 23

[154] Keith W Wait, Philip J Jackson, and Lanny S Smoot. Self locomotion of a spherical rolling robot using a novel deformable pneumatic method. In *2010 IEEE International Conference on Robotics and Automation*, pages 3757–3762. IEEE, 2010. 159, 160

[155] Weiren Wu, Chunlai Li, Wei Zuo, Hongbo Zhang, Jianjun Liu, Weibin Wen, Yan Su, Xin Ren, Jun Yan, Dengyun Yu, Guangliang Dong, Chi Wang, Zezhou Sun, Enhai Liu, Jianfeng Yang, and Ziyuan Ouyang. Lunar farside to be explored by Chang'e-4. *Nature Geoscience*, 12(4):222–223, April 2019. Number: 4 Publisher: Nature Publishing Group. 15

[156] Long Xiao. China's touch on the Moon. *Nature Geoscience*, 7(6):391–392, June 2014. Number: 6 Publisher: Nature Publishing Group. 15

[157] CAI Yao, GAO Feng, and LIU Zening. Neural network compensation method for path tracking control of a spherical mobile robot. *Applied Mechanics & Materials*, 2014. 147

[158] Tomi Ylikorpi, Aarne Halme, Peter Jakubik, Jussi Suomela, and Mika Vainio. Biologically inspired solutions for robotic surface mobility. In *Proceedings of 8th ESA Workshop on Advanced Space Technologies for Robotics and Automation*, pages 2–4, 2004. 160, 161

[159] Tomi Ylikorpi and Jussi Suomela. *Ball-shaped robots*. INTECH Open Access Publisher, 2007. 161

[160] Joong-Cheol Yoon, Sung-Su Ahn, and Yun-Jung Lee. Spherical robot with new type of two-pendulum driving mechanism. In *2011 15th IEEE International Conference on Intelligent Engineering Systems*, pages 275–279. IEEE, 2011. 149, 150

[161] Qiang Zhan, Yao Cai, and Caixia Yan. Design, analysis and experiments of an omni-directional spherical robot. In *2011 IEEE International Conference on Robotics and Automation*, pages 4921–4926. IEEE, 2011. 151, 152, 153

Die Schriftenreihe

wird vom Lehrstuhl für Informatik VII: Robotik und Telematik der Universität Würzburg herausgegeben und präsentiert innovative Forschung aus den Bereichen der Robotik und der Telematik.

Die Kombination fortgeschrittener Informationsverarbeitungsmethoden mit Verfahren der Regelungstechnik eröffnet hier interessante Forschungs- und Anwendungsperspektiven. Es werden dabei folgende interdisziplinäre Aufgabenschwerpunkte bearbeitet:

- Robotik und Mechatronik: Kombination von Informatik, Elektronik, Mechanik, Sensorik, Regelungs- und Steuerungstechnik, um Roboter adaptiv und flexibel ihrer Arbeitsumgebung anzupassen.

- Telematik: Integration von Telekommunikation, Informatik und Steuerungstechnik, um Dienstleistungen an entfernten Standorten zu erbringen.

Anwendungsschwerpunkte sind u.a. mobile Roboter, Tele-Robotik, Raumfahrtsysteme und Medizin-Robotik.

Lehrstuhl Informatik VII
Robotik und Telematik
Am Hubland
D-97074 Wuerzburg

Tel.: +49 (0) 931 - 31 - 86678
Fax: +49 (0) 931 - 31 - 86679

schi@informatik.uni-wuerzburg.de
http://www7.informatik.uni-wuerzburg.de

ISSN: 1868-7474 (online)
ISSN: 1868-7466 (print)
ISBN: 978-3-945459-33-1 (online)

Zitation dieser Publikation

Rossi, A. P., et al. (2021). DAEDALUS - Descent And Exploration in Deep Autonomy Lava Underground Structures. Schriftenreihe Würzburger Forschungsberichte in Robotik und Telematik, Band 21. Würzburg: Universität Würzburg.
DOI: 10.25972/OPUS-22791

Eine Kooperation von